Topological phases in two-dimensional systems

Emmanuel Victor Caires Lopes

Universidade Federal de Uberlândia
Instituto de Física
Programa de Pós-Graduação em Física

Uberlândia
2025

Emmanuel Victor Caires Lopes

Topological phases in two-dimensional systems

Tese de doutorado apresentada ao Programa de Pós-graduação em Física da Universidade Federal de Uberlândia como parte dos requisitos para a obtenção do título de Doutor em Física.

Área de concentração: Física

Orientador: Tome Mauro Schmidt

Uberlândia
2025

Dados Internacionais de Catalogação na Publicação (CIP)
Sistema de Bibliotecas da UFU, MG, Brasil.

L864t 2025

Lopes, Emmanuel Victor Caires, 1996-
Topological phases in two-dimensional systems [recurso eletrônico] / Emmanuel Victor Caires Lopes. - 2025.

Orientador: Tome Mauro Schmidt.
Tese (Doutorado) - Universidade Federal de Uberlândia, Programa de Pós-graduação em Física.
Modo de acesso: Internet.
Disponível em: http://doi.org/10.14393/ufu.te.2025.5514
Inclui bibliografia.
Inclui ilustrações.

1. Física. 2. Materiais bidimensionais. 3. Isolantes topológicos. 4. Funcionais de densidade. I. Schmidt, Tome Mauro, 1965-, (Orient.). II. Universidade Federal de Uberlândia. Programa de Pós-graduação em Física. III. Título.

CDU: 53

Rejâne Maria da Silva
Bibliotecária-Documentalista – CRB6/1925

UNIVERSIDADE FEDERAL DE UBERLÂNDIA
Coordenação do Programa de Pós-Graduação em Física
Av. João Naves de Ávila, 2121, Bloco 1A, Sala 213 - Bairro Santa Mônica, Uberlândia-MG, CEP 38400-902
Telefone: (34) 3239-4309 - www.infis.ufu.br - cpgfisica@ufu.br

ATA DE DEFESA - PÓS-GRADUAÇÃO

Programa de Pós-Graduação em:	Física				
Defesa de:	Defesa de Doutorado				
Data:	Dezoito de julho de 2025	Hora de início:	09:00	Hora de encerramento:	12:00
Matrícula do Discente:	12123FIS002				
Nome do Discente:	Emmanuel Victor Caires Lopes				
Título do Trabalho:	*Topological phases in two-dimensional systems*				
Área de concentração:	Física				
Linha de pesquisa:	Estrutura eletrônica e simulações computacionais				
Projeto de Pesquisa de vinculação:	*N.A*				

Reuniu-se, por meio de videoconferência, a Banca Examinadora, designada pelo Colegiado do Programa de Pós-graduação em Física, assim composta: Professores Doutores: Gerson Ferreira Junior - INFIS/UFU, George Balster Martins- INFIS/UFU, Felipe David Crasto de Lima - CNPEM, Marcio Jorge Teles da Costa - UFF e Tomé Mauro Schmidt - INFIS/UFU, orientador do discente.

Iniciando os trabalhos o presidente da mesa, Prof. Tomé Mauro Schmidt, apresentou a Comissão Examinadora e o candidato, agradeceu a presença do público, e concedeu ao discente a palavra para a exposição do seu trabalho. A duração da apresentação do discente e o tempo de arguição e resposta foram conforme as normas do Programa.

A seguir o senhor(a) presidente concedeu a palavra, pela ordem sucessivamente, aos(às) examinadores(as), que passaram a arguir o(a) candidato(a). Ultimada a arguição, que se desenvolveu dentro dos termos regimentais, a Banca, em sessão secreta, atribuiu o resultado final, considerando o(a) candidato(a):

Aprovado

Esta defesa faz parte dos requisitos necessários à obtenção do título de Doutor.

O competente diploma será expedido após cumprimento dos demais requisitos, conforme as normas do Programa, a legislação pertinente e a regulamentação interna da UFU.

Nada mais havendo a tratar foram encerrados os trabalhos. Foi lavrada a presente ata que após lida e achada conforme foi assinada pela Banca Examinadora.

Documento assinado eletronicamente por **George Balster Martins**, **Professor(a) do Magistério Superior**, em 22/07/2025, às 08:39, conforme horário oficial de Brasília, com fundamento no art. 6º, § 1º, do Decreto nº 8.539, de 8 de outubro de 2015.

Documento assinado eletronicamente por **Tome Mauro Schmidt**, **Presidente**, em 22/07/2025, às 10:16, conforme horário oficial de Brasília, com fundamento no art. 6º, § 1º, do Decreto nº 8.539, de 8 de outubro de 2015.

Documento assinado eletronicamente por **Gerson Ferreira Junior**, **Professor(a) do Magistério Superior**, em 22/07/2025, às 10:21, conforme horário oficial de Brasília, com fundamento no art. 6º, § 1º, do Decreto nº 8.539, de 8 de outubro de 2015.

Documento assinado eletronicamente por **Felipe David Crasto de Lima**, **Usuário Externo**, em 22/07/2025, às 14:54, conforme horário oficial de Brasília, com fundamento no art. 6º, § 1º, do Decreto nº 8.539, de 8 de outubro de 2015.

Documento assinado eletronicamente por **Marcio Jorge Teles da Costa**, **Usuário Externo**, em 29/07/2025, às 09:48, conforme horário oficial de Brasília, com fundamento no art. 6º, § 1º, do Decreto nº 8.539, de 8 de outubro de 2015.

A autenticidade deste documento pode ser conferida no site https://www.sei.ufu.br/sei/controlador_externo.php?acao=documento_conferir&id_orgao_acesso_externo=0, informando o código verificador **6528679** e o código CRC **84C55116**.

Referência: Processo nº 23117.049932/2025-13 SEI nº 6528679

Agradecimentos

To God,

To my family, for the unconditional love and support

To my friends, for the motivation and funny times

To professor Tome Mauro Schmidt, for the extreme patience and carefull guidance

To professor Roberto Hiroki Miwa, for the helpfull discussions and collaboration

To all members of the Physics Institute (INFIS) at UFU

To CAPES, for the financial support

To LNCC (project SCAFMat2) and CENAPAD (project proj483), for the computational resources

Resumo

Nesta tese, investigamos o surgimento de propriedades topológicas em sistemas bidimensionais (2D). Realizamos os cálculos utilizando a Teoria do Funcional da Densidade (DFT) e métodos *tight-binding*. O primeiro sistema estudado foi a monocamada de bismuto, um conhecido isolante topológico, dopado com um átomo magnético. Nossos cálculos mostraram que as propriedades magnéticas introduzidas não afetam a fase topológica. Notavelmente, demonstramos que, quando as impurezas estão localizadas próximas à borda, surge um acoplamento de longo alcance. Além disso, verificamos duas transições de fase magnética em função da distância entre as impurezas, comportamento característico das interações Ruderman-Kittel-Kasuya-Yosida (RKKY). Essas conclusões foram validadas por meio do Hamiltoniano RKKY, cujos resultados apresentam boa concordância com os cálculos de DFT. A segunda fase topológica investigada neste trabalho emerge em estruturas porosas de SiGe e Ge semelhantes ao grafenileno. Verificou-se cruzamentos de bandas quadruplamente degenerados que, com a inclusão do acoplamento *spin*-órbita, se dividem em um par de pontos de Weyl. Suas propriedades topológicas foram confirmadas por meio do cálculo da quiralidade de Weyl e da curvatura de Berry. Essas conclusões foram corroboradas pelos estados topológicos de borda que conectam pontos de Weyl com quiralidades opostas, arcos de Fermi. Por fim, estudamos o efeito Hall quântico anômalo em monocamadas de 1T-CrX_2 (X = Bi, Sb) sob tensão biaxial extrema. Essa fase surge da interação entre o acoplamento *spin*-órbita, efeitos de muitos elétrons e deformação biaxial. Estados topológicos de borda também foram observados, concordando com a correspondência entre *bulk* e borda. Os resultados deste capítulo ampliam a lista de materiais magnéticos bidimensionais com a predição do sistema 1T-$CrBi_2$. Para ambos os sistemas, nossos cálculos mostram temperaturas de Curie acima de 160 K, o que fornece descobertas valiosas para o contexto do efeito Hall quântico anômalo.

Palavras-chave: Propriedades topológicas, Materiais bidimensionais, Interação *spin*-órbita, Estrutura eletrônica.

Abstract

In this thesis, we investigate the emergence of topological properties in two-dimensional (2D) systems. We perform the calculations using density functional theory and tight-binding methods. The first system we investigate is a bismuth monolayer, a well-known topological insulator, doped with magnetic atoms. Our calculations show that the introduced magnetic perturbation does not affect the topological phase. Notably, we verify that when the impurities are located near the edge, a long-range coupling arises between them. Additionally, we note the occurrence of two magnetic phase transitions as a function of the inter-impurity distance, a signature of Ruderman-Kittel-Kasuya-Yosida (RKKY) interactions. These conclusions are validated by means of the derived RKKY Hamiltonian, whose results show good agreement with DFT calculations. The second topological phase investigate in this work emerges in graphenylene-like porous SiGe and Ge structures. We find fourfold degenerate band crossings which, under spin-orbit coupling, split into a pair of Weyl points. Their topological properties are confirmed through Weyl chirality and Berry curvature calculations. These conclusions are supported by the bulk-boundary correspondence, where we verify topological edge states (2D Fermi arcs) connecting Weyl points with opposite chiralities. Finally, we study the quantum anomalous Hall effect in extremely biaxial tensile strained 1T-CrX_2 (X = Bi, Sb) monolayers. This topological phase arises from the interplay of spin-orbit coupling, many-body effects and biaxial tensile strain. Topological edge states are also observed, consistent with the bulk-boundary correspondence. The results of this investigation extend the list of two-dimensional magnetic materials, in which we predict the stability of the free standing 1T-$CrBi_2$ monolayer. For both systems, our calculations show Curie temperatures above 160 K, which provides valuable findings for the quantum anomalous Hall context.

Keywords: Topological properties, Two-dimensional materials, Spin-orbit interaction, Electronic Structure.

List of Figures

Figure 1 – Two dimensional materials and its different crystal structures. Image from Ref. [1]. 17
Figure 2 – Timeline of experimentally observed topological systems following the theoretical prediction of the quantum spin Hall effect in 2005. Image from Ref. [2]. 18
Figure 3 – Topological materials and their applications in different research fields. Image from Ref. [3]. 19
Figure 4 – Surfaces of a sphere (a), torus (b), and double torus (c), representing the geometric forms with genus $g = 0$, $g = 1$, and $g = 2$, respectively. . 36
Figure 5 – Illustration of the band inversion process in a topological insulator. The blue and red color indicates the valence and conduction bands, respectively. As the SOC increases, the band gap start from a trivial behavior (a), achieve a critical point (b) and reopens with inverted character (c). Image from Ref. [4]. 37
Figure 6 – Schematic representation of topological edge (a)-(b) and surface (c)-(d) states. Panels (a) and (c) show the real-space scenario, while (b) and (d) illustrates the corresponding momentum-space representation. Figure from Ref. [5]. 38
Figure 7 – Schematic illustration of an inverted band structure without SOC. The inclusion of SOC can open a band gap (a), characterizing a topological insulator phase, or when combined with a fundamental symmetry breaking, form a Weyl semimetal phase (b). In the topological insulator phase, the arrows represent the helical spin texture of the Dirac cone, while in the Weyl semimetal phase the arrows indicate the Fermi arcs. Adapted image from Ref. [6]. 40
Figure 8 – Momentum-resolved (a) and energy-resolved (b) measurements of the Fermi arcs on the TaAs surface. The red and blue points indicate the Weyl nodes with opposite chiralities. Adapted image from Ref. [7]. . . 41

Figure 9 – Scheme of the quantum anomalous Hall effect. The blue arrows represent the dissipationless topological edge states, and the black arrows indicate the intrinsic magnetic moment of the material. 43

Figure 10 – Top (a) and side (b) view of the bismuthene crystal structure. The black line indicates the unit cell, which contains two atoms. 46

Figure 11 – Projected band structure for bismuthene without SOC (a) and under different percentages of SOC: 25% (b), 50% (c), 75% (d), and 100% (e). The blue and red circles correspond to the p_z and p_{xy} orbitals, respectively. 47

Figure 12 – (a) Bismuthene band structure without edge passivation. The contribution of the edge state is highlighted with the high intensity contribution in colormap, while the bulk shows a low intensity contribution. Spin texture colormap is shown in (b) for $\langle S_y \rangle$ component and (c) for $\langle S_z \rangle$ counterpart. The red (blue) color indicates spin up (spin down). The bismuthene nanoribbon in a zigzag cut illustrating figure is shown in (d), the arrows indicate the system periodicity. 48

Figure 13 – Left (a) and right (b) edge projected spin texture $\langle S_z \rangle$ component onto band structure for the hydrogen edge passivated bismuthene (c). Here, the blue circles indicate spin down while the red color represents spin up. 49

Figure 14 – Bismuthene doped with one V atom at the top and side view in (a). Projected band structure for pristine Bi monolayer (b), vanadium doped Bi system without (c) and with (d) U_{eff} correction. The red (blue) circles represent the contribution of p_{xy} (p_z) orbitals and the green circles represent the d-orbitals from V atoms. 50

Figure 15 – Bismuthene nanoribbon with vanadium atoms (magenta circles) near the edge. The dashed lines indicate the possible first and second point defect substitution. At the edge, the white atoms represents the hydrogen atoms. 51

Figure 16 – Magnetic coupling (total energy difference) as a function of the inter-impurity distance when the V-atoms are in bulk (a) and at the edge (b) of the bismuthene. 52

Figure 17 – Bismuthene structure with vanadium impurities near the edge is shown in (a), the arrows indicate the magnetic orientation for this system. In (b) is shown the orbital contribution of the doped edge atoms to the band structure and (c) the spin component $\langle S_z \rangle$ contribution. For the antiferromagnetic orientation of V atoms (d), the same is shown in (e) and (f). 53

Figure 18 – Energy dispersion E(k) for different β parameters. The solid, dashed, and dash-dotted lines correspond to different values of β, as indicated in the legend box. Here, $E_+(k)$ and $E_-(k)$ are plotted in the same color. 55

Figure 19 – Direct comparison between effective model results (purple triangles) at the lattice parameter distance points and DFT counterpart (black circles). The inset shows the continuous curve for the effective model. . 58

Figure 20 – Porous structure at the top (upper figure) and side (lower figure) views. Here, the dashed line represents the unit cell, which is composed by 12 atoms. The blue (I) and magenta (II) atoms was studied in both Ge and Si (I)/Ge (II) atomic distribution, respectively. 60

Figure 21 – Porous SiGe (a)-(b) and Ge (c)-(d) band structures, respectively. Figures (a) and (c) show the electronic band structure with SOC effect. In counterpart, (b) and (d) are without SOC inclusion. A small band gap between valence and conduction band is highlighted in (a-2) and (c-2) figures, while in (a-3) and (c-3) is the Weyl crossing pair. The same energy range is shown in (b) and (d), showing the behavior of bands without SOC. 61

Figure 22 – Position of Weyl points and their chiralities in the Brillouin zone for SiGe (a) and Ge (b) atomic composition. In insets it is highlighted the position of WPs. Unlike to the Ge WPs, which is on the high-symmetry Γ-M line, the SiGe WPs are located in the Σ-Σ_1 path (green-line). Here, the blue (red) represents the positive (negative) chirality. 63

Figure 23 – Berry curvature distribution for a selected region in kx,ky plane in Porous Ge system. The aquamarine region is highlighted in the next figure. The blue (red) color indicates the Berry curvature of the Weyl point with positive (negative) chirality. The inset figure shows a zoom in the negative chiral pair, which in distance it can not be distinguished. 63

Figure 24 – Porous structure nanoribbon with periodicity only in the arrows direction (a). The projection of the Weyl points in the edge path which connects Weyl pairs with opposite chirality is shown in (c). 64

Figure 25 – Band structure plot with the Weyl points projection for porous SiGe (a) and (c) system without and with hydrogen saturation, respectively. Figures (b) and (d) show the same, but for Ge counterpart. The blue and red circles represents the Weyl point chirality of the projected Weyl points. The high intensity edge states corresponds to the 1D Fermi arcs. 65

Figure 26 – Spin components plots of the Fermi arcs in Ge (a)-(c) and SiGe (d)-(f) structures. The red and blue colors indicates the positive and negative spin values, respectively. 66

Figure 27 – Crystal structure of 1T-CrX_2 (X=Bi, Sb) monolayer at the top (a) and side views (b). The magenta spheres represent the Cr atoms and the blue counterpart Bi or Sb atoms. The black line indicates the unit cell. 72

Figure 28 – Dynamical and thermal stabilities for 1T-CrX_2 monolayers. In (a) and (b) is shown the phonon spectra for 1T-$CrBi_2$ and 1T-$CrSb_2$ monolayers, respectively. For these respective systems, (c) and (d) show the *ab initio* molecular dynamics at 300 K, with the final snapshot highlighted in the inset. The buckling height as a function of the lattice parameter is shown in (e) and (f) for Bi and Sb compositions, respectively. 73

Figure 29 – Phonon dispersion for the ultimate tensile strained 1T-$CrBi_2$ monolayer (20%) in (a) and for the ultimate strain value for 1T-$CrSb_2$ (25%) in (b). Strain-energy curve as function of the biaxial tensile strain is shown in (c). 74

Figure 30 – Total energy difference between the Cr atoms aligned in AFM and FM configuration as function of the biaxial tensile strain. The positive (negative) values indicate the AFM (FM) phase as most stable in comparison with FM (AFM) alignment. 75

Figure 31 – Magnetic anisotropy energy (given in meV) as function of U_{eff} parameter for ultimate tensile strained 1T-$CrBi_2$ (a) and 1T-$CrSb_2$ (b). The positive and negative MAE values indicate the easy magnetization axis out-of-plane and in-plane, respectively. 77

Figure 32 – Magnetic moment as function of the temperature for 1T-$CrBi_2$ monolayer under 20% of biaxial tensile strain in red symbols and in blue for 1T-$CrSb_2$ monolayers under 25%. 78

Figure 33 – Band structure without (a) and with (b) SOC effects in ultimate tensile-strained 1T-$CrBi_2$ monolayer, additionally (c) shows the Berry curvature distribution in momentum space. For the Sb counterpart, at the ultimate tensile strain, the band structures without and with SOC are shown in (d) and (e), respectively, and (f) shows the Berry curvature plot for this system. 79

Figure 34 – Evolution of Wannier charge centers for the ultimate tensile strained 1T-CrX_2 monolayers. Plots for 1T-$CrBi_2$ with OP and IP magnetism are shown in (a) and (c), respectively. For the Sb counterpart, the corresponding plots are shown in (b) and (d), representing the OP and IP magnetism, respectively. 80

Figure 35 – Projected band structure along the edge path of 1T-$CrBi_2$ with two different biaxial tensile strain values, 19% (a) and 20% (b). In (d) and (e), the same is shown for 23.4% and 25% tensile strained 1T-$CrSb_2$. The green arrows indicate the topological edge states. The anomalous Hall conductivity for the highest tensile strained Bi and Sb compositions is shown in (c) and (d). A schematic figure of a quantum anomalous Hall device and a way to measure anomalous Hall conductivity is illustrated in (g). The blue and black arrows indicates the edge states and intrinsic OP magnetism, respectively. 81
Figure 36 – Topological phase diagram for 1T-CrX_2 monolayers, with the Chern number as function of the percentage of biaxial tensile. The black symbols represent the Bi composition and purple symbols the Sb counterpart. 82

List of Tables

Table 1 – Cohesive and formation energies of CrX_2 systems in a free standing (FS) configuration, and at the ultimate tensile strain (TS) form. Here, the Cohesive energy is given in eV/atom, and the formation energy is expressed in eV per unit cell. 74
Table 2 – Calculated magnetic anisotropy energy values (in meV) for the 1T-$CrBi_2$ monolayers under different external biaxial tensile strain. The easy magnetization axis is located in-plane (out-of-plane) when the MAE values are negative (positive). 75
Table 3 – Calculated magnetic anisotropy energy values (in meV) for the 1T-$CrSb_2$ monolayers under different external biaxial tensile strain. The easy magnetization axis is located in-plane (out-of-plane) when the MAE values are negative (positive). 76
Table 4 – Relative energy calculations, given in meV, for the 1T-$CrSb_2$ monolayer with the U_{eff} = 4 eV. The ground magnetic phase is ferromagnetic, which is set as zero, and the values reflects the total energy difference with relation to Néel, Stripy and Zigzag magnetic phases. 76
Table 5 – Magnetic parameters for 1T-CrX_2 monolayers at the ultimate tensile strain. The magnetization per Cr atom is given in μ_B, the magnetic anisotropy energy in meV, while the coupling parameter ΔE_{AFM-FM} per Cr atoms in the system is also given in meV. The Curie temperature is shown in Kelvin. 78

Contents

1 INTRODUCTION . . . 16
1.1 Thesis overview . . . 17

2 METHODOLOGY . . . 20
2.1 Density Functional Theory . . . 21
2.1.1 Hohenberg-Kohn theorems . . . 21
2.1.2 Kohn-Sham *Ansatz* . . . 22
2.1.3 Kohn-Sham equations . . . 23
2.2 Functionals and Approximations . . . 26
2.2.1 Local density approximation . . . 27
2.2.2 Generalized gradient approximation . . . 27
2.2.3 DFT+U . . . 28
2.3 Spin density functional theory . . . 29
2.4 Berry Phase . . . 30
2.5 Wannier functions . . . 32

3 TOPOLOGICAL SYSTEMS IN CONDENSED MATTER . . . 35
3.1 Topology . . . 35
3.2 Topological insulators . . . 36
3.3 Weyl semimetals . . . 38
3.4 Quantum anomalous Hall insulators . . . 42

4 RKKY INTERACTION MEDIATED BY TOPOLOGICAL STATES IN BISMUTHENE . . . 45
4.1 Bismuth monolayer - Revision . . . 45
4.2 Electronic properties of V-doped bismuthene . . . 49
4.3 Magnetic interactions in bulk . . . 51
4.4 Magnetic interactions via topological edge states . . . 52

4.5 Effective Hamiltonian . . . 54

5 TWO-DIMENSIONAL WEYL SEMIMETALS . . . 59
5.1 Structural and electronic properties . . . 59
5.2 Topological properties . . . 60
5.3 Weyl equation analysis for 2D systems . . . 66
5.3.1 Eigenenergies and Eigenfunctions . . . 67
5.3.2 Topological analysis . . . 69

6 QUANTUM ANOMALOUS HALL EFFECT IN 1T-CRX_2 MONOLAYERS . . . 71
6.1 Stability of 1T-MX structures . . . 71
6.2 Magnetic properties . . . 74
6.2.1 Curie Temperature . . . 77
6.3 Quantum Anomalous Hall effect . . . 78

7 CONCLUSION . . . 83

BIBLIOGRAPHY . . . 86

APPENDIX 103

APPENDIX A – COMPUTATIONAL DETAILS . . . 104
A.1 Chapter 4 . . . 104
A.2 Chapter 5 . . . 105
A.3 Chapter 6 . . . 105

APPENDIX B – ACADEMIC PRODUCTION . . . 106
B.1 Thesis originated articles . . . 106
B.2 Articles in collaboration . . . 106
B.3 Conferences . . . 106
B.4 Awards . . . 107

Chapter 1

Introduction

The experimental realization of graphene in 2004 [8, 9] provided a revolution in materials science. The successful isolation of a two-dimensional (2D) system, previously believed to be experimentally inaccessible, represented a major breakthrough in physics. Due to this remarkable achievement, Andre Geim and Konstantin Novoselov were awarded the Nobel Prize in Physics in 2010. Since this experimental report, many other 2D materials with graphene-like structures have been synthesized, such as silicene [10], bismuthene [11, 12], stanene [13, 14] and hexagonal boron nitride [15]. Additionally, materials that crystallize in other structures, such as MXenes [16, 17], metal-organic frameworks [18, 19], black phosphorus-based systems [20, 21] and transition metal dichalcogenetes [22], have also been synthesized. Their structures are illustrated in Fig. 1. In electronic band theory, materials are classified by their band gap as semiconductors, metals and insulators. It is important to note that all these electronic classifications were observed in the 2D context [23], creating new opportunities for research in low-dimensional systems. Magnetic materials constitute an important subclass of 2D materials, despite early theoretical predictions, the first experiment realization was achieved only in 2017 [24]. A few materials have been synthesized in this new subclass, including CrY_3 (Y = Cl, Br, I) [24, 25, 26], Fe_3GeTe_2 [27], and $Cr_2Ge_2Te_6$ [28]. The combination of magnetic properties and 2D architecture is desired for different applications in condensed matter physics.

The development of 2D materials coincided with the emergence of candidate materials for topological systems in the solid state context. Topological materials combine valuable properties, such as relativistic effects, symmetry-protected topological states, bulk-boundary correspondence, and high-speed [29, 30]. In 2005, the seminal work of Kane and Mele introduced the quantum spin Hall effect in graphene [31], providing key insights into topology and materials science. The first experimental achievement of this phase was reported in 2007 [32]. Since the beginning of topological properties investigation with the Kane-Mele model, several topological phases were observed, including Weyl semimetals [33, 6, 34, 35], quantum anomalous Hall effect [36, 37, 38], topological crystalline insulators [39, 40, 41], and high-order topological insulators [42]. The timeline of

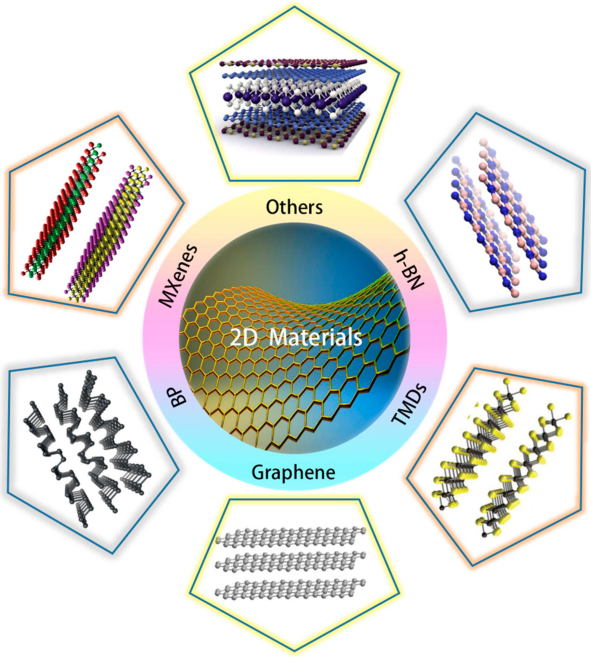

Figure 1 – Two dimensional materials and its different crystal structures. Image from Ref. [1].

experimentally reported topological materials is shown in Fig. 2. Prediction and advances in the topological field had a significant impact on the modern physics, culminating in the 2016 Nobel Prize in Physics awarded to Thouless, Haldane, and Kosterlitz for their discoveries on topological phases of matter and phase transitions.

The United Nations designated 2025 as the International Year of Quantum Science and Technology (QST) [43]. In QST field, topological materials play a significant role in quantum computing and quantum transport applications due to their fundamental properties, such as quantized Hall conductivity, dissipationless boundary states, and high electron mobility. Beyond QST, topological materials have been applied in different fields including catalysis [44, 45], thermoelectricity [34, 46], low energy consumption [47, 30], and optics [48], as illustrated in Fig 3. To enable characterization and optimization of new devices, research efforts to discover and study new topological materials have grown substantially in the last decade.

In this way, computational materials science plays an important role in predicting and studying new materials. With recent advances in computing, is has become accessible to simulate materials at large scales with thousands of atoms, providing valuable guidance for experimental synthesis.

1.1 Thesis overview

In this thesis, we investigate the emergence of topological properties in different two-dimensional materials by means of first-principles calculations. We also investigate the

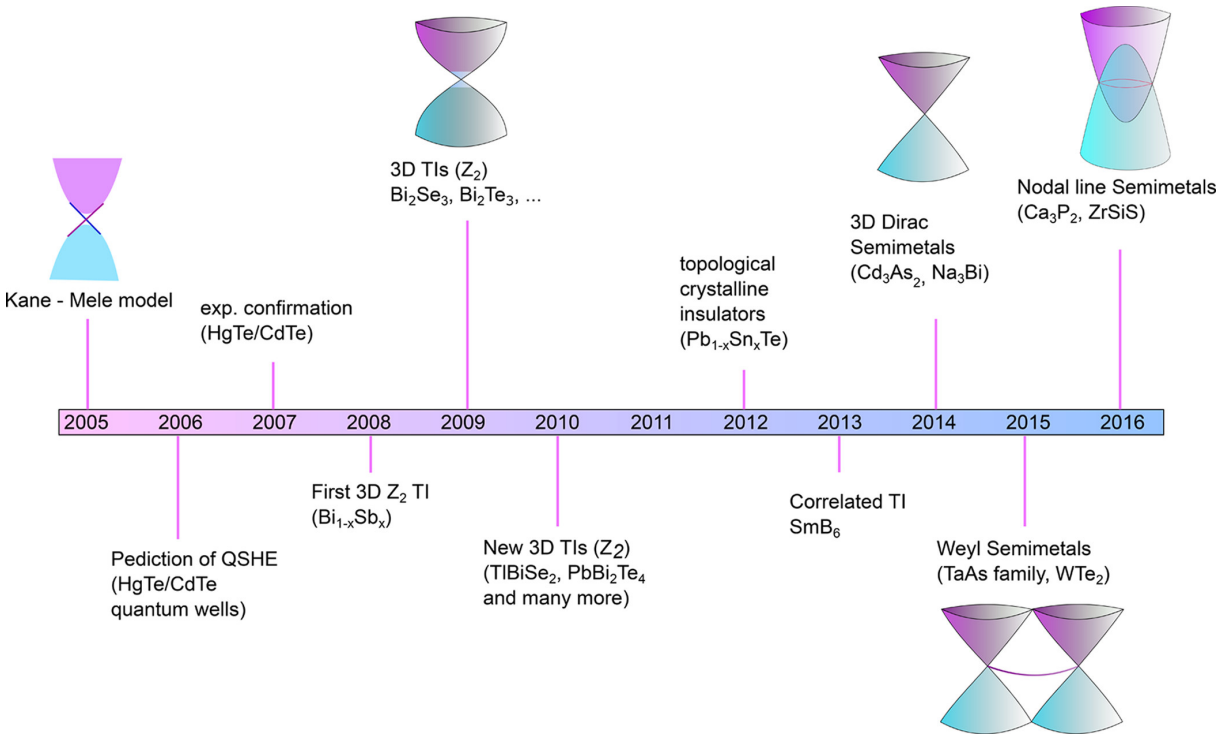

Figure 2 – Timeline of experimentally observed topological systems following the theoretical prediction of the quantum spin Hall effect in 2005. Image from Ref. [2].

effects and consequences of these topological phases. This thesis is composed by seven chapters and is organized as follows:

Chapter 1 is the introduction of this thesis, where the history of two-dimensional materials and topological materials is briefly discussed. Their applications and advances are also discussed in this chapter.

The second chapter describes the methodology used in this research. This chapter starts with a discussion from the perspective of the Schrödinger equation in materials context, and its limitations when applied to systems with a large number of atoms. We connect this to materials context and introduce the density functional theory (DFT). In addition, we derive the Kohn-Sham equations. This chapter also includes a discussion of the approximations for the exchange and correlation term and their appropriate cases. The concepts of Berry phase and Wannier functions are also discussed in detail in the final part of this chapter.

Through this thesis, we investigate different topological phases in two-dimensional systems. The third chapter briefly introduces the concept of topology and its connection to solid state physics. This chapter also contains an introduction to each topological system studied in this work, including the topological insulators, Weyl semimetals and quantum anomalous Hall insulators. We briefly present the history of each class, their key properties, experimental synthesis, and major advances of each field.

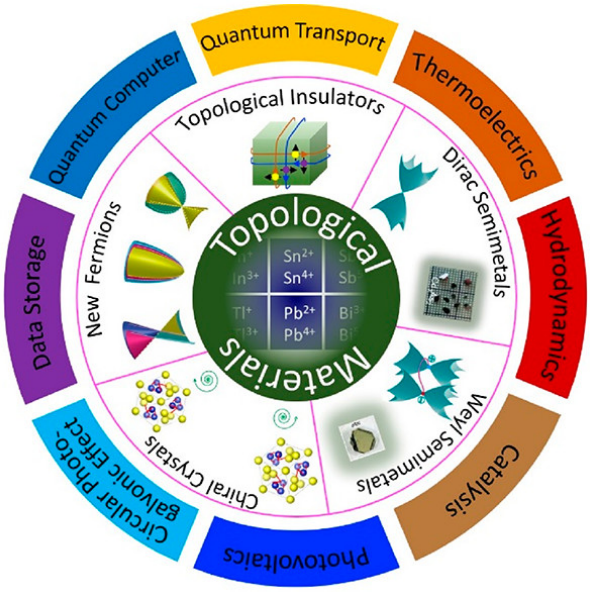

Figure 3 – Topological materials and their applications in different research fields. Image from Ref. [3].

The results of this thesis are divided into Chapters 4, 5, and 6. In Chapter four, we investigate the electronic and topological properties of bismuthene under magnetic doping. This chapter begins with a review of bismuthene and its key topological properties. Magnetism is introduced in bismuthene through a magnetic dopant, magnetic and topological properties are investigated for different doping percentages and system configurations. We observe that the topological edge states couple the magnetic impurities via long-range indirect interaction, which was also investigated in the final section of the chapter using an effective Hamiltonian based on DFT results.

Chapter five discusses a new topic in condensed matter physics, Weyl semimetals in two-dimensional systems. This topological state arises in porous structures that are intrinsically noncentrosymmetric. This chapter presents a well-detailed investigations of Weyl chirality, Berry curvature, two-dimensional Fermi arcs and its spin texture. These results complete the family of Weyl semimetals, with the prediction of the first two-dimensional linear Weyl crossings in a noncentrosymmetric structure.

In the chapter six we discuss the emergence of quantum anomalous Hall effect in 1T-CrX_2 (X = Bi, Sb) monolayers. Beyond the topological properties, we perform a detailed study of crystal stability, electronic and magnetic properties of these systems. Our calculations show a new stable material the 1T-$CrBi_2$ monolayer, extending the list of two-dimensional magnetic materials.

Chapter 2

Methodology

In the search for a complete description of materials, the Schrödinger equation provides a helpful way to extract their physical properties, such as wavefunctions and eigenenergies. In the solid state physics context, a given material is composed of a large number of atoms arranged in a structure. These atoms are composed by nuclei and electrons. The nuclei, in turn, are composed of protons and neutrons. Since a material contains multiple atoms and, consequently, multiple electrons and nuclei, these interactions are described solely by the Coulomb interaction, repulsion between electrons and attraction between electrons and nuclei. With the addition of the kinetic energies, all terms of the Hamiltonian are known.

In this context, it is expected that the system wavefunction depends on the N electrons ($\boldsymbol{r}$) and M nuclei ($\boldsymbol{R}$) coordinates, which assumes the form of $\Psi = \Psi(\boldsymbol{r}_1, ..., \boldsymbol{r}_N, \boldsymbol{R}_1, ..., \boldsymbol{R}_M)$. The Hamiltonian that describes all interactions in materials includes the kinetic energies of the electrons (T_e) and nuclei (T_N), the repulsion between electrons (W_e), the repulsion between nuclei (W_N), and the attraction between nuclei and electrons (V_N). The general Hamiltonian is given by the sum of these terms

$$H = T_e + T_N + W_e + W_N + V_n. \tag{1}$$

The fully expanded Hamiltonian, expressed in Hartree units [49], is given by

$$H = -\sum_i \frac{\nabla_i^2}{2} - \sum_I \frac{\nabla_I^2}{2M} + \frac{1}{2}\sum_{i\neq j} \frac{1}{|\boldsymbol{r}_i - \boldsymbol{r}_j|} + \frac{1}{2}\sum_{I\neq J} \frac{Z_I Z_J}{|\boldsymbol{R}_I - \boldsymbol{R}_J|} - \sum_{i,I} \frac{Z_I}{|\boldsymbol{r}_i - \boldsymbol{R}_I|}. \tag{2}$$

In principle, all physical quantities can be extracted only by solving the time-independent Schrödinger equation (Hψ=Eψ), such as eigenergies and the probability of finding a electron at a given position. However, the solution of the Schrödinger equation for this Hamiltonain can be unpractical due to its multiple degrees of freedom. In this way, there are some approximations that we can perform to reduce the number of variables in the system. One of them is the Born-Oppenheimer approximation [50]. Since the nuclei are nearly 1800 times heavier than the electrons, the nuclei can be considered fixed in

a position, while the electrons move around them. This leads to an uncoupling of the electron and nuclear motions, resulting in a separation of the equations that describes their dynamic. With this approximation, we reduce the terms in the general Hamiltonian to

$$H = T_e + W_e + V_n. \tag{3}$$

This new Hamiltonian is purely electronic. The Schrödinger equation under this new form is given by

$$\left[-\sum_i \frac{\nabla_i^2}{2} + \sum_i V_n(\boldsymbol{r}_i) + \frac{1}{2}\sum_{i \neq j} \frac{1}{|\boldsymbol{r}_i - \boldsymbol{r}_j|} \right] \Psi = E\Psi. \tag{4}$$

Which is the fundamental equation of electronic structure [49]. The solution of this equation provides a complete electronic description, with the wavefunction expressed as $\Psi = \Psi(\boldsymbol{r}_1, ..., \boldsymbol{r}_N)$. However, when attempting to apply the Eq. (4) to a realistic system, the problem becomes quite unworkable. For a single CO_2 molecule, the wavefunction for its 22 electrons will have 66-dimensions [51]. In a complex material, the number of electrons can be larger than 10^{22}. In this way, further considerations can be used to make this problem treatable, such as by means of the crystal structure periodicity and the Bloch theorem [52, 53, 54]. However, the coupled electrons remain a problem, even with few electrons in the unit cell. In this way, the DFT proposes a simpler way to describe the system properties. Instead of looking only for the wavefunction, the electronic charge density has the main focus in this new analysis. Additionally, a "system replacement" is performed, which significantly simplify the analysis of the problem and reduces the computational cost, as we will discuss in the next section.

2.1 Density Functional Theory

The arise and consolidation of the DFT provided a revolution in modern physics and chemistry. The DFT is based on the investigation of the system ground state electronic charge density, instead of its wavefunction properly. This theory is based on two theorems and, due to the impacts in computational materials simulation, Walter Kohn and John Pople were awarded with the nobel prize in chemistry in 1998. The DFT is an exact theory, and provides exactly results for simple systems, such as free electrons gas. However, as we will discuss next, to describe one of the terms in real materials, some approximations are required, which leads to a approximated results in most of cases.

2.1.1 Hohenberg-Kohn theorems

Considering a nonrelativistic treatment for a given system with N interacting electrons in the non-degenerated ground state, the first theorem shows a univocal connection between the electronic density and the external potential [49].

First theorem: *The external potential V_n is uniquely determined, less an additive constant, by the electronic density of the ground state $n(\boldsymbol{r})$.*

This first theorem leads to important implications. Since the ground state charge density allows us to investigate the external potential, all the terms in the Hamiltonian (4) can be determined. With the external potential and the Hamiltonian from Eq.(4), we can obtain the corresponding ground state many-electron wavefunction Ψ. With the ground state wavefunction, the last step consists of determining the system's eigenenergies, which leads to the following relation

$$n(\boldsymbol{r}) \rightarrow V_n \rightarrow \Psi \rightarrow E.$$

Since the electronic density depends on the position $\boldsymbol{r}$, the ground state energy is a density functional. In the functional notation, this relation can be expressed as

$$E = F[n(\boldsymbol{r})]. \tag{5}$$

Second theorem: *The energy of a ground state is minimum for the exact ground state electronic density.*

As previously mentioned in the discussion of theorem 1, since the external potential is uniquely determined by the ground state electronic density, the ground state wavefunction can be obtained from the electronic density. However, by applying an external effect, the many-electron wavefunction will change, and it is not determined only by the ground state of electron density. This is intrinsically related to the second theorem, which states that any wavefunction that does not lead to the minimum mean energy value corresponds to a excited electron density $n'(\boldsymbol{r})$. This auxiliary electronic density leads to an external potential and, consequently, to a wavefunction. The mean value of the Hamiltonian will leads to higher energy values.

$$E[n(\boldsymbol{r})] = \langle \Psi | H | \Psi \rangle < \langle \Psi' | H | \Psi' \rangle, \tag{6}$$

Which leads to

$$E[n(\boldsymbol{r})] < E[n'(\boldsymbol{r})]. \tag{7}$$

2.1.2 Kohn-Sham *Ansatz*

Although the Hohenberg-Kohn theorems give valuable insights regarding the electronic density of the ground state, the associated calculations can be quite complicated due to the interacting electrons. In this context, one of the key advantages of DFT is the representation of the original system by an auxiliary system that consists of N non-interacting electrons under an effective potential. This change in representation is based on the Kohn-Sham *Ansatz*, where relies on two premises [55]:

1 - Non-interacting-V-representability: This assumption consist in the statement that the ground-state electronic density of an interacting system can be described by the

ground-state electronic density of a non-interacting auxiliary system under an effective potential.

2 - Auxiliary Kohn-Sham Hamiltonian H_{KS}: The auxiliary Kohn-Sham Hamiltonian is constructed including the kinetic energy of the non-interacting N electrons and an auxiliary potential, which we denote as the Kohn-Sham potential. This H_{KS} Hamiltonian assumes the following form

$$H_{KS} = \sum_{i}^{N} \left(-\frac{1}{2}\nabla_i^2 \right) + \sum_{i}^{N} V_{KS}(\boldsymbol{r}_i). \tag{8}$$

The electronic system is fermionic, and its wavefunction must be antisymmetric. We can express the ground-state wavefunction of the auxiliary non-interacting system in the Slater determinant form

$$\Phi_{KS} = \frac{1}{\sqrt{N!}} \begin{vmatrix} \phi_1(\boldsymbol{r}_1) & \phi_2(\boldsymbol{r}_1) & \cdots & \phi_N(\boldsymbol{r}_1) \\ \phi_1(\boldsymbol{r}_2) & \phi_2(\boldsymbol{r}_2) & \cdots & \phi_N(\boldsymbol{r}_2) \\ \vdots & \vdots & \ddots & \vdots \\ \phi_1(\boldsymbol{r}_N) & \phi_2(\boldsymbol{r}_N) & \cdots & \phi_N(\boldsymbol{r}_N) \end{vmatrix}. \tag{9}$$

In this way, using the variable separation methods, we obtain N eigenvalues equation for the electrons

$$h_{KS}\phi_i = \epsilon_i \phi_i. \tag{10}$$

The auxiliary Hamiltonian assumes the form of a single particle under an effective potential, defined as

$$h_{KS} = -\frac{\nabla^2}{2} + V_{KS}(\boldsymbol{r}). \tag{11}$$

In this way, we replace a problem of many interacting electrons by a non-interacting system with the electrons under an effective potential. In this auxiliary system, the wavefunction depends only on the free electrons spatial coordinates. There are additional steps that are helpful in the materials context. The solids can exhibit the atomic alignment in a crystalline form, which shows a periodicity and the wavefunction differs only by a phase, reducing the analysis of the system to its unit cell. In the next section, we discuss how to construct a functional that minimizes the ground state energy and derive the Kohn-Sham equations.

2.1.3 Kohn-Sham equations

In the previous section, the Hohenberg-Kohn theorems were studied. These theorems provide valuable insights regarding the study of systems in their ground state, where the ground state energy is expressed in terms of the electronic density. However, the exact form of this functional is not explicitly defined and remains an open topic in condensed matter physics. In this section, we will explore the general form of this functional.

Based on the Hohenberg-Kohn theorems and the Kohn-Sham *ansatz*, we can construct a functional that minimizes the total energy of the system, given the exact ground state electronic density. This functional must include contributions from the kinetic energy, the Coulomb interaction and external potential. This ground state energy can be written as

$$E = min_{n(\boldsymbol{r})} \{T[n] + W[n] + V_n[n]\} = min_{n(\boldsymbol{r})} \left[F[n] + \int n(\boldsymbol{r}) V_{ext}(\boldsymbol{r}) d\boldsymbol{r}\right]. \tag{12}$$

Here, F[n] denotes the universal functional, which contains the kinetic energy and Coulomb interaction terms, present in all many-electron systems. The other term is the external potential due do the nuclei-electron interaction.

All terms in the universal functional are dependent on the electronic density. However, for the kinetic energy, this dependence is implicit expressed through the Kohn-Sham orbitals. The kinetic energy is given by

$$T[n] = -\frac{1}{2} \sum_i \int \phi_i^*(\boldsymbol{r}) \nabla^2 \phi_i(\boldsymbol{r}) d\boldsymbol{r}. \tag{13}$$

The classical electronic repulsion, given in terms of the Hartree energy [49], has the form

$$E_H[n] = \frac{1}{2} \iint \frac{n(\boldsymbol{r}) n(\boldsymbol{r'})}{|\boldsymbol{r} - \boldsymbol{r'}|} d\boldsymbol{r} d\boldsymbol{r'}. \tag{14}$$

By means of the described interactions, and the external potential, we can rewrite the energy expression (12) in the following format

$$E[n] = T[n] + E_H[n] + V_n[n] + E_{xc}[n]. \tag{15}$$

It is worth to note that an additional term (E_{xc}) was included in the previous equation. This term is named the exchange and correlation energy, and all interactions beyond the kinetic energy and Coulomb interaction are incorporated into this term. A closed expression for this term remains one of the greatest challenges in modern density functional theory [51]. The nature of this term and further approximations will be discussed in a detail in the next section.

The energy as a functional of the electronic density (Eq. (15)) can be rewritten, using Eqs. (13) and (14), in the full expanded terms as

$$E[n] = -\frac{1}{2} \sum_i \int \phi_i^*(\boldsymbol{r}) \nabla^2 \phi_i(\boldsymbol{r}) d\boldsymbol{r} + \frac{1}{2} \iint \frac{n(\boldsymbol{r}) n(\boldsymbol{r'})}{|\boldsymbol{r} - \boldsymbol{r'}|} d\boldsymbol{r} d\boldsymbol{r'} + \int n(\boldsymbol{r}) V_{ext}(\boldsymbol{r}) d\boldsymbol{r} + E_{xc}[n]. \tag{16}$$

The condition to minimizing the Kohn-Sham auxiliary system functional can be viewed as a minimization problem with respect to the electronic density. We can solve this problem using of the Lagrange functional method

$$L = E[n] - \sum_{ij} \left[\epsilon_{ij} \int \phi_i^*(\boldsymbol{r}) \phi_j(\boldsymbol{r}) d(\boldsymbol{r}) - \delta_{ij}\right]. \tag{17}$$

Using the functional expression from Eq. (15), we can rewrite the Eq. (17) as

$$L = T[n] + E_H[n] + V_n[n] + E_{xc}[n] - \sum_{ij}\left[\epsilon_{ij}\int \phi_i^*(\boldsymbol{r})\phi_j(\boldsymbol{r})d(\boldsymbol{r}) - \delta_{ij}\right]. \tag{18}$$

The orthogonality condition between the orbitals i and j implies that

$$\int \phi_i^*(\boldsymbol{r})\phi_j(\boldsymbol{r})d(\boldsymbol{r}) = \delta_{ij}. \tag{19}$$

In searching for a ground-state density that minimizes the functional, we apply the Hohenberg-Kohn variational principle, described as

$$\frac{\delta L}{\delta\phi_i^*(\boldsymbol{r})} = 0, \tag{20}$$

or, using (18)

$$\frac{\delta T[n]}{\delta\phi_i^*(\boldsymbol{r})} + \frac{\delta}{\delta\phi_i^*(\boldsymbol{r})}\left[E_H[n] + V_n[n] + E_{xc}[n]\right] = \frac{\delta}{\delta\phi_i^*(\boldsymbol{r})}\sum_i \epsilon_i \int \phi_i^*(\boldsymbol{r})\phi_i(\boldsymbol{r})d(\boldsymbol{r}). \tag{21}$$

By performing the functional derivative [1] of the first term on the left-hand side and the term on the right-hand side of the previous equation, we obtain

$$\frac{\delta T[n]}{\delta\phi_i^*(\boldsymbol{r})} = \frac{\delta}{\delta\phi_i^*(\boldsymbol{r})}\left[-\frac{1}{2}\sum_i \int \phi_i^*(\boldsymbol{r})\nabla^2\phi_i(\boldsymbol{r})d\boldsymbol{r}\right] = -\frac{1}{2}\nabla^2\phi_i(\boldsymbol{r}). \tag{22}$$

Rewriting Eq. (21) using the results from the functional derivative, we have

$$-\frac{1}{2}\nabla^2\phi_i(\boldsymbol{r}) + \frac{\delta}{\delta\phi_i^*(\boldsymbol{r})}\left[E_H[n] + V_n[n] + E_{xc}[n]\right] = \epsilon_i\phi_i(\boldsymbol{r}). \tag{23}$$

A useful property of the corresponding functional derivative in this context is

$$\frac{\delta f}{\delta\phi_i^*(\boldsymbol{r})} = \frac{\delta f}{\delta n}\frac{\delta n}{\delta\phi_i^*(\boldsymbol{r})} = \frac{\delta f}{\delta n}\phi_i(\boldsymbol{r}). \tag{24}$$

By applying the previous property into Eq. (23)

$$-\frac{\nabla^2}{2}\phi_i(\boldsymbol{r}) + \frac{\delta}{\delta n}\left[E_H[n] + V_n[n] + E_{xc}[n]\right]\phi_i(\boldsymbol{r}) = \epsilon_i\phi_i(\boldsymbol{r}). \tag{25}$$

The derivatives of $E_H[n]$ and $E_{xc}[n]$ with respect to the electron density correspond to the respective potentials, where we substitute (25) into the final expression and, since that $\frac{\delta V_n[n]}{\delta n} = V_{ext}(\boldsymbol{r})$, we verify the following equation

$$\left[-\frac{\nabla^2}{2} + V_{ext}(\boldsymbol{r}) + V_H(\boldsymbol{r}) + V_{xc}(\boldsymbol{r})\right]\phi_i(\boldsymbol{r}) = \epsilon_i\phi_i(\boldsymbol{r}). \tag{26}$$

[1] Considering a functional with follows the form

$$F[\alpha] = \int f(\boldsymbol{r}, \alpha(\boldsymbol{r}))d\boldsymbol{r},$$

The derivative of the functional can be expressed as

$$\frac{\delta F[\alpha]}{\delta\alpha} = \frac{\delta f}{\delta\alpha}.$$

In compact form, we can rewrite the Eq.(26) as a single-particle Schrödinger equation under a effective Kohn-Sham potential

$$\left[-\frac{\nabla^2}{2} + V_{KS}(\boldsymbol{r})\right]\phi_i(\boldsymbol{r}) = \epsilon_i\phi_i(\boldsymbol{r}). \tag{27}$$

Where

$$V_{KS}(\boldsymbol{r}) = V_{ext}(\boldsymbol{r}) + V_H(\boldsymbol{r}) + V_{xc}(\boldsymbol{r}), \tag{28}$$

$$\nabla^2 V_H(\boldsymbol{r}) = -4\pi n(\boldsymbol{r}), \tag{29}$$

$$n(\boldsymbol{r}) = \sum_i |\phi_i(\boldsymbol{r})|^2. \tag{30}$$

The Equations (27) and (30) are known as the Kohn-Sham equations [56], which provides a revolutionary way to investigate the electronic properties of the materials. It is important to note that, to obtain the ground-state electronic density, the Kohn-Sham orbitals are required for the calculations, as stated by Eq. (30). However, to calculate the Kohn-Sham orbitals (Eq. (27)), the effective potential from Eq. (28) is required, which depends on the ground-state electronic density expression.

In practice, the Kohn-Sham equations are solved numerically through self-consistent calculations. This method consists in perform an initial guess for the electronic density, where the effective potential is calculated. Using this potential, the Kohn-Sham equation (27) can be solved. This solution enables the calculation of a new electronic density, which can be compared to the old charge density, from the initial guess. If the difference between the new and old densities is lower than a fixed tolerance criterion, the calculation can be stopped. If not, the full cycle is repeated with the new estimated density until the criterion is reached. This initial guess for the electron density is usually obtained from the sum of the charges of the materials isolated atoms.

2.2 Functionals and Approximations

In the previous section, we derived the Kohn-Sham equations using the Kohn-Sham *ansatz*, which replaces the interacting many-electrons system by a non-interacting system under an effective potential. In the effective potential, all the effects that are not accounted for the kinetic energy and Coulomb interaction are included in the exchange and correlation energy [49, 55].

The exchange-correlation term is given by the sum of two distinct contributions: exchange energy and correlation energy. The exchange energy arises from the Pauli's exclusion principle. Since electrons are fermions, their wavefunction must be antisymmetric. As a result, two electrons with the same spin orientation cannot occupy the same energy level, only opposite spins are allowed. This leads to an energetic cost associated with exchanging electrons between orbitals. Although the exchange integrals are computationally expensive, it has a closed expression derived from the Hartree-Fock equations [49, 55].

On the other hand, the correlation energy originates from many-body effects. The probability of finding an electron at a given position decreases when other electrons are nearby. Similarly, a single electron influences the overall electronic distribution, and vice versa. Unlike the exchange term, the correlation term does not have a closed-form expression. Its nature is complex, as it affects both the kinetic and potential energies of the system.

In this way, approximations are necessary to address the problem. Two widely used approaches are the local density and generalized gradient approximations, as will be discussed next.

2.2.1 Local density approximation

A first proposal for solution of the exchange and correlation term is the local density approximation (LDA). This approach was proposed by Kohn and Sham in their seminal paper [56] and provides a foundational framework for further approximations. The LDA simplifies the electronic density by assuming it to be homogeneous, based on free homogeneous electrons gas model. This simplification makes it possible to investigate the exchange and correlation energy in a physically accessible way. In this approximation, the exchange and correlation energy can be expressed as

$$E_{xc}[n] = \frac{1}{2}\int n(\boldsymbol{r})[\epsilon_x^{LDA} + \epsilon_c^{LDA}]d\boldsymbol{r}. \tag{31}$$

Where $\epsilon_{x(c)}^{LDA}$ is the exchange (correlation) energy in the LDA. Under this approximation, an analytic expression for the exchange energy can be derived, which it is given by

$$\epsilon_x^{LDA} = -\frac{3}{4}\left[\frac{3}{\pi}\right]^{\frac{1}{3}}\int_V n(\boldsymbol{r})^{\frac{4}{3}}d\boldsymbol{r}. \tag{32}$$

While the exchange energy has a closed-form expression, the correlation energy does not have an analytical expression. This term can be studied using numerical methods, such as Monte Carlo simulations [55, 49, 57].

The LDA successfully describes systems with uniform electronic density. However, for non-homogeneous systems, where the electronic density varies significantly, a more sophisticated approach is required. This leads to the generalized gradient approximation (GGA).

2.2.2 Generalized gradient approximation

In the search for a more accurate approach to describe the ground state electronic density, it is required to take into account non-uniform effects. In this context, the generalized gradient approximation represents an improvement over the LDA approach. Unlike LDA, which accurately describes only systems with homogeneous electronic density, GGA

also incorporates the gradient effects of the electron density, providing a more accurate description for the systems. The exchange and correlation functional in GGA has the form

$$E_{xc}[n(\boldsymbol{r})] = \int f^{GGA}(n(\boldsymbol{r}), \nabla n(\boldsymbol{r}))d\boldsymbol{r}. \tag{33}$$

Here, f^{GGA} is a function of the electronic density and its gradient. It is important to note that simply incorporating the gradient of the electronic density is not sufficient to achieve significant improvements in accuracy compared to LDA, which requires the inclusion of other terms in the expansion [55, 58]. Under this approach, the correlation term is described as

$$E_c^{GGA}[n(\boldsymbol{r})] = \int n(\boldsymbol{r})[\epsilon_c^{LDA} + H(n(\boldsymbol{r}), t)]d\boldsymbol{r}. \tag{34}$$

Where ϵ_c^{LDA} represents the correlation energy obtained within the LDA framework. The function $H(n(\boldsymbol{r}), t)$ incorporates the expanded gradient terms. Classic GGA functionals include the Becke-Lee-Yang-Parr (BLYP) [59, 60], Perdew-Wang (PW) [61], and Perdew-Burke-Ernzerhof (PBE) [62] functionals, with PBE being one of the most widely used in DFT calculations.

2.2.3 DFT+U

Although GGA approaches can sufficiently describe a large class of materials, there is one class of system that these standard DFT approximations fails to describe with reasonable accuracy. In systems that exhibit strong electronic correlation, these methods fail, leading to divergence with experimental results [63, 64, 65]. Strongly correlated electrons arises in well-localized d and f orbitals, where, without a correct treatment, wrong results are reported [55, 58, 66]. In many systems, without many-electron correction, they exhibit metallic behavior, but with the correction they may show insulating behavior. These systems are known as Mott insulators [30, 67, 68]. The correction, known as DFT+U, incorporates many-electron effects through an externally added Coulomb term (U).

This new approach lies in the Hubbard model. Here, a correction term is introduced in the total energy of the standard exchange and correlation term, such as LDA, GGA or meta-GGA. The new energy under this consideration reads as

$$E_{LDA+U}[n(\boldsymbol{r})] = E_{LDA}[n(\boldsymbol{r})] + E_{Hub}[n^{l,\sigma}_{m_1,m_2}] - E_{dc}[n^{l,\sigma}]. \tag{35}$$

The Hubbard term (E_{Hub}) denotes the correction term, which depends of the occupation number (n) of the spin electrons (σ) at a given atomic site (l), in the m-th state. However, part of the electronic correlation, even that is not completely described, is included on the E_{LDA} functional. To correct this issue, the E_{dc} is introduced to avoid double counting terms.

A largely used functional from DFT+U context was introduced by Dudarev [63], where it is taken only the difference between U and J terms, the energy expression under this method is given by

$$E_{LDA+U}[n(\boldsymbol{r})] = E_{LDA}[n(\boldsymbol{r})] + \frac{(U_{eff})}{2} \sum_{m,\sigma} \left[n_{m,\sigma} - n_{m,\sigma}^2 \right]. \tag{36}$$

Where $U_{eff} = U - J$. There are some ways to estimate the effective U term. One of them is by adjusting this parameter until the properties matches with the experimental findings, such as lattice parameter or orbital localization. Computationally, different approaches are developed to estimate this parameter, such as linear response method [69].

2.3 Spin density functional theory

Throughout this chapter, although was given indirect physical insights regarding spin inclusion, there was no formal treatment of this physical property within DFT. Without considering spin, a wide class of phenomena cannot be accurately described by this theory, including magnetic materials, topological insulators, quantum anomalous Hall systems, and Rasbha effects. Therefore, a complete DFT framework requires the explicit inclusion of spin.

The inclusion of magnetism in DFT is closely related to special relativity and the Pauli exclusion principle, which states that two electrons with the same spin cannot occupy the same energy level. A formal treatment of spin density functional theory was developed by Rajagopal and Callaway [70]. In the special relativity context, using the Dirac equation, they demonstrated that the total energy of the system in the ground state is a functional of the four-current $J_\mu(\boldsymbol{r})$. This four-current include information from the electronic density (n($\boldsymbol{r}$)), the electron spin density ($\boldsymbol{s}(\boldsymbol{r})$), and current densities.

- Without magnetic properties: $n(\boldsymbol{r}) \xrightarrow{F} E$, $E = F[n(\boldsymbol{r})]$
- With magnetic properties: $n(\boldsymbol{r}), \boldsymbol{s}(\boldsymbol{r}) \xrightarrow{G} E$, $E = G[n(\boldsymbol{r}), \boldsymbol{s}(\boldsymbol{r})]$.

Unlike the spinless case, in this context, the total energy has a functional form that depends not only on the electron density, but also on the spin density. These physical properties are defined by

$$n(\boldsymbol{r}) = n(\boldsymbol{r}, \sigma = \uparrow) + n(\boldsymbol{r}, \sigma = \downarrow), \tag{37}$$

$$\boldsymbol{s}(\boldsymbol{r}) = n(\boldsymbol{r}, \sigma = \uparrow) - n(\boldsymbol{r}, \sigma = \downarrow). \tag{38}$$

Here, $\uparrow$ e $\downarrow$ denote spin-up and spin-down states, respectively. In this way, the electronic density can be rewritten as

$$n(\boldsymbol{r}) = \sum_i |\phi_i(\boldsymbol{r}, \uparrow)|^2 + \sum_i |\phi_i(\boldsymbol{r}, \downarrow)|^2. \tag{39}$$

We can rewrite the Kohn-Sham equation (Eq. (27)) in terms of the spin components as

$$\left[-\frac{1}{2}\nabla^2 + V_n(\boldsymbol{r}) + V_H(\boldsymbol{r}) + V_{xc,\sigma}(\boldsymbol{r})\right]\phi_{i,\sigma}(\boldsymbol{r}) = \epsilon_{i,\sigma}\phi_{i,\sigma}(\boldsymbol{r}). \tag{40}$$

Where the exchange and correlation potential is given by

$$V_{xc,\sigma}(\boldsymbol{r}) = \frac{\delta E_{xc}[n_\uparrow, n_\downarrow]}{\delta n_\sigma(\boldsymbol{r})}. \tag{41}$$

To generalize the Kohn-Sham equation, it is necessary to use a spinor description, where

$$\Psi_i(\boldsymbol{r}) = \phi_i(\boldsymbol{r}, \uparrow)\chi_\uparrow + \phi_i(\boldsymbol{r}, \downarrow)\chi_\downarrow. \tag{42}$$

In this formulation, the correlation and exchange terms are separated into a classical sum, with the magnetic field also included

$$\left[-\frac{1}{2}\nabla^2 + V_n(\boldsymbol{r}) + V_H(\boldsymbol{r}) + V_{xc}(\boldsymbol{r}) + \mu\boldsymbol{\sigma}\cdot\boldsymbol{B}_{xc}(\boldsymbol{r})\right]\Psi_i(\boldsymbol{r}) = \epsilon_i\Psi_i(\boldsymbol{r}). \tag{43}$$

The term $\boldsymbol{B}_{xc}(\boldsymbol{r})$ is defined as the exchange and correlation magnetic field, which aligns the electrons and leads to magnetic ordering.

2.4 Berry Phase

In the study of topological states of matter, a key concept used for computing topological invariants is the Berry phase and its derived quantities, such as the Berry curvature and Berry connection. The Berry phase arises in systems that perform a closed path under an adiabatically evolution. Previously, it was believed that a quantum system under an adiabatic evolution did not carry any information accumulated in the evolution, and only the dynamical phase would manifest. However, Michael V. Berry [71] demonstrates that, in a closed path, this system carries a phase due to geometric effects. This phase, also known as the geometric phase, has applications in different physics areas, such as solid state physics and electrodynamics [72, 73, 74].

We analyze a physical system that intrinsically depends on the $\mathbf{R}$ parameter, where $\boldsymbol{R} = (R_1, R_2, ..., R_N)$, and is also time dependent, denoted by t. The evolution of the $\mathbf{R}$ parameter is smoothly and the system is not exposed to significant perturbations in a given time $t = T$. The system Hamiltonian can be expressed as $H(\boldsymbol{R}(t))$, with the corresponding eigenenergies denoted by $E_n(\boldsymbol{R}(t))$. The n-th eigenstate of this Hamiltonian is described by the ket $|n(\boldsymbol{R}(t))\rangle$. By using the Schrödinger's equation at a given time t, we rewrite the expression as

$$H(\boldsymbol{R}(t))|n(\boldsymbol{R}(t))\rangle = E_n(\boldsymbol{R}(t))|n(\boldsymbol{R}(t))\rangle. \tag{44}$$

At an initial time, which is fixed at $t = 0$, we denote $\boldsymbol{R}(0) = \boldsymbol{R}_0$. By rewriting the Schrödinger's equation (44) in its time-dependent form for an initial state, we have

$$H(\boldsymbol{R}(t))|n(\boldsymbol{R}_0)\rangle = i\hbar\frac{\partial}{\partial t}|n(\boldsymbol{R}_0)\rangle. \tag{45}$$

From the perspective of time evolution and dynamical evolution of the system, the eigenstate $|n(\boldsymbol{R}(t))\rangle$ at the initial time can be rewritten as

$$|n(\boldsymbol{R}_0)\rangle = e^{i\alpha_n(t)}e^{i\gamma_n(t)}|n(\boldsymbol{R}(t))\rangle, \tag{46}$$

here $\alpha_n(t)$ corresponds to the dynamical phase. The system that is already in his eigenstate, by suffering the time variation, and without perturbation, due to time evolution this system will be finding in its eigenstate less due to a phase, that is the dynamical phase, given by

$$\alpha_n(t) = -\frac{1}{\hbar}\int E_n dt. \tag{47}$$

When we perform the substitution of Eq. (47) into Eq. (46) and, by considering the eigenvalues form (Eq. (45)), we obtain

$$E_n\left[e^{-\frac{i}{\hbar}\int E_n dt}e^{i\gamma_n(t)}\right]|n(\boldsymbol{R}(t))\rangle = i\hbar\frac{\partial}{\partial t}\left[e^{-\frac{i}{\hbar}\int E_n dt}e^{i\gamma_n(t)}\right]|n(\boldsymbol{R}(t))\rangle. \tag{48}$$

By taking the derivative in the right-hand side of the previous equation, we obtain

$$i\hbar\left\{\left[-\frac{i}{\hbar}E_n + i\frac{\partial}{\partial t}\gamma_n(t)\right]e^{-\frac{i}{\hbar}\int E_n dt}e^{i\gamma_n(t)}|n(\boldsymbol{R}(t))\rangle + e^{-\frac{i}{\hbar}\int E_n dt}e^{i\gamma_n(t)}\frac{\partial}{\partial t}|n(\boldsymbol{R}(t))\rangle\right\}. \tag{49}$$

In this way, with the simplification of the exponential terms, the Eq. (48) can be rewritten as

$$E_n|n(\boldsymbol{R}(t))\rangle = i\hbar\left[-\frac{i}{\hbar}E_n + i\frac{d}{dt}\gamma_n(t) + \frac{d}{dt}\right]|n(\boldsymbol{R}(t))\rangle. \tag{50}$$

By applying $\langle n(\boldsymbol{R}(t))|$ on both sides of (50), and using the normalization condition $\langle n(\boldsymbol{R}(t))|n(\boldsymbol{R}(t))\rangle = 1$, it can be noted that

$$\frac{d}{dt}\gamma_n(t) = i\langle n(\boldsymbol{R}(t))|\frac{d}{dt}|n(\boldsymbol{R}(t))\rangle. \tag{51}$$

With the following derivative property

$$\frac{d}{dt}|n(\boldsymbol{R}(t))\rangle = \nabla_{\boldsymbol{R}}|n(\boldsymbol{R}(t))\rangle \cdot \frac{d\boldsymbol{R}}{dt}, \tag{52}$$

we can rewrite the previous equation as

$$\frac{d}{dt}\gamma_n(t) = i\langle n(\boldsymbol{R}(t))|\nabla_{\boldsymbol{R}}|n(\boldsymbol{R}(t))\rangle\frac{d\boldsymbol{R}}{dt}. \tag{53}$$

The term $i\langle n(\boldsymbol{R}(t))|\nabla_{\boldsymbol{R}}|n(\boldsymbol{R}(t))\rangle$ is named as the Berry connection, here represented by $\boldsymbol{A}_n(\boldsymbol{R}(t))$. By performing the integral from 0 to T on both sides of the previous equation, which is the time which the adiabatic motion is performed, we obtain

$$\gamma_n(T) = \int_{\boldsymbol{R}(0)}^{\boldsymbol{R}(T)} \boldsymbol{A}_n(\boldsymbol{R}(t)) \cdot d\boldsymbol{R}. \tag{54}$$

For a closed loop, in a given time T, the system return to the initial position, $\boldsymbol{R}(T) = \boldsymbol{R}_0$. This leads to the Berry phase expression

$$\gamma_n(C) = \oint_C \boldsymbol{A}_n(\boldsymbol{R}) \cdot d\boldsymbol{R}. \tag{55}$$

The previous expression can be rewritten using Stokes' theorem, where the Berry phase is expressed as a surface integral of the Berry connection curl

$$\gamma_n(C) = \int_S \boldsymbol{\Omega}_n(\boldsymbol{R}) \cdot d\boldsymbol{S}. \tag{56}$$

Here $\boldsymbol{\Omega}_n$ is defined as the Berry curvature, which is given as $\boldsymbol{\Omega}_n(\boldsymbol{R}) = \nabla_{\boldsymbol{R}} \times \boldsymbol{A}_n(\boldsymbol{R})$. As will be discussed in the Chapter 3, the Berry phase and Berry curvature exhibit key properties in the context of topological systems. Based on this, we revisit the Berry curvature expression, where we rewrite in the following form

$$\nabla_{\boldsymbol{R}} \times \boldsymbol{A}_n(\boldsymbol{R}) = \mathrm{Im}\{\nabla_{\boldsymbol{R}} \times [\langle n(\boldsymbol{R})|\nabla_{\boldsymbol{R}}|n(\boldsymbol{R})\rangle\}. \tag{57}$$

By applying the curl property $\nabla \times [f(\boldsymbol{r})\nabla g(\boldsymbol{r})] = \nabla f(\boldsymbol{r}) \times \nabla g(\boldsymbol{r})$, we can rewrite the Berry curvature as

$$\boldsymbol{\Omega}_n = \mathrm{Im}\{\nabla_{\boldsymbol{R}}\langle n(\boldsymbol{R})| \times |\nabla_{\boldsymbol{R}}|n(\boldsymbol{R})\rangle\}. \tag{58}$$

By inserting the completeness relation, we have

$$\boldsymbol{\Omega}_n = \mathrm{Im}\left\{\sum_{m\neq n} \nabla_{\boldsymbol{R}}\langle n(\boldsymbol{R})|m(\boldsymbol{R})\rangle \times \langle m(\boldsymbol{R})|\nabla_{\boldsymbol{R}}|n(\boldsymbol{R})\rangle\right\}. \tag{59}$$

To verify the off-diagonal elements, where m≠n, we revisit the Schrödinger equation. We apply the $\nabla_{\boldsymbol{R}}$ operator in Eq. (44), leading to

$$\nabla_{\boldsymbol{R}}H(\boldsymbol{R})|n(\boldsymbol{R})\rangle + H(\boldsymbol{R})\nabla_{\boldsymbol{R}}|n(\boldsymbol{R})\rangle = \nabla_{\boldsymbol{R}}E(\boldsymbol{R})|n(\boldsymbol{R})\rangle + E_n(\boldsymbol{R})\nabla_{\boldsymbol{R}}|n(\boldsymbol{R})\rangle \tag{60}$$

By projecting into $\langle m(\boldsymbol{R})|$ state, we obtain

$$\langle m(\boldsymbol{R})|\nabla_{\boldsymbol{R}}|n(\boldsymbol{R})\rangle = \frac{\langle m(\boldsymbol{R})|\nabla_{\boldsymbol{R}}H(\boldsymbol{R})|n(\boldsymbol{R})\rangle}{(E_n - E_m)} \tag{61}$$

Note that this result can be applied to Eq. (59), where the Berry curvature can be rewritten as

$$\boldsymbol{\Omega}_n = \mathrm{Im}\left\{\sum_{m\neq n} \frac{\langle n(\boldsymbol{R})|\nabla_{\boldsymbol{R}}H(\boldsymbol{R})|m(\boldsymbol{R})\rangle \times \langle m(\boldsymbol{R})|\nabla_{\boldsymbol{R}}H(\boldsymbol{R})|n(\boldsymbol{R})\rangle}{(E_m(\boldsymbol{R}) - E_n(\boldsymbol{R}))^2}\right\}. \tag{62}$$

It is worth to note that this Berry curvature expression can also be expressed in terms of the velocity operator [75, 76].

2.5 Wannier functions

One of the intuitive ways to calculate topological invariants is by integrating the Berry connection over the Brillouin zone. Although the Berry phase provides a useful way to analytically calculate the topological phase of systems and is successfully applied in particular cases, such as in two-level systems, its computational implementation is

challenging. This is because the Berry connection depends on the gauge choice, and fixing the gauge is non-trivial. Alternatively, the parity of wavefunctions can be used to compute the topological invariant, however, this method is restricted to centrosymmetric systems. In this context, Wannier functions offer a more straightforward approach for computing topological invariants.

The Wannier functions are strictly related to the Bloch Functions and were introduced by Grigori Wannier in 1937. These functions show a strong correspondence with tigh-binding models [77], and are defined as

$$|w_{n\boldsymbol{R}}\rangle = \frac{V_{cell}}{(2\pi)^3}\int_{BZ} e^{-i\boldsymbol{k}\cdot\boldsymbol{R}}|u_{n\boldsymbol{k}}\rangle d\boldsymbol{k}. \tag{63}$$

Here, V_{cell} corresponds to the volume of the unit cell, BZ denotes the Brillouin zone of the system as the integration limit, and $|u_{n\boldsymbol{k}}\rangle$ represents the Bloch states. By performing the Fourier transform (FT), it can be obtained the Bloch functions in terms of the Wannier counterpart

$$|u_{n\boldsymbol{k}}\rangle = \sum_{\boldsymbol{R}} e^{i\boldsymbol{k}\cdot\boldsymbol{R}}|w_{n\boldsymbol{R}}\rangle. \tag{64}$$

Clearly, by performing the inverse Fourier transform, the Wannier functions can once again be expressed in terms of the Bloch functions, as follows

$$|w_{n\boldsymbol{R}}\rangle = \frac{V_{cell}}{(2\pi)^3}\int_{BZ} e^{-i\boldsymbol{k}\cdot\boldsymbol{R}}|u_{n\boldsymbol{k}}\rangle d\boldsymbol{k} \qquad \overset{FT}{\Longleftrightarrow} \qquad |u_{n\boldsymbol{k}}\rangle = \sum_{\boldsymbol{R}} e^{i\boldsymbol{k}\cdot\boldsymbol{R}}|w_{n\boldsymbol{R}}\rangle. \tag{65}$$

One of the main advantages of using Wannier functions is the ability to define the Wannier charge centers (WCC). The WCC represent the expectation value of the position operator for the Wannier functions

$$\overline{\boldsymbol{r}}_n = \langle w_{n\boldsymbol{0}}|\boldsymbol{r}|w_{n\boldsymbol{0}}\rangle. \tag{66}$$

Through this definition, the WCC are equal to the Fourier transform coefficients of the Berry connection, establishing a direct relationship between the Wannier charge centers and the geometric properties of the electronic states

$$\langle w_{n\boldsymbol{0}}|\boldsymbol{r}|w_{n\boldsymbol{R}}\rangle = \boldsymbol{A}_{n\boldsymbol{R}}. \tag{67}$$

Similarly to the Bloch states wavefunctions, we can define

$$\boldsymbol{A}_{n\boldsymbol{R}} = \frac{V_{cell}}{(2\pi)^3}\int_{BZ} e^{-i\boldsymbol{k}\cdot\boldsymbol{R}}\boldsymbol{A}_n(\boldsymbol{k})d\boldsymbol{k} \qquad \overset{FT}{\Longleftrightarrow} \qquad \boldsymbol{A}_n(\boldsymbol{k}) = \sum_{\boldsymbol{R}} e^{i\boldsymbol{k}\cdot\boldsymbol{R}}\boldsymbol{A}_{n\boldsymbol{R}}. \tag{68}$$

By substituting Eq. (68) into Eq. (67), and considering $\boldsymbol{R} = 0$ as the origin of coordinates, we can verify the relation between the WCC and the Berry connection as

$$\overline{\boldsymbol{r}}_n = \frac{V_{cell}}{(2\pi)^3}\int_{BZ} \boldsymbol{A}_n(\boldsymbol{k})\cdot d\boldsymbol{k}, \tag{69}$$

Using the definition of $\boldsymbol{A}_n(\boldsymbol{k})$, the previous equation can rewritten as

$$\overline{\boldsymbol{r}}_n = \frac{V_{cell}}{(2\pi)^3}\int_{BZ} i\langle u_{n\boldsymbol{k}}|\nabla_{\boldsymbol{k}}|u_{n\boldsymbol{k}}\rangle d\boldsymbol{k}. \tag{70}$$

Restricting this previous equation to the 1D case, where the integral over the Brillouin zone reduces to the interval from 0 to $2\pi/a$, and replacing the unit cell volume with the lattice parameter a, we obtain

$$\overline{x}_n = \left(\frac{a}{2\pi}\right)\int_0^{\frac{2\pi}{a}} \langle u_{nk}|i\partial_k|u_{nk}\rangle dk, \tag{71}$$

It can be noted that this integral corresponds to the Berry phase expression, defined in Eq. (55), applied to the 1D system. We can rewrite as

$$\overline{x}_n = a\frac{\gamma_n}{2\pi}. \tag{72}$$

This leads to a direct relationship between the Wannier charge centers and the Berry phase, differing only by a factor. In this case, calculating the WCC along a path from 0 to a is analogous to calculating the Berry phase from 0 to 2π path. One useful quantity is the sum of the Wannier charge center over the Brillouin zone, which plays a key role in determining the Z_2 topological invariant. Unlike the Berry connection, which is not gauge invariant, this quantity does not depend on the gauge choice [77]. The sum of WCCs is given by

$$\sum_\alpha \overline{x}_\alpha^S = \frac{1}{2\pi}\int_{BZ} A^S, \tag{73}$$

where $S = I, II$, due to time-reversal symmetry property. In a smoothly period adiabatic motion over an adiabatic time interval $\left[0, \frac{T}{2}\right]$, the Z_2 index can be calculated in the following way

$$Z_2 = \sum_\alpha \left[\overline{x}_\alpha^I\left(\frac{T}{2}\right) - \overline{x}_\alpha^{II}\left(\frac{T}{2}\right)\right] - \sum_\alpha \left[\overline{x}_\alpha^I(0) - \overline{x}_\alpha^{II}(0)\right]. \tag{74}$$

This invariant performs a fundamental in the classification of trivial and topological insulators, as will be discussed in detail in the following chapter.

Chapter 3

Topological systems in condensed matter

Topological phases of matter are among the most promising topics of condensed matter physics. Since the discover of the nontrivial phases in solids, different topological systems have been both theoretically predicted and experimentally observed. Due to their potential application in different areas, topological materials have attracted significant scientific interest in the last two decades. In this chapter, we first introduce the concept of topology and smooth deformations. Then we present the key properties and discuss the advances in three fundamental topological systems: topological insulators, Weyl semimetals and quantum anomalous Hall insulators. These phases will be investigated details in this work.

3.1 Topology

Topology is a field of mathematics that investigates geometric forms under adiabatic deformation and classifies them by an invariant. This branch is considered an extension of geometry. In this context, the topological classification can be represented by the genus invariant, denoted by g, which counts the number of holes in a surface. The sphere (Fig. 4(a)) represents a surface with $g = 0$, and the torus (Fig. 4(b)) a surface with $g = 1$. Different geometric forms with the same number of holes share the same invariant, since they belong to the same topological class. Interestingly, geometric forms in the same topological class can be transformed into one another through continuous deformations. Considering the torus in Fig 4(b), by applying smooth deformations, this geometry can be transformed into a teacup without changing its topological class. However, the transformation of the torus into a sphere would require performing, at some point, a non-smooth deformation, which is to perform a hole in its surface. Consequently, it is not possible to transform a torus ($g = 1$) into a sphere ($g = 0$) through smooth deformations.

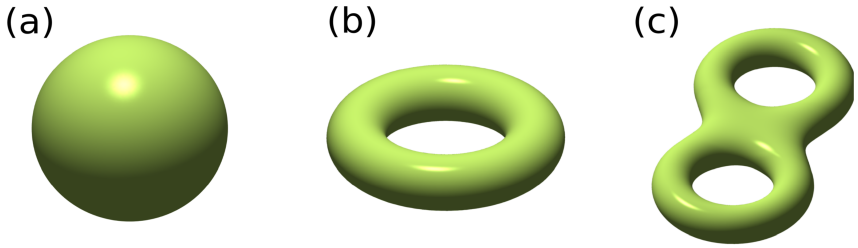

Figure 4 – Surfaces of a sphere (a), torus (b), and double torus (c), representing the geometric forms with genus $g = 0$, $g = 1$, and $g = 2$, respectively.

3.2 Topological insulators

The concept of topology was imported into condensed matter physics to classify different classes of band insulators, where one class cannot be adiabatically connected to another without significantly modifying their properties. Systems that show, in their electronic structure, an energy gap between the valence and conduction bands are classified as trivial and nontrivial (topological) insulators. Similarly to the genus and torus example, a trivial insulator cannot be smoothly transformed into a topological insulator without closing the band gap, leading to a different topological invariant [29, 78, 5]. In this case, the topological invariant is calculated by the Z_2 index, which is intrinsically related to the Berry phase and Wannier functions, as discussed in Section 2.5. While a trivial insulator shows $Z_2 = 0$, a topological insulator is characterized by $Z_2 = 1$.

One of the key signatures to identify a nontrivial phase in insulators is the bulk band behavior under inclusion of relativistic effects [4]. The topological phase transition is illustrated in Fig. 5. Without spin-orbit coupling (SOC), the bands behave as a trivial insulator with $Z_2 = 0$. Under a smooth increase of SOC effects, beyond a certain value, the band gap must close (critical point) and then reopen (Fig. 5(c)). With this reopening, the conduction band carries information from the valence band and vice versa, which leads to the nomenclature of an inverted band gap, as shown in Fig. 5(c). In bismuthene, as will be discussed in Chapter 4, the critical point occurs at 50% of SOC strength. In systems like graphene, the topological bands without SOC are already in the critical point configuration, and the inclusion of SOC lifts the degeneracy, leading to an inverted gap.

In a topological insulator, while the bulk exhibits a insulator band configuration, at the surface (in 3D system) or edge (in 2D system), metallic states connecting the valence to conduction bands are observed due to the bulk-boundary correspondence. It is important to note that these states arise not only with the vacuum interface, but also at interfaces with trivial materials. Interestingly, these metallic surface/edge states are spin-polarized and counterpropagate relative to one another. In the $+\boldsymbol{k}$ momentum direction, a spin up channel can be observed, while in the $-\boldsymbol{k}$ direction, there is a spin down edge channel, as illustrated in Fig 6. In this specific region of momentum space, the electrons behave as

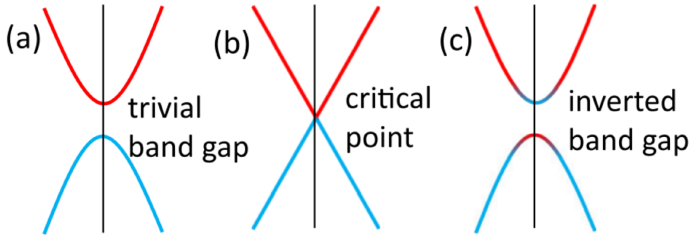

Figure 5 – Illustration of the band inversion process in a topological insulator. The blue and red color indicates the valence and conduction bands, respectively. As the SOC increases, the band gap start from a trivial behavior (a), achieve a critical point (b) and reopens with inverted character (c). Image from Ref. [4].

massless Dirac fermions, usually showing high-speed Fermi velocity on the order of 10^5 m/s [79, 80, 81], which enable valuable applications in high-speed electronics. Interestingly, as the topological surface/edge shows a spin-momentum locked, in the 3D systems, the spin-texture shows a helical behavior in a momentum-resolved dispersion, as shown in Fig 6(d). The Hamiltonian that describes these topological states and its helical behavior is given by

$$H = v_F \boldsymbol{k} \times \boldsymbol{\sigma}. \tag{75}$$

Here, $\boldsymbol{k}$ represents the momentum vector, $\boldsymbol{\sigma}$ the Pauli matrices, and v_F the Fermi velocity, we also denoted $\hbar = 1$. The nature of these spin-polarized boundary states lies in an intrinsic symmetry that plays a significant role in topological insulators, the time-reversal symmetry. Although more directly related to momentum reversal [82], which performs $\boldsymbol{p}|_{t=0} \rightarrow -\boldsymbol{p}|_{t=0}$, the time-reversal symmetry operator (Θ) is defined as

$$\Theta = e^{\frac{-i\pi S_y}{\hbar}} K = -i\sigma_y K. \tag{76}$$

Here, K denotes the conjugated complex operator, $\hbar$ the Planck's constant. The time-reversal operator leads to a moment inversion and also inverts the spin components in a half-integer spin system, in the form

$$\Theta^{-1} \boldsymbol{p} \Theta = -\boldsymbol{p}, \tag{77}$$

$$\Theta^{-1} S_z \Theta = -S_z, \tag{78}$$

and also

$$\Theta^{-1} H(\boldsymbol{k}) \Theta = H(-\boldsymbol{k}). \tag{79}$$

This Hamiltonian property imposes that the electronic band structure in a time-reversal symmetry protected system must appear in degenerate pairs. Such degeneracy forms what are called the Kramers pairs. This leads to the key property for topological insulators $E(\boldsymbol{k}, \uparrow) = E(-\boldsymbol{k}, \downarrow)$.

The SOC is intrinsically related to the atomic number. This relativistic effect induce topological phase in different materials composed by heavy elements, such as Sn, Pb

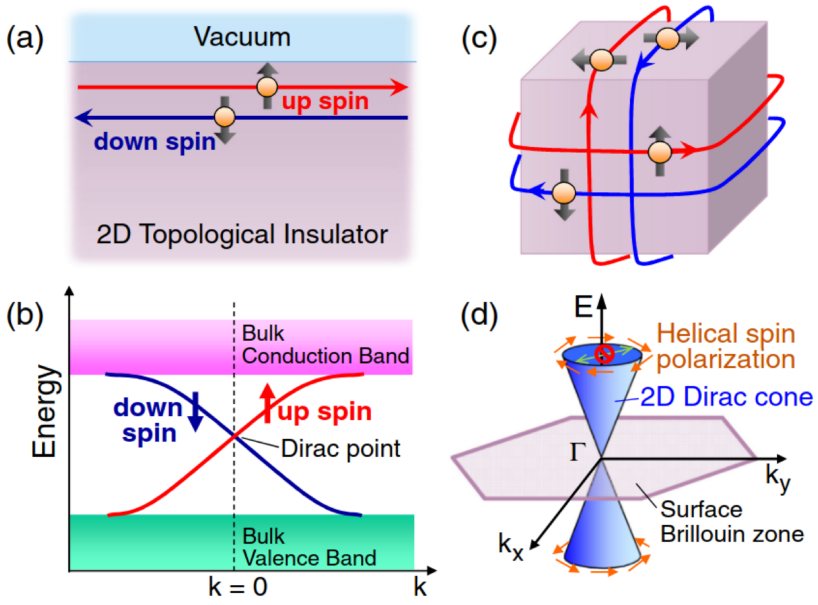

Figure 6 – Schematic representation of topological edge (a)-(b) and surface (c)-(d) states. Panels (a) and (c) show the real-space scenario, while (b) and (d) illustrates the corresponding momentum-space representation. Figure from Ref. [5].

and Te [41, 83]. In two-dimensional systems, the topological insulators, also known as quantum spin Hall insulators, were first predicted in graphene by Kane and Mele in 2005 [31]. Shortly after, in 2006, Bernevig, Hughes and Zhang proposed another quantum spin Hall system candidate, they reported the topological phase transition in CdTe confined HgTe quantum wells [84]. The experimental verification was given one year later, in 2007 [32]. In 3D topological insulators counterpart, the first experimental observation was reported in 2008. By means of angle resolved photoemission spectroscopy (ARPES), it was verified the topological surface states in $Bi_{0.9}Sb_{0.1}$ films [85]. Subsequently, this topological properties were verified in different pristine and doped 3D systems [86, 87].

A well-known 2D topological insulator, and the object of study in this part of this work, is the bismuth monolayer. This system was first experimentally grown in 2017 by Reis *et al.* [11], where a single bismuth monolayer was epitaxially deposited on a SiC substrate. Through ARPES images, a pair of topologically protected edge states where verified, showing a good agreement between experiments and DFT calculations. More recently, in 2021, a bismuth monolayer was grown on Ag(111), exhibiting a topological band gap of approximately 1 eV [12]. In both systems, due to substrate interaction, the bismuthene shows a planar configuration, with a band gap opening at the K point.

3.3 Weyl semimetals

In the study of topological systems, it is commonly reported that topological properties arise in materials with a band gap opened by SOC effects, as previously discussed. In this

way, a natural question arises: can band crossings also exhibit topological properties? The answer is yes, and the nature of this behavior lies in the Dirac equation. This equation provides a suitable way to combine quantum mechanics and special relativity, its solution can lead to different particles behaviors, giving rise to Dirac, Majorana and Weyl fermions.

In 1929, Hermann Weyl studied one particular solution of the Dirac equation, which is based on massless particles proposal [88]. The Weyl study led to a simpler case solution, where the fermions always arises in pairs with opposite chiralities. For a long time, neutrinos were thought to meet the criterion for Weyl fermions candidates, as also discussed in quantum mechanics textbooks [82, 89]. However, with the neutrino mass measurements, they do not fit as possible candidates, leaving a gap in this particles class [33]. Currently, there are no experimental reports of Weyl fermions in physics beyond solid state systems.

The Weyl Hamiltonian is given by

$$H = v_F \boldsymbol{k} \cdot \boldsymbol{\sigma}. \tag{80}$$

From the previous Hamiltonian, the Weyl fermion eigenenergies are given by $E = \pm v_F k$. The energy of a Weyl fermion shows a linear dispersion in the momentum space.

In the solid state physics context, a given system protected by both inversion and time-reversal symmetry has a band structure double degenerate in spin up and spin down, where $E(\boldsymbol{k}, \uparrow) = E(\boldsymbol{k}, \downarrow)$. Without SOC, a symmetry-protected system can shows fourfold degenerate Dirac crossings between the valence and conduction bands. When SOC is included, these band crossings can be affected or not, as illustrated in Fig. 7. The first possible scenario is the band opening (Fig. 7(a)), which is a key signature of topological insulators, as previously discussed. The second possibility is that the SOC does not affect the fourfold degenerate band crossing, resulting in a Dirac semimetal signature. A pair of Weyl points may arise from a Dirac semimetal by breaking either time-reversal or inversion symmetry, where a fourfold degenerated crossing slipts into pair of Weyl crossings (Fig. 7(b)). It is important to note that Weyl points can also arise in systems without Dirac semimetal behavior. In gapped systems, by breaking the inversion or time-reversal symmetry, the upper and lower bands can split and cross each other, leading to a topological phase transition [21].

Weyl fermions show a nonvanishing Berry curvature at the crossing point. Starting from the Weyl Hamiltonian (Eq. (80)), the Berry curvature is given by [90, 91]

$$\boldsymbol{\Omega} = \mp \frac{\boldsymbol{k}}{2k^3}. \tag{81}$$

Where $\boldsymbol{\Omega}$ denotes the Berry curvature. In this scenario, Weyl points can be understood as monopole chiral charges, where the positive and negative topological crossings act as a source and drain of Berry curvature, respectively. This form allows the visualization of the Berry curvature as field lines connecting Weyl points with opposite chiralities. The Weyl chirality is given by

$$\chi = \frac{1}{2\pi} \int_{FS} \boldsymbol{\Omega} \cdot d\boldsymbol{k}. \tag{82}$$

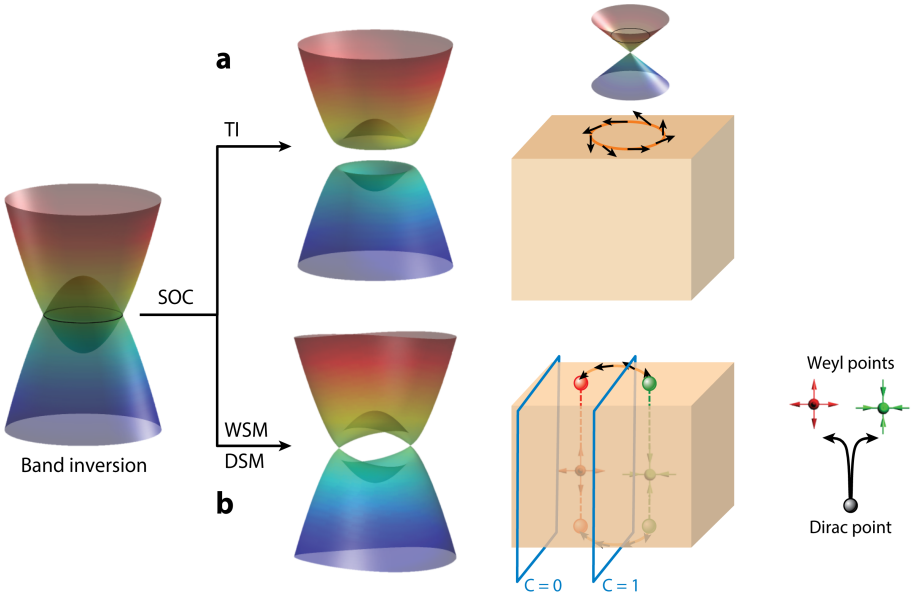

Figure 7 – Schematic illustration of an inverted band structure without SOC. The inclusion of SOC can open a band gap (a), characterizing a topological insulator phase, or when combined with a fundamental symmetry breaking, form a Weyl semimetal phase (b). In the topological insulator phase, the arrows represent the helical spin texture of the Dirac cone, while in the Weyl semimetal phase the arrows indicate the Fermi arcs. Adapted image from Ref. [6].

Here, *FS* represents the Fermi surface that encloses a Weyl point. Due to Nielsen-Ninomiya theorem [92], also known as fermion doubling theorem, the sum of the chiral charges in the Brillouin zone must be zero, satisfying the following equation

$$\sum_{j}^{BZ} \chi_j = 0. \tag{83}$$

This implies that Weyl points must arise in pairs with opposite chiralities in the Brillouin zone; consequently, a single Weyl point will not appear without its corresponding partner [77, 90]. In this way, symmetries play a crucial role in the Weyl semimetals study. Distinct symmetry conditions lead to different Weyl point behavior in the Brillouin zone, affecting both Berry curvature and chirality. For a noncentrosymmetric 3D system, protected by time-reversal symmetry, with a pair of Weyl points located in $\boldsymbol{k_0}$ and $-\boldsymbol{k_0}$, the Berry curvature and Weyl chiralities show the following properties

$$\boldsymbol{\Omega}(\boldsymbol{k}_0) = -\boldsymbol{\Omega}(-\boldsymbol{k}_0), \tag{84}$$

$$\chi(\boldsymbol{k}_0) = \chi(-\boldsymbol{k}_0). \tag{85}$$

In contrast, for an inversion-symmetric 3D system, but with the time-reversal symmetry broken, the properties changes as follows

$$\boldsymbol{\Omega}(\boldsymbol{k}_0) = \boldsymbol{\Omega}(-\boldsymbol{k}_0), \tag{86}$$

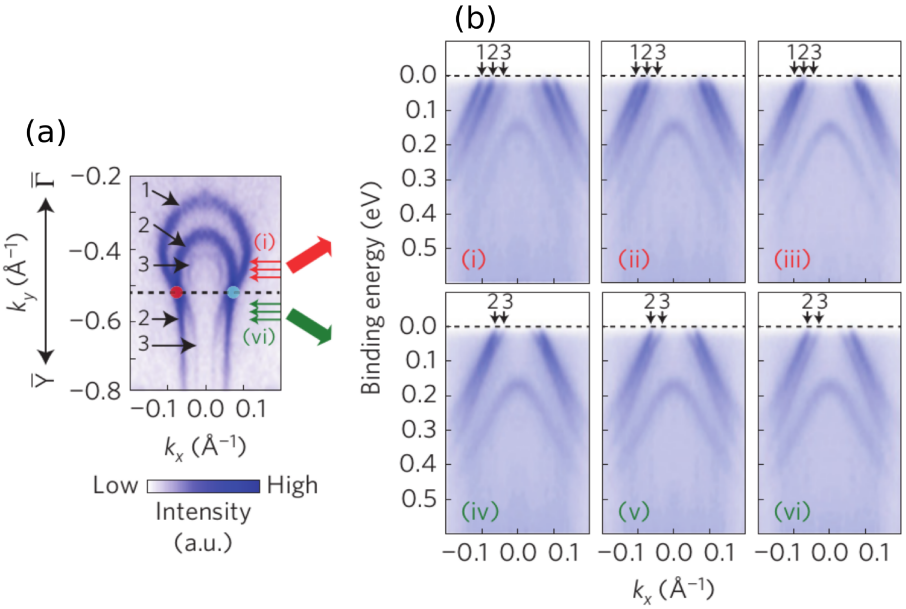

Figure 8 – Momentum-resolved (a) and energy-resolved (b) measurements of the Fermi arcs on the TaAs surface. The red and blue points indicate the Weyl nodes with opposite chiralities. Adapted image from Ref. [7].

$$\chi(\boldsymbol{k}_0) = -\chi(-\boldsymbol{k}_0). \tag{87}$$

It is important to note that these properties are restricted to 3D systems. In time-reversal symmetric systems the minimum number of Weyl points that may arise in Brillouin zone is four. In counterpart, for time-reversal symmetry broken systems, this minimal number of Weyl point is two [34, 91]. As will be discussed in Chapter 5, with the reduction in dimensionality, the inversion and time-reversal properties for Weyl points and Berry curvatures significantly change.

Similarly to other topological materials, Weyl semimetals show nontrivial surface (or edge) states due to the bulk-boundary correspondence. In this class, these topological states are called Fermi arcs. While in topological insulators the boundary states connect the valence to conduction bands, the Fermi arcs form open curves that connect the projected bulk Weyl points at the surface (or edge), as schematically shown in Fig 7(b). Through ARPES measurements, in a 3D system, Fermi arcs can be observed at two different perspectives, the first consists in a fixed energy value with k-resolved momentum, as shown in Fig 8(a), the second is in energy resolved per momentum band structure (Fig. 8(b)). Interestingly, in systems where the surface projects two Weyl points degenerated, for examples in a top surface projecting $+k_z$ and $-k_z$ Weyl points, the projected Fermi arcs will shown a double degenerated behavior.

The intrinsically noncentrosymmetric TaAs family (TaAs, NbP, TaP and NbAs) was the first family of Weyl semimetals theoretically predicted and experimentally observed [35, 93, 94, 95, 7, 96, 97]. Their prediction was in 2015 and, at the same year, the exper-

imental verification in TaAs and TaP occurred, marking a breakthrough in topological matter research. Subsequently, other materials were verified to show the Weyl semimetal phase, including transition metal dichalcogenides, such as $MoTe_2$ and WTe_2 [98, 99, 100, 101, 102, 103], and magnetic materials [104, 105, 106, 107].

Previously, it was believed that Weyl crossings were restricted only to 3D systems. However, it was verified that, under the protection of an crystal symmetry, Weyl semimetals can also arise in 2D systems [90]. The first predictions were reported in 2D magnetic materials [108, 109, 110, 111, 112, 113, 114, 115], followed by reports of quadratic Weyl crossings in both magnetic and non-magnetic systems [116, 117], and a linear Weyl crossing in a noncentrosymmetric system [118]. In 2024, the first experimental observation of Weyl semimetals in two-dimensional was reported [21], these topological crossings were found in bismuthene grown on a SnS substrate. A subsequent experimental identification of Weyl fermions in two dimensions was achieved in the $PtTe_{1.75}$ monolayer [119]. A well-detailed discussion on Weyl fermions in two-dimensional systems is presented in Chapter 5.

3.4 Quantum anomalous Hall insulators

The interplay between magnetic fields and electronic properties leads to remarkable physical effects in solid state physics. One of the most interesting discovers regarding the magnetism in materials is the connection between transversal conductivity and magnetic field intensity, first reported by Edwin H. Hall in 1879 [120]. This investigation demonstrates that in a metallic sample, when an electric current is applied parallel to the system while a perpendicular magnetic field is present, the electrons experience the Lorentz force. As a consequence, their trajectory is modified, leading to electron accumulation on one side and hole (positive charges) accumulation on the opposite side. This charge separation creates a potential difference between the opposite edges of the system, with is named as Hall voltage. Consequently, a transversal resistivity ρ_{xy} emerges, which is called Hall resistivity. This physical quantity is inversely proportional to the Hall conductivity σ_{xy}. Hall verified that this transversal conductivity is proportional to the applied magnetic field, which grows linearly with the external magnetic field.

With advances in experimental techniques, nearly 100 years later, Klaus von Klitzing verified that, under strong magnetic fields (close to 15 T) and low temperatures (4 K), the Hall conductivity becomes quantized in integer units of e^2/h, consequently the Hall resistivity is also quantized in h/e^2 integer values [121]. The remarkable precision of these measurements exhibits minimal experimental deviation for the quantized values [122]. These findings demonstrated the positive impact of the quantum Hall effect in the metrology [36]. Due to significance of the discovery of quantum Hall effect, Klaus von Klitzing received the Nobel Prize in Physics in 1985.

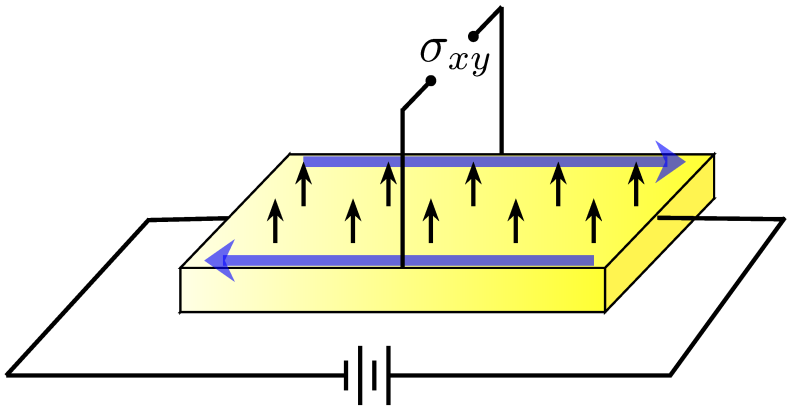

Figure 9 – Scheme of the quantum anomalous Hall effect. The blue arrows represent the dissipationless topological edge states, and the black arrows indicate the intrinsic magnetic moment of the material.

Magnetic systems also play a crucial role in the study of Hall effect and its derived effects. Shortly after the discovery of the Hall effect, Edwin Hall verified that, using a ferromagnetic sample, the Hall voltage increased 10 times compared to the nonmagnetic counterpart [123, 124]. This finding enhanced the discussion of the intrinsic magnetic role in the Hall effect. Interestingly, nonzero Hall conductivity can also arise in systems exposed to a potential difference and without any externally applied magnetic field, as schematically illustrated in Fig. 9. This effect is named as anomalous Hall effect, and, when the Hall conductivity shows quantized values, is named as quantum anomalous Hall (QAH) effect [36, 124, 72].

Quantum anomalous Hall insulators show similar properties to quantum spin Hall insulators. However, as these materials are magnetic, they intrinsically break the time-reversal symmetry. In these materials, the SOC strength also plays a crucial role in band inversion, resulting in a nonzero topological invariant. As a consequence, topological surface (or edge) states emerge due to bulk-boundary correspondence. These topological states connects the bulk bands with a gap opened by SOC. Unlike quantum spin Hall systems, where the boundary states counterpropates each other, these states propagates in one direction, as illustrated by the blue arrows in Fig 9. The number of topologically protected states is determined by the topological invariant, in this case, the Chern number

$$C = \frac{1}{2\pi}\int_{BZ} \boldsymbol{\Omega}(\boldsymbol{k}) d^2k. \tag{88}$$

Here, $\boldsymbol{\Omega}(\boldsymbol{k})$ is the Berry curvature as discussed in Section 2.4. Unlike the Z_2 index, where a topological insulator is characterized by $Z_2 = 1$, quantum anomalous Hall systems can exhibit different Chern numbers with values, including higher than 3 [125, 126], leading to a large number of boundary states propagating in one direction.

One of the key findings regarding topological properties in quantum anomalous Hall systems is the intrinsic connection between anomalous Hall conductivity and Berry phase

properties [124, 127, 75]. With the emergence of boundary states, the anomalous Hall conductivity shows a plateau peak at the band gap opening region in bulk. The Chern number will define the intensity value in integer units of e^2/h. The anomalous Hall conductivity is given by

$$\sigma_{xy} = C\frac{e^2}{h}. \tag{89}$$

It is important to note that contributions to σ_{xy} are not exclusively from Berry phase effects. Different effects can also influence the transversal conductivity, and potentially affect its quantized properties [72, 124].

The combination of topological boundary states with intrinsic magnetism makes quantum anomalous Hall systems promising candidates for practical applications, such as spintronic and memory storage technologies. The quantum anomalous Hall effect has been theoretically predicted in a large variety of materials, such as doped-systems [125, 128, 129], metal-organic frameworks [130, 131, 132] and in-plane magnetization systems [133]. More recently, in the context of valleytronics, different materials candidate have been proposed as quantum anomalous valley Hall insulators [134, 135].

In 2013, the first experimental observation of the QAH phase was reported by Chang *et al.* [38]. Using controlled Cr atoms doping, they verified the QAH effect in two well-know topological insulators, Bi_2Te_3 and Sb_2Te_3 films. In 2015, using the same topological insulators compounds, but with V atomic doping, it was verified the QAH phase in these materials [136]. This topological effect was observed in the intrinsically magnetic $MnBi_2Te_4$ flakes in 2020 [2]. This material show a different topological phases, such as magnetic topological insulator, quantum anomalous Hall effect and Weyl semimetal, which can be tuned by different magnetic alignment [137].

Chapter 4

RKKY interactions mediated by topological states in bismuthene

In this chapter, we investigate the effects on the electronic and topological properties of the bismuthene doped with magnetic atoms. It is well-known that magnetic effects can significantly affect the intrinsic properties of topological insulators, which can lead to a band gap opening in their edge/surface Dirac crossing, allowing electronic backscattering, consequently reducing their practical applications [29, 79, 4]. However, valuable findings can also arises in magnetic-doped topological insulators, such as the possibility of quantum anomalous Hall effect [36], long-range coupling between impurities due to topological effects [138, 139, 140], and spin filtering device applications [23]. Beyond this, magnetic properties may arise in topological insulators at different ways, such as due to dangling bonds [141] and doping effects [142, 143], which enhances the efforts in the investigation and control of magnetism in topological insulators [1].

4.1 Bismuth monolayer - Revision

The key insights into quantum spin Hall (QSH) insulators were given by Kane and Mele in 2005, who developed a model originally proposed for graphene [31]. However, the carbon SOC parameter exhibits a low intensity value, resulting in a extremely small band gap opening at the K-point, estimated as 42 μeV [144]. Although the topological phase in graphene is not easily experimentally accessible [4], the same crystal structure, composed of heavier atoms such as silicon, germanium, and thin, provides valuable findings into the context of topological materials [29, 4]. In this way, a theoretically predicted [145, 146] and experimentally synthesized [11, 12] QSH insulator is the bismuth monolayer. The bismuth monolayer, also known as bismuthene, has a crystal structure similar to graphene, but instead of C atoms, it is composed of a group-V element, the Bi atom. Figure 10 shows the bismuthene in the top (a) and side (b) views. Unlike graphene, which is planar,

[1] The results discussed in this chapter were published in Ref. [138].

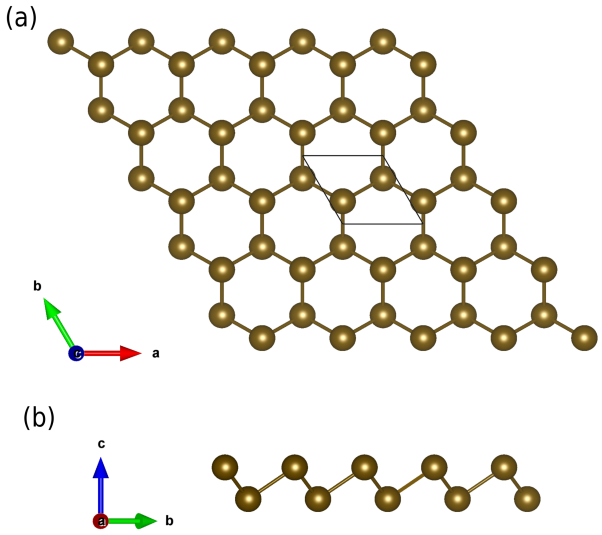

Figure 10 – Top (a) and side (b) view of the bismuthene crystal structure. The black line indicates the unit cell, which contains two atoms.

bismuthene shows a buckling height of 1.77 Å along the c direction. Its unit cell contains two atoms, and shows fully optimized lattice parameters as $a = b = 4.43$ Å, with a Bi-Bi bound length of 3.12 Å. To avoid interactions with its image periodicity, we have adopted $c = 20$ Å.

As we mentioned in Section 3.1, one signature for the quantum spin Hall effect is the band inversion with SOC inclusion. In bismuthene, the SOC strength, estimated as 0.43 eV [11], plays a crucial role in the band structure. Figure 11 shows the orbital-projected band structure for bismuthene under different percentages of SOC. Without SOC (Fig. 11(a)), the top of the valence band at Γ point is mainly composed by the sum of p_x and p_y orbitals, denoted here by p_{xy} (red symbols), in counterpart, the bottom of conduction band is dominated by the p_z orbitals (blue symbols). With the increase in SOC effects, around 50% of SOC (Fig. 11(c)), it can be noted a critical point, where the bands close the gap and then reopen with an inverted orbital character. With the band gap reopening due to SOC, at Γ point, the top of valence band is now mainly composed of p_z orbitals, while the bottom of the conduction band shows a p_{xy} orbitals, clearly indicating a band inversion phenomenon. The band gap with SOC effects shows a magnitude of 0.6 eV.

To confirm the topological nature of bismuthene, we performed a topological invariant calculation. Since this system is protected by spatial inversion symmetry, the Z_2 index can be determined from the parity of the occupied electronic states [147]. However, we have used the evolution of the Wannier charge center method [148, 149], discussed in Chapter 2. Our calculations show a $Z_2 = 1$ index for the SOC-included system, indicating its nontrivial character.

It is well-known that in a QSH system, while the bulk has a normal band gap, at the

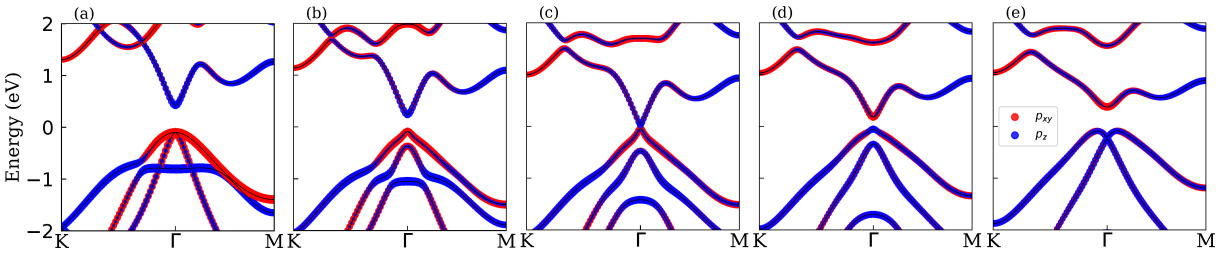

Figure 11 – Projected band structure for bismuthene without SOC (a) and under different percentages of SOC: 25% (b), 50% (c), 75% (d), and 100% (e). The blue and red circles correspond to the p_z and p_{xy} orbitals, respectively.

edges, electronic states connect the valence and conduction bands. Those edge electrons, in a given energy-momentum space region, behave as relativistic massless fermions. Interestingly, for each edge, two counterpropagating spin-polarized edge states can be observed as a consequence of time-reversal symmetry, where $E(+\boldsymbol{k},\uparrow) = E(-\boldsymbol{k},\downarrow)$. To investigate this bulk-boundary correspondence, we construct a sufficiently large bismuthene nanoribbon, where we perform the edge cut along the zigzag direction. The large width ensures that the spin channels on the left and right edges do not hybridize. These calculations were carried out using the tight-binding model based on Wannier functions extracted from DFT results, as described in Appendix A.

To construct and perform the nanoribbon calculations, is required to perform a rigid cut in the edge atomic bonds. These dangling bonds can significantly affect the electronic behavior of a QSH insulator at the interface with a trivial system (or the vacuum). In the bismuthene nanoribbon, without the edge ionic relaxation, a non-vanishing magnetism arises in these edge atoms due to unpaired electrons in p orbitals [150]. This local magnetic moment has an order of 0.29 μ_B, and, in ferromagnetic (FM) configuration, it lifts the degeneracy of the edge states. In this context, there is no connection between the valence and conduction bands via edge states. In the studies performed by Dev and Naumov [150, 151], it was found that, with the magnetism in the antiferromagnetic (AFM) phase, the connection with conduction band by the topological edge states is recovered. A useful way to reconstruct the edge, resulting in a vanishing magnetic moment, is by performing edge ionic relaxation. With the new edge atomic positions, the magnetism vanishes.

Figure 12(a) presents a projection of the right edge states from the bismuthene nanoribbon in a zigzag cut, shown in Fig. 12(d). Two counterpropagating edge states can be seen, they arises in $\overline{k_y} = 0$ point, crosses each other in $\overline{k_y} = \pi/a$ and connects the valence to conduction bands in $\overline{k_y} = 2\pi/a$ point. The Fermi velocity of this Dirac crossing is estimated as $v_F = 1.1 \times 10^5$ m/s. It is worth to note that these topological edge states are doubly degenerate in the entire energy dispersion due to contributions from the right and left edges, resulting in a fourfold degenerate crossing point. Although the projected edge states provide a suitable analysis from the topological behavior, in the context of time-

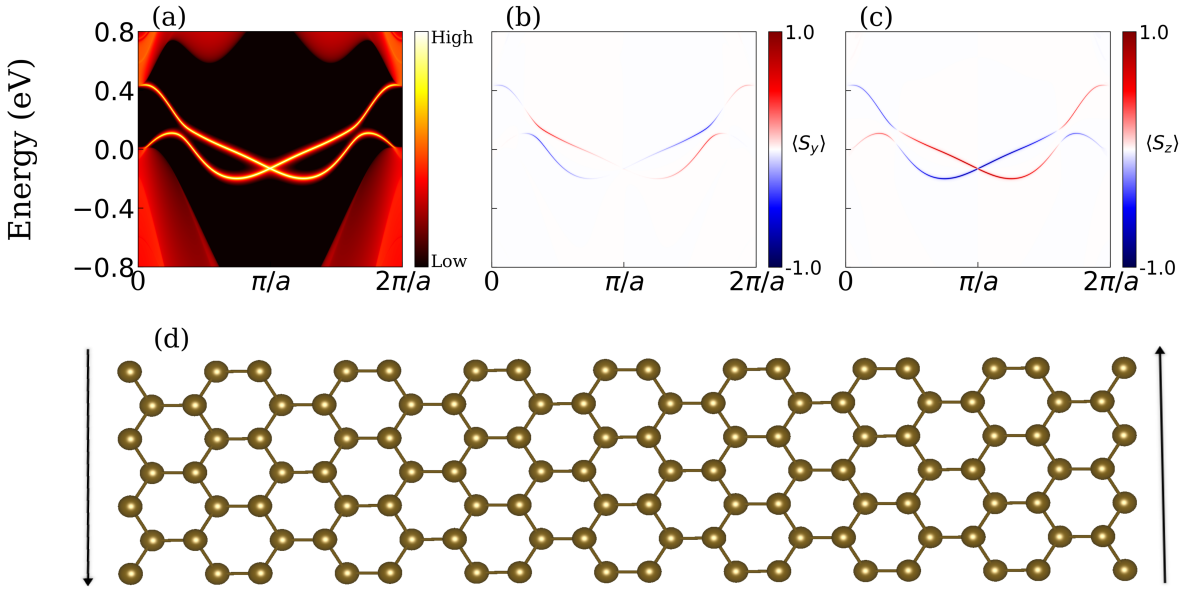

Figure 12 – (a) Bismuthene band structure without edge passivation. The contribution of the edge state is highlighted with the high intensity contribution in colormap, while the bulk shows a low intensity contribution. Spin texture colormap is shown in (b) for $\langle S_y \rangle$ component and (c) for $\langle S_z \rangle$ counterpart. The red (blue) color indicates spin up (spin down). The bismuthene nanoribbon in a zigzag cut illustrating figure is shown in (d), the arrows indicate the system periodicity.

reversal symmetry, we further investigated the spin texture $\langle \boldsymbol{S} \rangle$ of this system, where the spin polarization vector is given by

$$\langle S_{i,\alpha} \rangle = \frac{\hbar}{2} \langle \phi_i(\boldsymbol{k}) | \sigma_\alpha | \phi_i(\boldsymbol{k}) \rangle. \tag{90}$$

Here σ_α represents the Pauli matrices, α the x, y and z coordinates, and ϕ_i the wavefunctions of i-th electronic states. The spin vector is given by the sum of its component. As can be seen in Figs. 12(b) and 12(c), these edge states are mainly determined by the $\langle S_y \rangle$ and $\langle S_z \rangle$ components, resulting in a spin vector with the form $\langle \boldsymbol{S} \rangle = \langle S_y \rangle \hat{y} + \langle S_z \rangle \hat{z}$. In agreement with the TRS property, the energy relation $E(+\boldsymbol{k}, \uparrow) = E(-\boldsymbol{k}, \downarrow)$ is observed in the band dispersion. Due to symmetry property, at the other edge projection, the spin signal is inverted in comparison to the right edge, where it shows a positive signal, in the left edge is negative.

One useful way to avoid the dangling bond effects in nanoribbon calculations is to saturate the edge, where different types of atoms, usually nytrogen and hydrogen, are used to form chemical bonds with the edge ions, thereby avoiding missing bond effects [146, 150]. In this way, we passivate the dangling bonds at the zigzag edge with hydrogen atoms, as illustrated in Fig. 13. Our fully optimized ionic relaxation calculation shows a Bi-H bond length of 1.77 Å. In absence of dangling bounds, the topological edge states

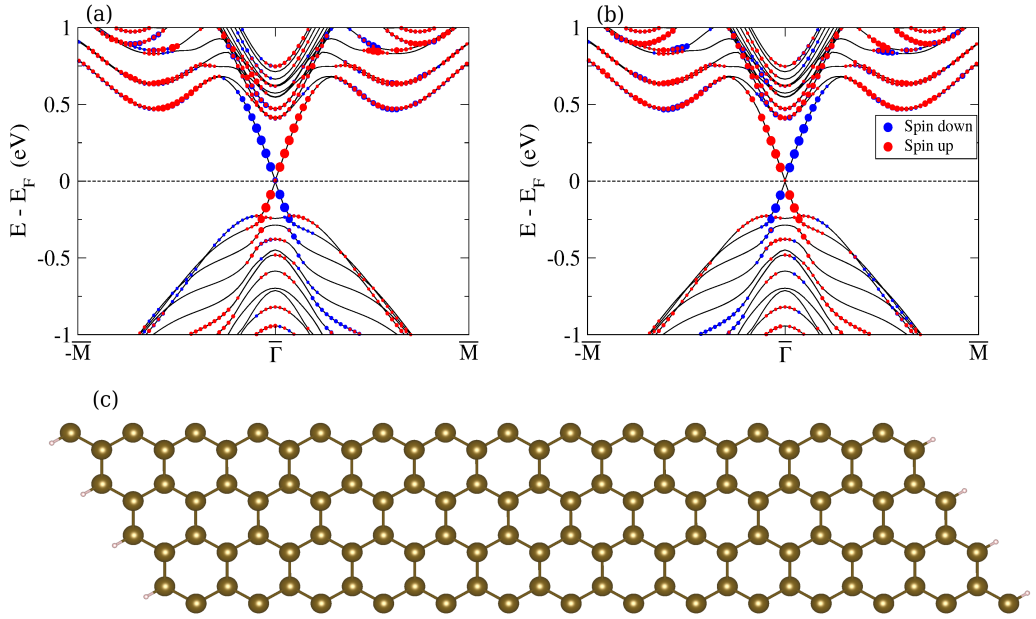

Figure 13 – Left (a) and right (b) edge projected spin texture $\langle S_z \rangle$ component onto band structure for the hydrogen edge passivated bismuthene (c). Here, the blue circles indicate spin down while the red color represents spin up.

has a significant change. The crossing point shifts to $\overline{k_y} = 0$ projection, and the Fermi velocity increases one order of magnitude (0.9×10^6 m/s). The spin-texture will also be affected by this electronic change, now the spin-contribution is uniquely dominated by the $\langle S_z \rangle$ contribution. Consequently, the total spin is given by $\langle \boldsymbol{S} \rangle = \langle S_z \rangle \hat{z}$.

4.2 Electronic properties of V-doped bismuthene

Using a large bismuthene unit cell with 50 atoms, repeated 5×5×1, we doped the bismuthene by perfoming a single atomic replacement. We substituted one Bi atom with a transition metal (TM) atom, vanadium. This single atomic replacement in the unit cell corresponds to a 2% of impurity concentration in this QSH system. The electronic configuration of the V atom is given by [Ar]$3d^3 4s^2$, where unpaired electrons in the d orbitals can be noted, resulting in a significant magnetic moment, enabling the study of magnetic effects in bismuthene. Due to atomic ratio difference between Bi and V atoms, we performed a nearest-neighbor relaxation calculation to obtain the optimized positions in this doped system. We observe a reduction in the buckling height for the Bi-V bond length (2.81 Å) in comparison with Bi-Bi bond-length (3.12 Å), as shown in Fig 14(a). These results are in good agreement with previous studies in the literature [152].

The V atom contributes with 3 μ_B out-of-plane (OP) magnetic moment per ion in the unit cell. To accurately describe the many-electron effects from the vanadium d-orbitals, we optimized the U_{eff} value using the linear response method [69]. Our calculations shows

that U_{eff} = 3.25 eV, which was used for all calculations in this work, unless otherwise mentioned. A direct comparison between the bismuthene band structure without and with V-doped can be seen in Figs. 14(b)-(d). Here, the magnetism induces a spin splitting in the band structure and introduces new energy levels inside the band gap. A strong hybridization can be observed between p and d orbitals from Bi and V atoms, respectively, shifting the Fermi level towards the valence band maximum. The Coulomb interaction separates the d-orbitals from the valence to the conduction band. To better visualize the effects of this correction on the electronic structure, we compare the results without (Fig. 14(c)) and with (Fig. 14(d)) U_{eff}. Without U_{eff}, a state mainly dominated by d orbitals emerges with minimum energy value is close to 0.18 eV at the Γ point. Additionally, an acceptor state is observed above the Fermi energy. This acceptor state also exhibit a small contribution from d states, resulting in a band gap with the upper state around 0.13 eV. With the inclusion of U_{eff} (Fig. 14(d)), the state with previous minimum value of 0.18 eV now shifts to above 0.3 eV, resulting in a direct band gap of 0.33 eV at the Γ point. One important finding is that, while without the Coulomb correction the acceptor state is partially flat around the Γ point, the introduction of the correction affects this band, which exhibits a nearly free electron behavior at Γ, similarly to pristine in Fig. 14(b).

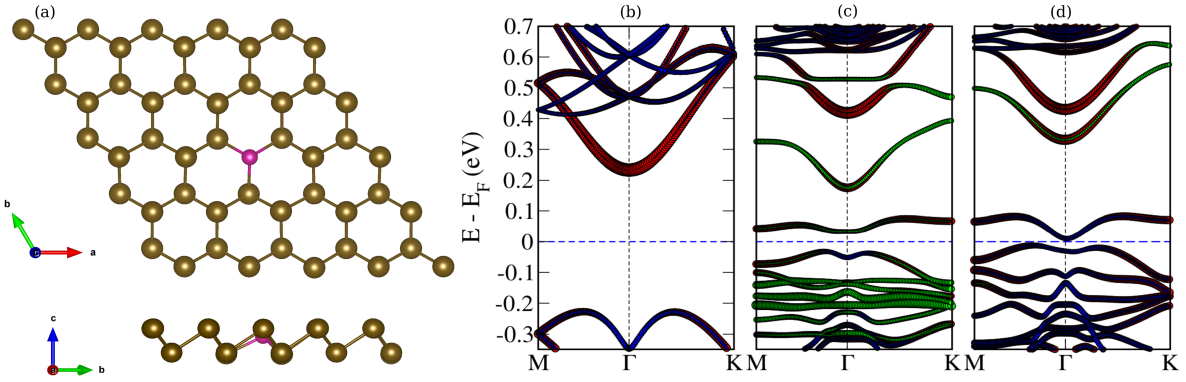

Figure 14 – Bismuthene doped with one V atom at the top and side view in (a). Projected band structure for pristine Bi monolayer (b), vanadium doped Bi system without (c) and with (d) U_{eff} correction. The red (blue) circles represent the contribution of p_{xy} (p_z) orbitals and the green circles represent the d-orbitals from V atoms.

One of the key findings of this work is the robustness of the topological invariant against the introduced impurities. Bismuthene shows a Z_2 equal to 1, even with the introduction of the impurities in concentrations up to 5%. However, a topological band behavior in the TM-doped system does not arises below the Fermi level, as in the pristine counterpart. The topological origin in this system lies in the new state with a nearly free electron behavior at the Γ point, similar to the pristine case, but located above Fermi energy. In higher doping concentrations, although the topological band gap is

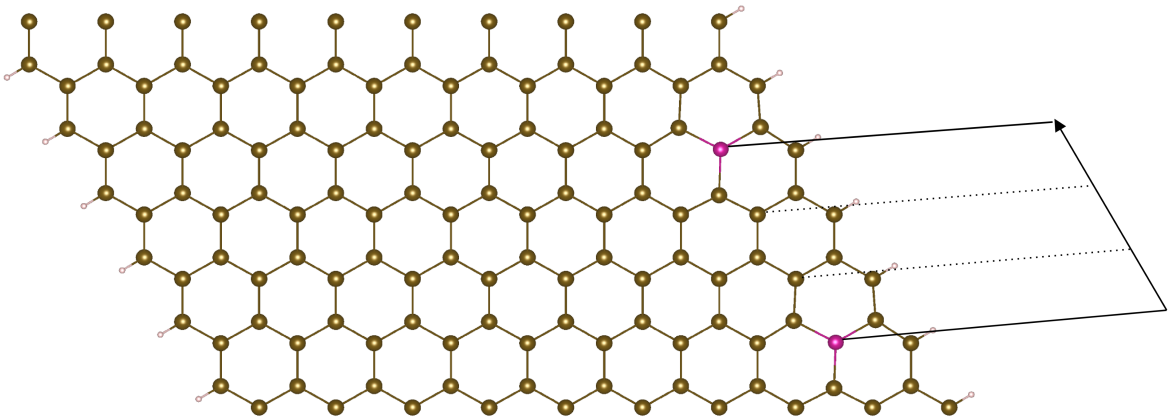

Figure 15 – Bismuthene nanoribbon with vanadium atoms (magenta circles) near the edge. The dashed lines indicate the possible first and second point defect substitution. At the edge, the white atoms represents the hydrogen atoms.

still observed, its magnitude is lower than in the case studied here. This reduced bulk gap may hinder the observation of topological edge states when performing a nanoribbon calculation to investigate the bulk-boundary correspondence.

4.3 Magnetic interactions in bulk

Since magnetism was induced in bismuthene by V atomic substitution, we can explore its magnetic properties and resultant effects, such as magnetic coupling between the ions and an increase in overlap orbital. As previously mentioned, the V atom contributes with a 3 μ_B magnetic moment, with its easy axis oriented OP. Consequently, due to periodic boundary conditions, the magnetic coupling with the impurity in the neighboring cell is ferromagnetic OP. However, to determinate the bulk ground magnetic phase (GMP), we increase the number of impurities in a enlarged unit cell. This allows us to set impurities in AFM and FM configurations. The GMP is determined by analyzing the total energy variation

$$\Delta E_T = E_T^{FM} - E_T^{AFM}. \tag{91}$$

Here, E_T^{AFM} (E_T^{FM}) denotes the total energy of the system with the impurities aligned in the AFM (FM) configuration. If the total energy variation is negative (positive), the FM (AFM) phase has lower energy, indicating this phase as GMP. We calculated the coupling between magnetic impurities as a function of their separation distance. As shown in Fig. 15, these deffects were simulated in a line arrangement. The inter-V distances corresponds to integer multiples of the lattice parameter. We conducted the calculations for separations up to 7 lattice parameters, corresponding to approximately 32 Å. As shown in Fig 16(a), the bulk bismuthene supports the FM phase for the shortest inter-V distances.

For larger separations (three lattice parameters), the exchange coupling decays to zero, indicating that the impurities become decoupled. This sugests that direct exchange interactions, such as overlap orbital, dominate in bulk. However, residual magnetic interations also emerges around 15 Å, suggesting an indirect magnetism contribution, where it may be mediated by the impurity state close to the Fermi level.

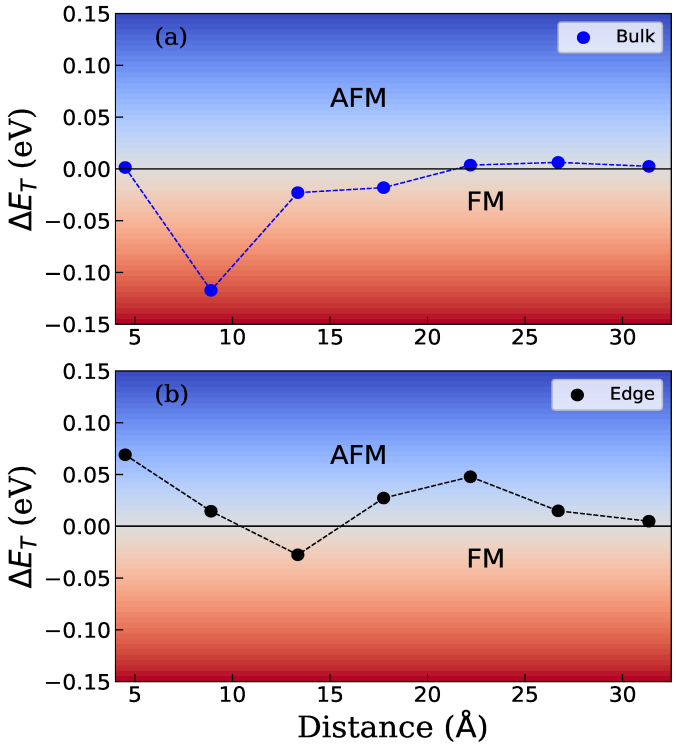

Figure 16 – Magnetic coupling (total energy difference) as a function of the inter-impurity distance when the V-atoms are in bulk (a) and at the edge (b) of the bismuthene.

4.4 Magnetic interactions via topological edge states

To investigate the role and effects of topological edge states in magnetic coupling between the V impurities, we have constructed a bismuthene nanoribbon with a zigzag edge, saturated with hydrogen atoms. We added the impurities at the second atomic row from the edge, as shown in Fig. 15. This allows us to study the effects of topologically protected spin-polarized massless fermions on the magnetic coupling between the impurities. Upon creating the edge in the system, interesting effects arise in this system. Figure 16(b) shows the total energy variation (Eq. (91)) for the impurities near the edge. Notably, when the topological edge state is present, the impurity interacts with the edge state, leading to a strong impurity coupling that depends on the TM separation. For a comparison, while the bulk system shows a near zero magnetic interaction at 19 Å, the edge configuration shows a high coupling value for the impurities, with an oscillatory increase that reaches

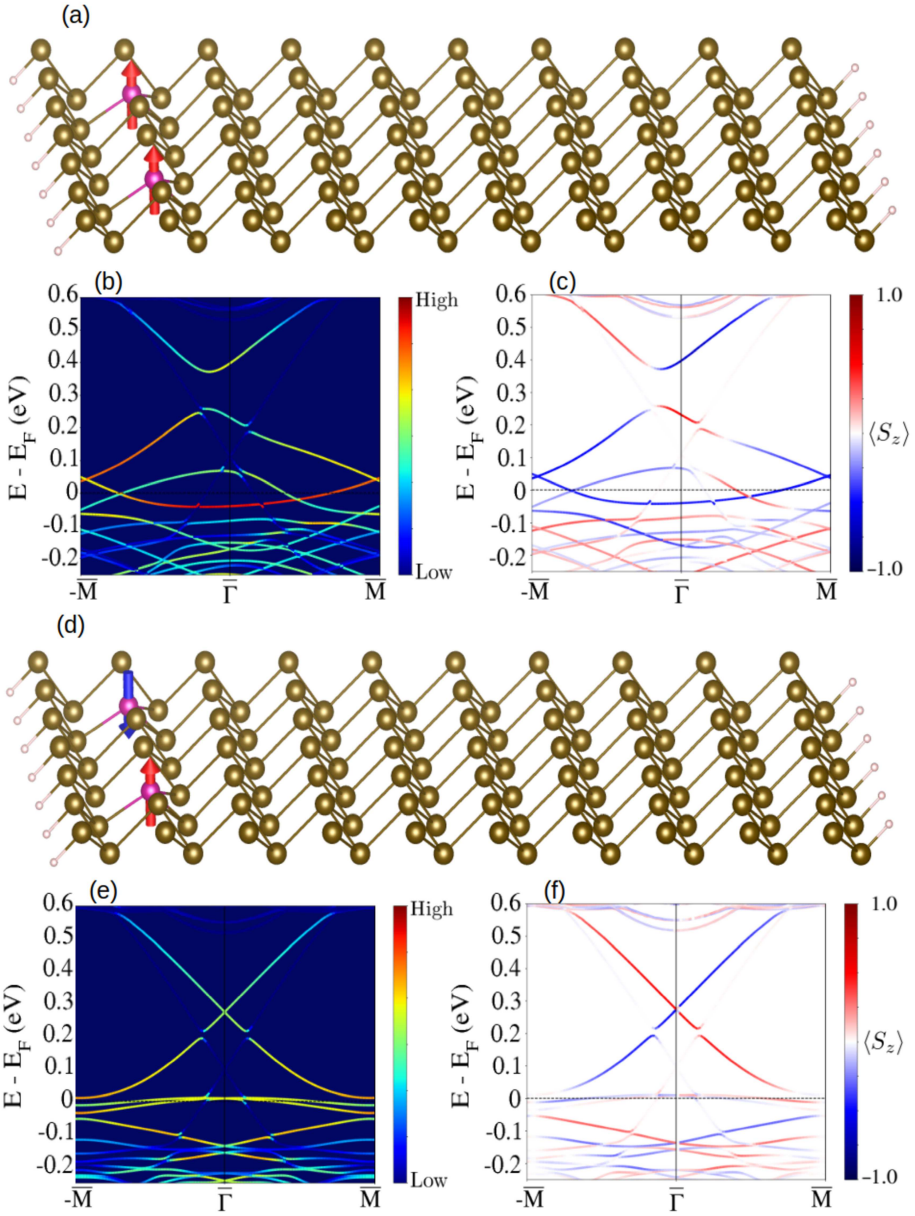

Figure 17 – Bismuthene structure with vanadium impurities near the edge is shown in (a), the arrows indicate the magnetic orientation for this system. In (b) is shown the orbital contribution of the doped edge atoms to the band structure and (c) the spin component $\langle S_z \rangle$ contribution. For the antiferromagnetic orientation of V atoms (d), the same is shown in (e) and (f).

a local maximum peak. Unlike in bulk configuration, the AFM in the edge configuration represents the GMP for nearly all the inter-impurities distances. Interestingly, for inter-V distances between 2 and 3 lattice parameters (approximately 9.8 and 14.5 Å), a transition in the GMP from AFM to FM is observed. With further increase, another phase transition is observed and the AFM configuration returns as GMP. This oscillation in GMP as function of inter-impurity distances is one of the signatures of Ruderman-Kittel-Kasuya-Yosida (RKKY) interactions, which are predicted to occur in both 2D and 3D systems [139, 153, 154]. The magnitude of these oscillations in both bulk and edge configurations

is consistent with studies with Fe-doped Bi_2Se_3, a well-known 3D topological insulator [140]. In the next section of this work, we will discuss these results from the perspective of an effective Hamiltonian.

In the following part of this section, we investigate the effects of magnetic interactions on the electronic band structure. For this analysis, we use the doped system with an inter-impurity distance of 3 lattice parameters. We performed calculations for defects in both in FM and AFM alignment, as can be seen in Figs 17(a) and 17(d), respectively. With the impurities in the FM configuration, the time-reversal symmetry is broken, lifting the Kramers degeneracy and enabling backscattering of electrons in the topological channels. Figure 17(b) shows the projected band structure of atoms from the left edge cut. The band gap magnitude is approximately 0.1 eV, and although backscattering occurs, the spin texture of these edge states remains OP, with $\langle S_z \rangle = \pm 1$ (Fig. 17(c)). On the other hand, when the impurities are in the AFM phase (Fig. 17(d)), the preservation of global time-reversal symmetry allows the recover of spin-polarized massless fermions channels that cross each other, with $E(+\boldsymbol{k}, \uparrow) = E(-\boldsymbol{k}, \downarrow)$. Notably, the AFM phase is the GMP for most inter-V distances, which leads us to conclude that the recovery of topological Dirac cone remains intact. It is important to mention that, in the topological edge states region, the V atoms contribute only with d_{xz} orbitals. The other orbitals from V remain at lower energy levels in the band dispersion. The robustness of this Dirac crossing is also observed in Cr-doped bismuthene with AFM alignment at the edge [155], supporting our findings. One interesting behavior in the AFM band structure is the parabolic curvature near the Fermi energy at $\overline{M}$ point, but linear at $\overline{\Gamma}$, indicating a competition between linear and quadratic $\mathbf{k}$ terms in the energy dispersion, similarly as reported in Rashba effect [156]. This energy dispersion indicates that the topological edge states have both massless and massive contributions at different points in momentum space. This finding provides valuable insights for building an effective model, as we will discuss latter. We performed the calculations without SOC, simulating a trivial insulator with the same edge. The obtained results were close to the bulk calculations, highlighting the importance of topology in this long-range coupling regime.

4.5 Effective Hamiltonian

To further validate the *ab initio* conclusions and provide a detailed analysis of the RKKY interactions between two magnetic impurities mediated by topological states, we derive an effective Hamiltonian that has the form of the RKKY Hamiltonian. To build this model, we consider a Hamiltonian H_0 that takes into account the relativistic massless fermions behavior with a linear energy dispersion, which corresponds to the dispersion of a pristine bismuthene nanoribbon, as shown in Fig. 13. Two magnetic impurities that are not directly coupled to each other can interact through indirect exchange. This interaction

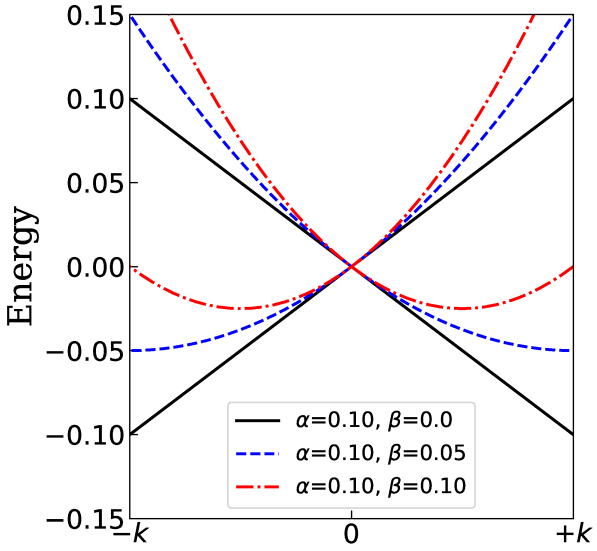

Figure 18 – Energy dispersion E(k) for different β parameters. The solid, dashed, and dash-dotted lines correspond to different values of β, as indicated in the legend box. Here, $E_+(k)$ and $E_-(k)$ are plotted in the same color.

can occur due to the electronic motion along the boundary of a system, or through a "sea" of conduction electrons [157]. To take into account the ribbon behavior, We build the wire Hamiltonian, which has the form

$$H_0 = \sum_{k,s,s'} (\beta k^2 \delta_{ss'} - \alpha k \sigma^z_{ss'}) c^\dagger_{ks} c_{ks'}. \tag{92}$$

Here $c^\dagger_{ks}$ (c_{ks}) denotes the creation (annihilation) operator of an electron with spin s in a low-energy band. Based on DFT results, we verified that the linear dispersion shows a slope, which reduces the Fermi velocity. This slope is denoted by the α parameter. The small curvature of the band near the Fermi level, represented by β, is one of the signatures of the competition between the linear and quadratic dispersion. This behavior is similar to that observed in Rashba effect [156]. Figure 18 shows the energy dispersion for different values of β compared to α. As the β parameter increases, a parabolic curvature near $\pm k$ becomes evident.

As we previously mentioned, the magnetic impurities $\boldsymbol{S}_1$ and $\boldsymbol{S}_2$ do not couple to each other directly. However, those magnetic impurities have a coupling with the ribbon $\boldsymbol{s}_i$ electrons, which mediates the indirect coupling. The interaction between the impurities and ribbon electrons is given by the Heisenberg model [157], which has the form of

$$H_i = 2J \sum_{i=1}^{2} \boldsymbol{S}_i \boldsymbol{s}_i, \tag{93}$$

where J is the coupling parameter between the impurity and the ribbon electron. The factor 2 is introduced for convenience [158]. Using the spin components property [82], we

rewrite the Hamiltonian (93) as

$$H_i = 2J\sum_{i=1}^{2}\left\{S_i^z s_i^z + \frac{1}{2}(S_i^- s_i^+ + S_i^+ s_i^-)\right\}. \tag{94}$$

The ribbon electron spins s_i can be expressed in terms of $c_{ks}^\dagger$ and c_{ks} operators using the following expressions

$$s_i^z = \frac{1}{2}(c_{i\uparrow}^\dagger c_{i\uparrow} - c_{i\downarrow}^\dagger c_{i\downarrow}), \tag{95}$$

$$s_i^+ = (c_{i\uparrow}^\dagger c_{i\downarrow}), \tag{96}$$

$$s_i^- = (c_{i\downarrow}^\dagger c_{i\uparrow}). \tag{97}$$

Here atomic units were used, with $\hbar = 1$. To rewrite the Hamiltonian from Eq. (94) in terms of creation and annihilation operators, we use the Eqs. (95), (96) and (97), resulting in

$$H_i = J\sum_{i=1}^{2}\left\{S_i^z(c_{i\uparrow}^\dagger c_{i\uparrow} - c_{i\downarrow}^\dagger c_{i\downarrow}) + S_i^-(c_{i\uparrow}^\dagger c_{i\downarrow}) + S_i^+(c_{i\downarrow}^\dagger c_{i\uparrow})\right\}. \tag{98}$$

In this way, it is convenient to obtain the Hamiltonian from Eq. (98) in momentum space. To perform this step, we apply the spatial Fourier transform in the operators $c_{ks}^\dagger$ and c_{ks}, which is given by

$$c_{i,s} = \frac{1}{\sqrt{N}}\sum_k e^{+ikx_i} c_{ks}, \tag{99}$$

$$c_{i,s}^\dagger = \frac{1}{\sqrt{N}}\sum_k e^{-ikx_i} c_{ks}^\dagger. \tag{100}$$

Applying the spatial Fourier transformation (Eqs. (99) and (100)) to the Hamiltonian in Eq. (98), we obtain the following Kondo-like Hamiltonian [157, 159, 160] which describes coupling between $\boldsymbol{S}_1$ and $\boldsymbol{S}_2$ with the edge electrons

$$H_i = \frac{J}{N}\sum_{k,k'} e^{-i(k-k')x_i}[S_i^z\left(c_{k'\uparrow}^\dagger c_{k\uparrow} - c_{k'\downarrow}^\dagger c_{k\downarrow}\right) + S_i^+ c_{k'\downarrow}^\dagger c_{k\uparrow} + S_i^- c_{k'\uparrow}^\dagger c_{k\downarrow}]. \tag{101}$$

In this context, x_i represents the coordinates of the impurities along the edge of the nanoribbon system, which we assume to be in x-orientation. Also, S_i^α, where $\alpha = x, y, z$ denotes the α-component of the impurity i spin operator and $S_i^\pm = \left(S_i^x \pm iS_i^y\right)/2$. The full Hamiltonian is given by the sum of the Hamiltonians from the nanoribbon (Eq. (92)) and the Kondo-like Hamiltonian (Eq. (101)), resulting in

$$H = H_0 + H_1 + H_2. \tag{102}$$

The effective Hamiltonian that describes the coupling between the magnetic impurities mediated by the ribbon edge electrons was obtained by means of second order perturbation theory, as proposed in Ref. [159]. In this method, the degrees of freedom of the itinerant

electrons are taken into account. Once that H_0 has already expressed in σ^z basis, the second-order perturbation theory can be applied to the H_1 and H_2 Hamiltonians

$$H_{eff} = \sum_{k,s}^{occ} \sum_{k',s'}^{emp} \frac{\langle k,s|H_1+H_2|k',s'\rangle\langle k',s'|H_1+H_2|k,s\rangle}{E_{ks}-E_{k's'}}. \tag{103}$$

By solving the previous Hamiltonian, we obtain an effective Hamiltonian describing the indirect coupling between the impurities

$$\tilde{H} = I_{\parallel} S_1^z S_2^z + I_{\perp} S_1^+ S_2^- + I_{\perp}^* S_2^+ S_1^-. \tag{104}$$

Which has the form of an anisotropic RKKY-like Hamiltonian. In this notation, $I_{\parallel}$ and $I_{\perp}$ are defined as $I_{\parallel} = 2\mathrm{Re}\left(I_{++} + I_{--}\right)$ and $I_{\perp} = \left(I_{-+} + I_{+-}^*\right)$, respectively. The I terms are given by

$$I_{\delta\nu} = \frac{J^2}{4\pi^2} \int_{-k_\delta}^{k_\delta} dk \int_{|k'|>k_\delta} dk' \frac{e^{i(k-k')x}}{\beta(k^2-k'^2)+\delta\alpha(k-\delta\nu k')}. \tag{105}$$

Here, we denote $\delta, \nu \in \{+,-\}$, $k_\delta = k_F + \delta k_\alpha$, $k_\alpha = \alpha/2\beta$. Also, $x = x_2 - x_1$ is the inter-impurities distance, which $x_2 > x_1$. We perform a change of variables, with $k = qk_F$ and $q' = k'/k_F$, then we can provide a suitable form of Eq. (105) as

$$I_{\delta\nu} = I_0 \int_{-q_\delta}^{q_\delta} dq \int_{|q'|>q_\delta} dq' \frac{e^{i(q-q')k_F x}}{(q^2-q'^2)+\delta\tilde{a}(q-\delta\nu q')}. \tag{106}$$

Where we use the following relations: $I_0 = J^2/4\pi^2\beta$, $a = 2k_\alpha/k_F = \alpha/\beta k_F$, and $q_\delta = 1 + \delta k_\alpha/k_F = 1 + \delta\tilde{a}/2$.

To solve the integral expression shown in Eq. (106), we performed numerical calculations. We use the effective model combined with the DFT results obtained in Section 4.4. We fixed parameter k_α as $k_\alpha = 0.05k_F$, which results in $\tilde{a} = 0.1$. Although we solved this integral by means of numerical calculations, in Appendix A of Ref. [159], the authors provided an analytical expression for this integral solution.

In the Section 4.2, we have shown that the V-impurities provide a OP magnetization, oriented along the z-direction. For all inter-impurities distances, the magnetic phase remains aligned in z axis, which results in an indirect coupling mediated only by the $I_{\parallel}$ terms from Hamiltonian described in Eq. (104).

Figure 19 shows a comparison between the total energy variation ΔE_T (black circles), obtained from DFT calculations in Section 4.4, and the $I_{\parallel}$ term, calculated numerically solving the effective model. Both quantities shows the same unit and are plotted as a function of V-V distance. As shown in the inset, the effective model provides results for any value of the inter-impurities distance x. In the DFT counterpart, the atomic positions are restricted by the crystal structure of the edge. The DFT results and effective model shows a good agreement. For short inter-impurity distances, there is a small shift in purple triangles compared to black circles. This small deviation may result from direct exchange interactions, which arise from the overlap orbital of the magnetic impurities. At

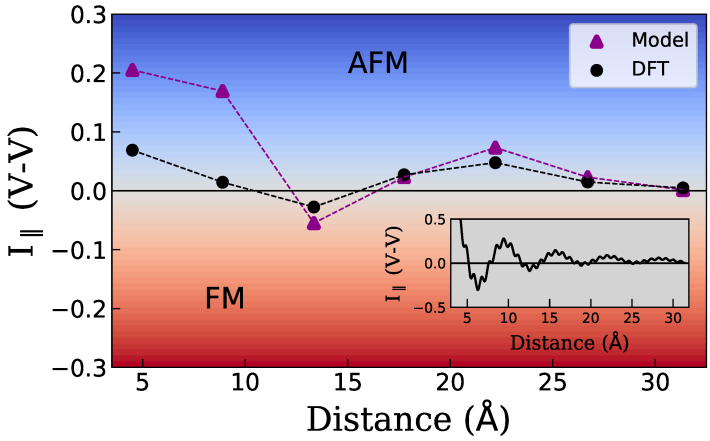

Figure 19 – Direct comparison between effective model results (purple triangles) at the lattice parameter distance points and DFT counterpart (black circles). The inset shows the continuous curve for the effective model.

large distances, the overlap orbital vanishing, resulting in a excellent agreement between the DFT and effective model. These results indicate that a RKKY-type of interaction arises from and it is mediated by the topological states of the bismuthene.

Chapter 5

Two-dimensional Weyl semimetals

Weyl semimetals are one of the last topological states of condensed matter physics that is theoretically predicted and experimentally observed. During a notable period, it was believed that this topological phase of materials would restricted only to three-dimensional systems, once that, with the dimensional reduction, the reduction in Weyl equation would make those crossings unstable against perturbations. However, it has been shown that, in the presence of an additional crystal symmetry, Weyl fermions can emerge in 2D systems. The role of the additional symmetry is to protect the Weyl point against instabilities. Similarly to 3D systems, for the emergence of Weyl semimetals in the 2D context it is also required to break one of the fundamentals symmetries: time-reversal or inversion. This chapter introduces the intrinsically noncentrosymmetric two-dimensional porous strutures, their electronic and topological properties, the Weyl semimetal case, as well as the Weyl equation in 2D [1].

5.1 Structural and electronic properties

The 2D porous structures studied in this chapter have atoms forming a hexagon connected to a square of atoms, arranged in such a way that a large ring can be observed, as shown in Fig. 20. In the case of carbon atomic composition, this porous structure is named graphenylene [161, 162], a widely studied material that has also been experimentally synthesized [163]. Here, we study the porous structure with two different atomic configurations. In the first distribution, blue and magenta spheres represent Si and Ge atoms, respectively. The second arrangement contains only Ge atoms. Unlike graphenylene, which is protected by inversion symmetry due to its planar configuration, both systems studied here present a small buckling height, 0.62 Å and 0.72 Å for SiGe and Ge, respectively. This intrinsic elevation along the c direction breaks the inversion symmetry, classifying both structures as noncentrosymmetric crystals. Their dynamical and thermal stabilities were confirmed through phonon and *ab initio* molecular dynamics

[1] The results discussed in this chapter were published in Ref. [118].

simulations in [164]. The SiGe and Ge porous structure crystallizes in P_{622} and P_6, or D_6^1 and C_6^1, space groups respectively, with fully converged lattice parameter $a = b = 10.92$ Å for SiGe and $a = b = 11.17$ Å. In both systems, the pore diameter is estimated to be around 9 Å, approximately 3 Å larger than the graphenylene counterpart [163].

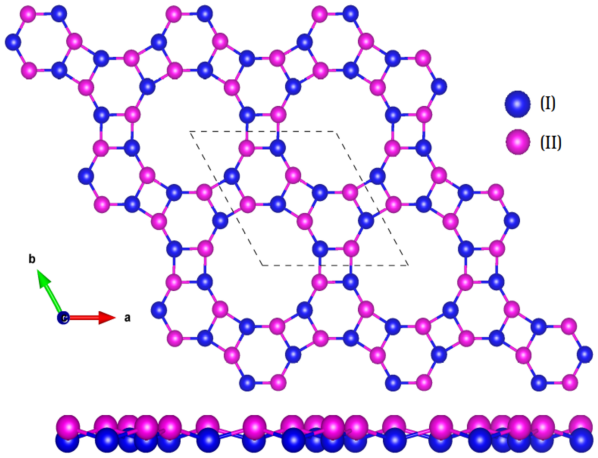

Figure 20 – Porous structure at the top (upper figure) and side (lower figure) views. Here, the dashed line represents the unit cell, which is composed by 12 atoms. The blue (I) and magenta (II) atoms was studied in both Ge and Si (I)/Ge (II) atomic distribution, respectively.

With the inclusion of SOC, the electronic band structure shows a semiconductor behavior for both systems, as shown in Figs. 21(a-1)-(a-2) and 21(c-1)-(c-2). The calculated band gaps between the top of the valence and the bottom of conduction bands are 4.0 meV for the SiGe configuration and 6.2 meV for the Ge counterpart. In the SiGe system, a smaller band gap opening is observed due to the SOC low parameter of Si compared to Ge ($\lambda_{Si} = 3.9$ meV and $\lambda_{Ge} = 43$ meV [80]). It is worth to note that the porous structure composed only with Si atoms exhibits a metallic behavior and does not show a sufficiently large band splitting upon the inclusion of SOC. Without SOC, in the full energy dispersion, the bands are doubly degenerate in spin up and spin down. Below the Fermi level, around -0.6 eV, interesting fourfold degenerate band crossings are noted, as highlighted in Figures 21(b-2) and 21(d-2). With the inclusion of SOC, two bands lift their degeneracy, while two others cross each other at two different points in the Brillouin zone (Figures 21(a-3) and 21(c-3)), producing a band crossing characteristic of Weyl semimetals [33, 6, 35].

5.2 Topological properties

In the band structure of porous Ge, a band gap opening is observed with the inclusion of fully relativistic effects, as shown in Fig. 21, where Fig. 21(d-1) corresponds to the band structure without SOC and Fig. 21(c-2) to the band structure with SOC. In SiGe,

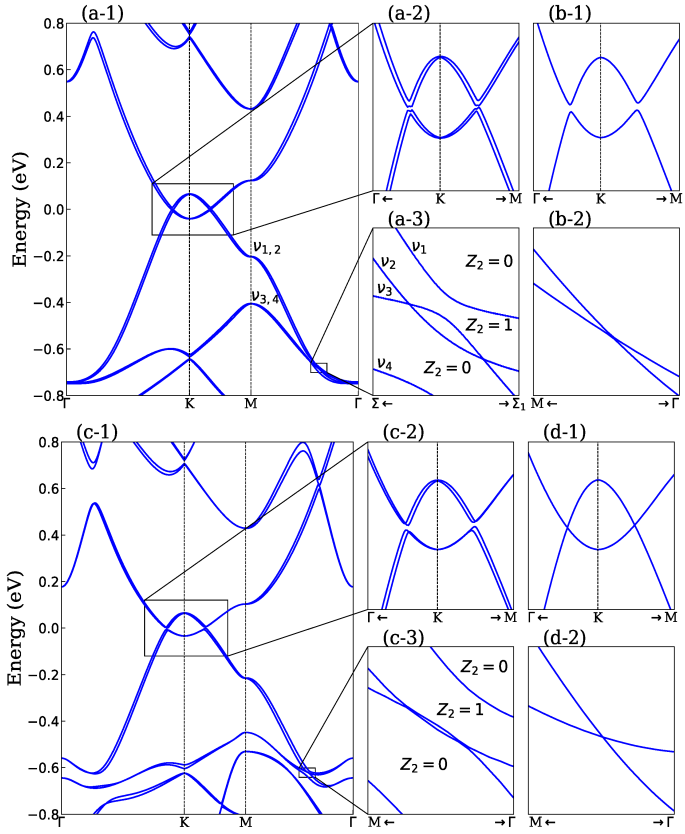

Figure 21 – Porous SiGe (a)-(b) and Ge (c)-(d) band structures, respectively. Figures (a) and (c) show the electronic band structure with SOC effect. In counterpart, (b) and (d) are without SOC inclusion. A small band gap between valence and conduction band is highlighted in (a-2) and (c-2) figures, while in (a-3) and (c-3) is the Weyl crossing pair. The same energy range is shown in (b) and (d), showing the behavior of bands without SOC.

due to its lower symmetric space group, the gap is already open without the inclusion of SOC (Fig. 21(b-1)). We compute the Z_2 index up to the Fermi level and, for both atomic configurations, a trivial behavior was verified, with $Z_2 = 0$. However, this trivial behavior arises due to an additional inverted band (ν_1), present in both systems. When we compute the Z_2 index up to the ν_2 band, we have found a nontrivial behavior, suggesting topological properties in both systems.

Regarding the interesting band crossings between ν_3 and ν_2 bands, and due to a non-trivial phase obtained up to ν_2, we investigate the topological properties of each crossing by using a derived 2D Weyl chirality (χ^{2D}) expression [118, 90, 165]

$$\chi^{2D} = \frac{1}{\pi} \oint_l \boldsymbol{A}(\boldsymbol{k}) \cdot d\boldsymbol{k}. \tag{107}$$

Where $\boldsymbol{A}(\boldsymbol{k})$ represents the Berry connection and l is the the closed loop in momentum space ($\boldsymbol{k}$) surrounding each crossing. For a trivial band crossing, $\chi^{2D} = 0$. In contrast, $\chi^{2D} \neq 0$ for a nontrivial touch point, where it can show integer numbers for the chiral charge, usually up to three [166]. By computing the Weyl chirality from each Dirac

crossing in the SiGe and Ge porous structures, we found that both crossings carry the same chirality ($\chi^{2D} = -1$), confirming their topological nature. By applying a C_6 symmetry, an opposite chirality point is observed. Over the entire Brillouin zone, the resultant chirality vanishes, which is in good agreement with the fermion doubling theorem [92], as we will discuss below. Although it is more commonly reported that Weyl crossing in a similar band shape produce opposite Weyl chiralities, the same chirality over a path has also been observed, but resultant chiral charge vanishing. This behavior has been reported in 3D systems, such as $Sn_{1-x}Pb_x$(Se, Te) and $AgBi(Cr_2O_7)_2$, [167, 168] as well as in the 2D systems like the Cr_2C [109].

In a 2D context, the Weyl Hamiltonian is studied with a reduction in dimensionality, which implies the absence of the ($k_z\sigma_z$). In this way, an additional crystal symmetry, such as C_2 or C_3, is pivotal to protect the stability of the 2D Weyl crossing [90]. As can be seen in Figure 22, applying a C_3 rotation to a specific Weyl point, it rotates to another point with the same chirality. In these systems, the C_3 symmetry is responsible for protecting these Weyl crossings, resulting in six pairs of Weyl nodes across the entire BZ. It is worth to note that, in the SiGe porous structure, the Weyl crossings are located out of the high-symmetry Γ-M line, along the Σ-Σ_1 direction (green line in Fig. 22(a)), due to its reducted space group symmetry. In the more symmetric Ge system, the Weyl points are located along the high-symmetry line, as show in inset from Fig. 22(b). The Weyl crossings from SiGe localize at (0.188,0.0075,0.0) and (0.185,-0.0103,0.0) points in units of 2π/a, here a is the lattice constant. For the porous Ge, since the topological points are located along a high-symmetry path, their respective positions are (0.216,0.0,0.0) and (0.206,0.0,0.0) at the same units. Unlike in time-reversal protected 3D Weyl crossings, where the chirality follows $\chi(\boldsymbol{k}) = \chi(-\boldsymbol{k})$, in the 2D counterpart, we have a different picture. For 2D Weyl systems with TRS protection, the chirality is ruled by $\chi(\boldsymbol{k}) = -\chi(-\boldsymbol{k})$. This property will be discussed in detail at the last section of this chapter.

Another key difference between 3D and 2D Weyl semimetals is related to the Berry curvature. In 3D systems, as discussed in Chapter 3, by starting from the Weyl Hamiltonian (80), the Berry curvature expression can be obtained as $\boldsymbol{\Omega}(\boldsymbol{k}) = \mp\boldsymbol{k}/2k^3$, which resembles the expression for the electric field [90, 72, 91]. This fact allows us two write the Berry curvature as monopole charges, with field lines connecting them. However, in 2D scenarios, the Berry curvature is described by a delta function formalism

$$\boldsymbol{\Omega}^{2D}_{k_0} = \pi\delta^2(\boldsymbol{k} - \boldsymbol{k_0})\boldsymbol{e}_{kz}. \tag{108}$$

Applying the time-reversal property in Eq. (108), we observe that in TRS-protected systems, $\boldsymbol{\Omega}(\boldsymbol{k}) = -\boldsymbol{\Omega}(-\boldsymbol{k})$, similarly to the chirality expression. This result indicates that a delta peak arises at the region of the Weyl crossing. Figure 23 shows the Berry curvature distribution for Ge structure in the $k_{x,y}$ plane. These crossing points are separated by smaller distances, the inset shows the zoom at the red delta point, where two delta peaks, one for each Weyl point, can be clearly seen.

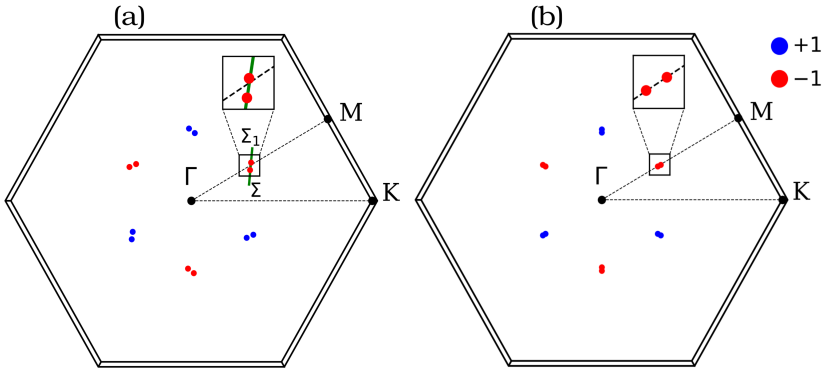

Figure 22 – Position of Weyl points and their chiralities in the Brillouin zone for SiGe (a) and Ge (b) atomic composition. In insets it is highlighted the position of WPs. Unlike to the Ge WPs, which is on the high-symmetry Γ-M line, the SiGe WPs are located in the Σ-Σ_1 path (green-line). Here, the blue (red) represents the positive (negative) chirality.

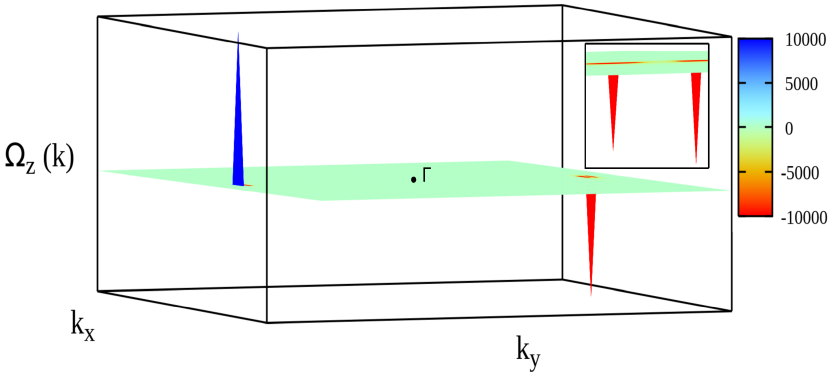

Figure 23 – Berry curvature distribution for a selected region in kx,ky plane in Porous Ge system. The aquamarine region is highlighted in the next figure. The blue (red) color indicates the Berry curvature of the Weyl point with positive (negative) chirality. The inset figure shows a zoom in the negative chiral pair, which in distance it can not be distinguished.

One of the main properties of systems that host Weyl crossings is the presence of topological Fermi arcs, a consequence of the bulk-boundary correspondence. Unlike in 3D systems, where the Fermi arcs can be observed in energy- or momentum-resolved density of states, in 2D configurations, since the edge path is one-dimensional, the 2D Fermi arc is more suitably observed in the energy-resolved band structure. By fixing an energy range and varying momentum directions, two high-density points corresponding to the projection of bulk WPs will be observed [21]. As the topological properties arise from the bulk crossings in both atomic configurations, we build a sufficiently large nanoribbon, as illustrated in Fig. 24, periodic only in the direction of the arrows. We project the band structure onto the $\overline{X}$-$\overline{M}$-$\overline{X'}$ path, which is equivalent to the 0 - π/a - $2\pi/a$ path along the $\overline{k_y}$ direction. As show in Figure 24(b), this path contains the projection of positive Weyl points (blue dashed line) and negative Weyl point (red dashed line).

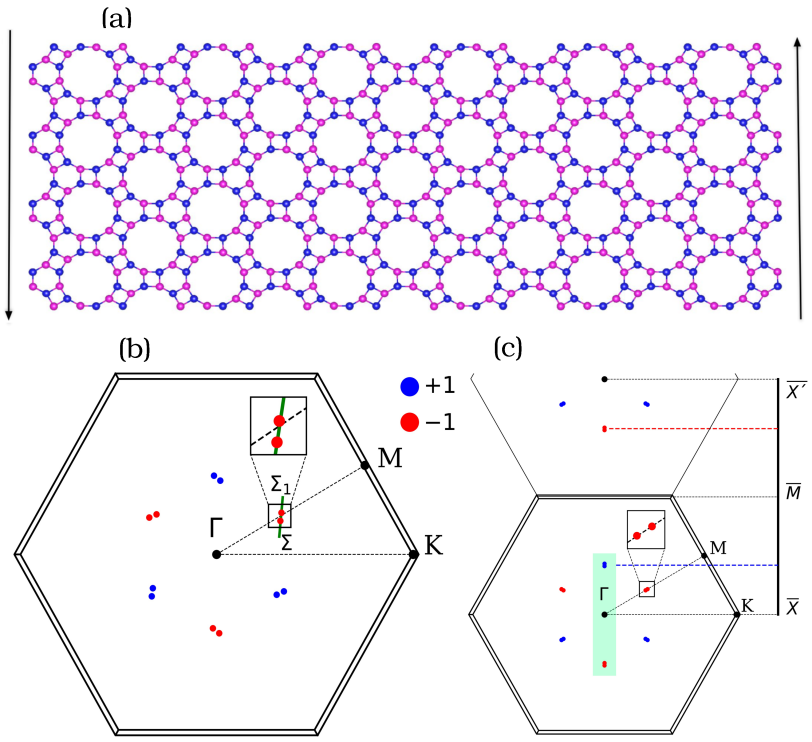

Figure 24 – Porous structure nanoribbon with periodicity only in the arrows direction (a). The projection of the Weyl points in the edge path which connects Weyl pairs with opposite chirality is shown in (c).

The projected band structures along the edge path for SiGe and Ge nanoribbons are shown in Figs. 25(a) and 25(b), respectively. Two edge states can be seen connecting the bulk projected Weyl points with opposite chiralities. These states are known as 2D Fermi arcs or Fermi strings [21]. Note that these Fermi arcs arise in pairs, with one for each Weyl point. Even though small inter-Weyl point distances are reported, a split of the arcs is noted. These edge states are double degenerated due to the same terminating edge, resulting in a degeneracy between left and right edge states. Due to the strong hybridization between the bulk and edge states, Fermi arcs originating from different Weyl points, beyond those projected in Figure 24, are hidden and cannot be observed. The Fermi arcs in these systems show a high Fermi velocity, with maximum energy values of -0.25 eV and -0.32 eV at π/a point for SiGe and Ge, respectively. These findings can make these materials suitable for high-speed devices and transport applications.

As the Fermi arcs are topological edge states, they exhibit the Kramers degeneracy at time-reversal invariant momentum points. However, in Figs. 25(a) and 25(b), the edge states are not degenerate at $\overline{M}$ point, indicating that some additional mechanism beyond the topological edge state lifts the Kramers degeneracy. To build the nanoribbon, a rigid cut in the bond length of the edge atoms was performed. Due to unpaired electrons that arises in dangling bonds, a local magnetic moment was created in both SiGe and Ge systems, with values of 0.27 and 0.12 μ_B, respectively. These local magnetic moments

are responsible for opening the band gap at the TRIM point. To avoid the non-vanishing magnetism originated from dangling bonds, we performed the hydrogen passivation at the nanoribbon edges. We used a reconstructed DFT nanoribbon to investigate the topological states. To avoid interactions between both sides, we build a sufficiently large nanoribbon with a width of 11.6 nm. After extracting the fully optimized bond lengths Si-H = 1.51 Å and Ge-H = 1.57 Å, we calculated the band structure of the nanoribbon using first-principles. As shown in Figs. 25(c) and 25(d), when projected onto edge atoms, two high-intensity bands arise from bulk WPs. These bands disperse with a high Fermi velocity and penetrate into the bulk at the position of opposite chirality WPs, similarly as non-saturated bands. However, with passivation, the local magnetic moment vanishes, recovering the Kramers degeneracy at $\overline{M}$ point. Even after hydrogen passivation, the bulk states also shows a strong hybridization with the edge, limiting the observation of Fermi arcs originated from different WPs.

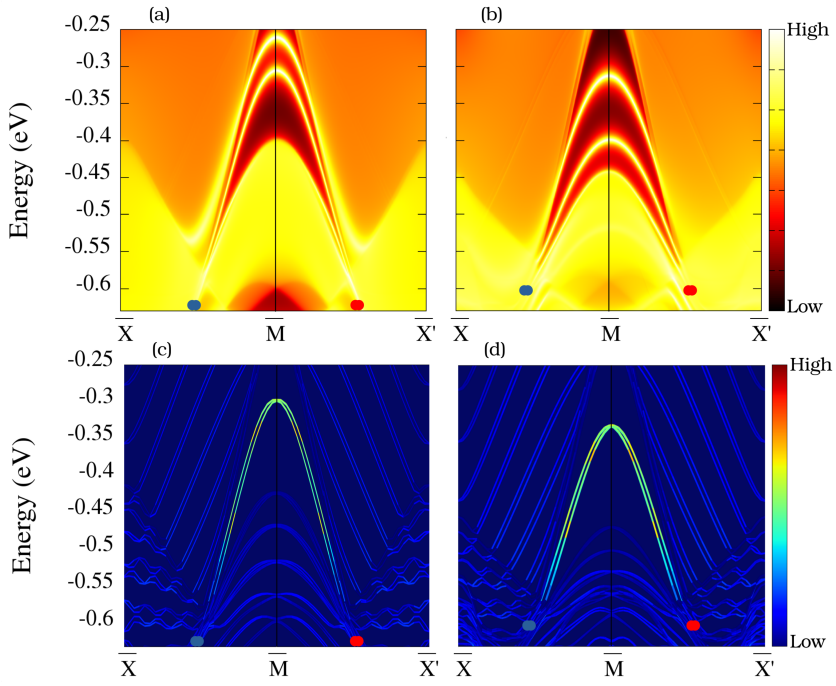

Figure 25 – Band structure plot with the Weyl points projection for porous SiGe (a) and (c) system without and with hydrogen saturation, respectively. Figures (b) and (d) show the same, but for Ge counterpart. The blue and red circles represents the Weyl point chirality of the projected Weyl points. The high intensity edge states corresponds to the 1D Fermi arcs.

In Weyl semimetals, the Fermi arcs do not follow a specific spin-polarization rule. A recent report shows that the spin texture of the Fermi arc in a 2D Weyl system is predominantly aligned along the $\langle S_z \rangle$ component [21], whereas other studies reveal non-collinear spin polarization configurations, with $\langle S_y \rangle$ and $\langle S_x \rangle$ also contributing to the spin-polarization vector [96, 98, 169]. As can be seen in Figs. 26(a)-(c), in the non-passivated edge Ge nanoribbon, the Fermi arcs have dominant behavior in $\langle S_z \rangle$, but with

smaller $\langle S_x \rangle$ and $\langle S_y \rangle$ contributions, exhibiting a non-collinear spin channel at the edge. In the SiGe composition, Figs. 26(d)-(f), the $\langle S_x \rangle$ and $\langle S_z \rangle$ components contribute equally to the Fermi arcs, also exhibiting a non-collinear edge state. With the edge passivation, in both cases, the edge bands show a similar spin-texture behavior, restoring the Kramers degeneracy.

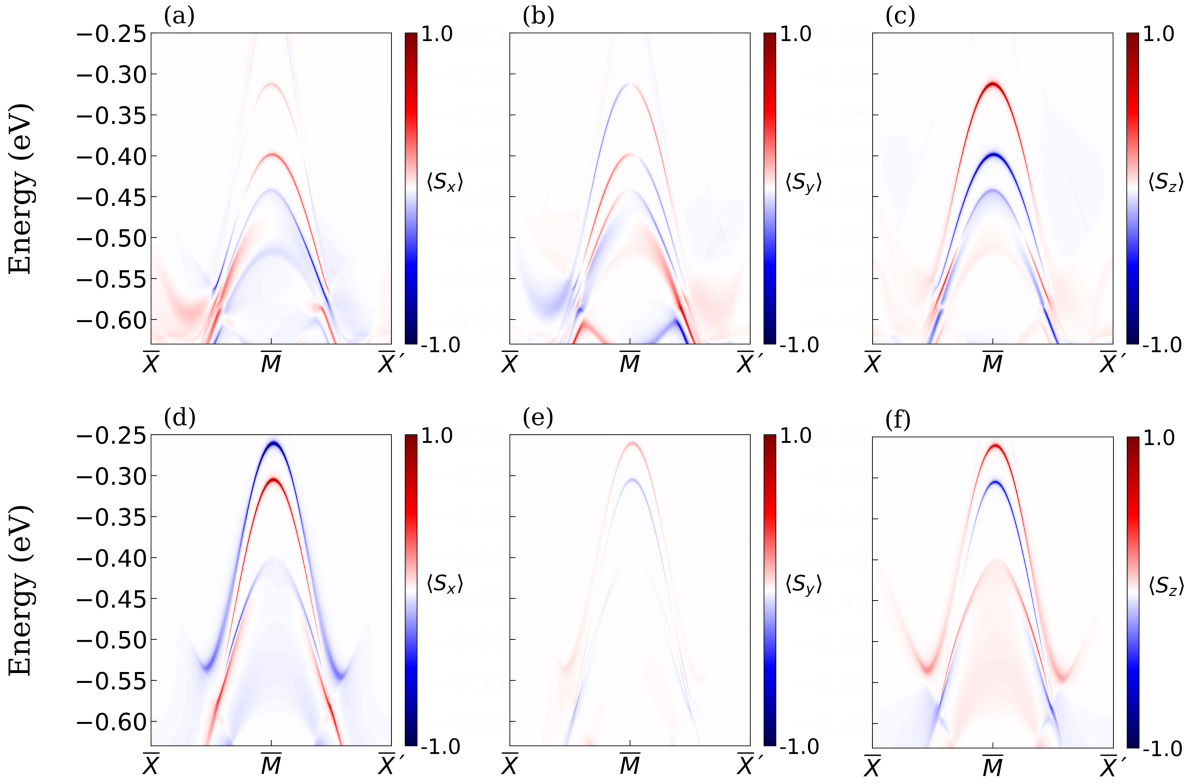

Figure 26 – Spin components plots of the Fermi arcs in Ge (a)-(c) and SiGe (d)-(f) structures. The red and blue colors indicates the positive and negative spin values, respectively.

5.3 Weyl equation analysis for 2D systems

In this section we perform a thorough analysis of Weyl equation applied to a two-dimensional context. We have found that the topological properties match with the findings obtained from DFT.

In 1929, Hermann Weyl proposed a particular case of the Dirac equation, which became known as the Weyl equation [88]. Weyl's study has a significant impact on different physics areas, such as cosmology and condensed matter physics [89, 33, 6]. The solution of the equation proposed by Weyl describes massless fermions. As we previously discussed in

Chapter 3, the Weyl Hamiltonian is given by

$$H = \hbar c \boldsymbol{k}\cdot\boldsymbol{\sigma},$$

where $\hbar$ and c represent the reduced Planck constant and the speed of light, respectively, $\boldsymbol{k}$ corresponds to the momentum, and $\boldsymbol{\sigma}$ represents the Pauli matrices. In condensed matter physics, instead of using the speed of light, it is used the Fermi velocity. In a typical Dirac crossing, the Fermi velocity (v_F) can reach the order of 10^6 m/s [146, 170, 171], here we use $v_F = 1$ for convenience. However, to simplify the notation, we use natural units mentioned in Chapter 2. The Weyl Hamiltonian for an isotropic xy-plane is given by

$$H = k_x\sigma_x + k_y\sigma_y. \tag{109}$$

In terms of the Pauli matrices ($\sigma_{x,y}$), the 2D Weyl Hamiltonian can be rewritten as

$$H = k_x \begin{pmatrix} 0 & 1 \\ 1 & 0 \end{pmatrix} + k_y \begin{pmatrix} 0 & -i \\ i & 0 \end{pmatrix}, \tag{110}$$

or, in a compact form

$$H = \begin{pmatrix} 0 & k_x - ik_y \\ k_x + ik_y & 0 \end{pmatrix}. \tag{111}$$

Which shows a vanishing diagonal contribution, that corresponds to the term associated with the k_z component in its 3D counterpart.

5.3.1 Eigenenergies and Eigenfunctions

Through the Schrödinger equation, (44), we can determine the eigenenergies and eigenfunctions of the Weyl Hamiltonian (111). The Schrödinger equation with the Weyl Hamiltonian is given by

$$\begin{pmatrix} 0 & k_x - ik_y \\ k_x + ik_y & 0 \end{pmatrix} \begin{pmatrix} \varphi_1 \\ \varphi_2 \end{pmatrix} = \epsilon \begin{pmatrix} \varphi_1 \\ \varphi_2 \end{pmatrix}. \tag{112}$$

The eigenvalues are obtained using the characteristic equation, given by $det(A - \lambda I)$, which allows us to determinate the corresponding eigenvalues

$$\begin{vmatrix} -\epsilon & k_x - ik_y \\ k_x + ik_y & -\epsilon \end{vmatrix} = 0, \tag{113}$$

resulting in eigenenergies equation

$$\epsilon = \sqrt{k_x^2 + k_y^2}. \tag{114}$$

Consequently, rewritten using $k^2 = k_x^2 + k_y^2$, the key result for the behavior of relativistic fermions, $\epsilon = \pm k$, is obtained. In a condensed matter physics context, the solution is expressed by $\epsilon = \pm v_F k$. This solution leads to an interesting physical behavior, the

positive and negative eigenenergy values imply that Weyl points always arise in pairs, with the same dispersion but in opposite momentum directions.

To derive the respective eigenfunctions, which are important in the study of topological invariants and the Berry curvature, we consider the eigenvalue $\epsilon = -k$. Inserting the corresponding eigenvalue into Eq. (112), results in

$$\begin{pmatrix} k & k_x - ik_y \\ k_x + ik_y & k \end{pmatrix} \begin{pmatrix} \varphi_1 \\ \varphi_2 \end{pmatrix} = \begin{pmatrix} 0 \\ 0 \end{pmatrix}, \tag{115}$$

which yields the following equation

$$k\varphi_1 + (k_x - ik_y)\varphi_2 = 0. \tag{116}$$

Or, in a more suitable form

$$\varphi_1 = \frac{-k_x + ik_y}{k}\varphi_2. \tag{117}$$

Using the normalization condition of the coefficients $|\varphi_1|^2 + |\varphi_2|^2 = 1$, it results in

$$\frac{(-k_x + ik_y)\,(-k_x - ik_y)}{k^2}\varphi_2^2 + \varphi_2^2 = 1. \tag{118}$$

Consequently, we obtain

$$\varphi_2 = \frac{1}{\sqrt{2}}. \tag{119}$$

Using the result from Eq. (117) and inserting Eq.(119), we can rewrite as

$$\varphi_1 = \frac{1}{\sqrt{2}}\frac{-k_x + ik_y}{k}. \tag{120}$$

To simplify the notation, we use cylindrical coordinates $k_x = k\cos\theta$, $k_y = k\sin\theta$, while k_z remains unchanged. With this, we can rewrite the previous equation in the form

$$\varphi_1 = \frac{1}{\sqrt{2}}\frac{-k\cos\theta + ik\sin\theta}{k}, \tag{121}$$

By means of Euler's relation ($e^{-i\theta} = \cos\theta - i\sin\theta$), we obtain the coefficient φ_1 as

$$\varphi_1 = -\frac{1}{\sqrt{2}}e^{-i\theta}, \tag{122}$$

which leads to both coefficient terms

$$\begin{cases} \varphi_1 = -\frac{1}{\sqrt{2}}e^{-i\theta}, \\ \varphi_2 = \frac{1}{\sqrt{2}}. \end{cases} \tag{123}$$

The eigenfunction expression is given by

$$\psi = \frac{1}{\sqrt{2}}\begin{pmatrix} -e^{-i\theta} \\ 1 \end{pmatrix}. \tag{124}$$

It is worth noting that, for the corresponding $\epsilon = +k$ eigenvalue, the only difference remains in the sign of the φ_1 term, resulting in $\varphi_1 = +\frac{1}{\sqrt{2}}e^{-i\theta}$, which leads to the expression for the eigenfunctions

$$\psi_{\pm k} = \frac{1}{\sqrt{2}} \begin{pmatrix} \pm e^{-i\theta} \\ 1 \end{pmatrix}. \tag{125}$$

Those results are important for the analysis of topological properties, as we will discuss below.

5.3.2 Topological analysis

Once we have obtained the eigenfunctions for the 2D isotropic Weyl Hamiltonian, we can further investigate the topological characteristics by estimating the Berry quantities, i.e., phase, connection and curvature, and Chern number. The Berry connection is given by

$$\boldsymbol{A}(\boldsymbol{k}) = i\langle\psi_{\pm k}|\nabla_{\boldsymbol{k}}|\psi_{\pm k}\rangle. \tag{126}$$

Here $\nabla_{\boldsymbol{k}}$ denotes the gradient operator in momentum space. As our analysis was performed in cylindrical coordinates, the gradient operator in this coordinate system is given by

$$\nabla_{\boldsymbol{k}} = \frac{\partial}{\partial k}\boldsymbol{e}_k + \frac{1}{k}\frac{\partial}{\partial\theta}\boldsymbol{e}_\theta + \frac{\partial}{\partial k_z}\boldsymbol{e}_z. \tag{127}$$

It can be noted that the only nonzero component is in θ direction, where the derivative leads to

$$\frac{\partial}{\partial\theta}|\psi_{\pm k}\rangle = \frac{1}{\sqrt{2}} \begin{pmatrix} \mp ie^{-i\theta} \\ 0 \end{pmatrix}. \tag{128}$$

Consequently, performing the expected value operation, and taking into consideration the imaginary index from Eq. (126), the Berry connection is given by

$$\boldsymbol{A}(\boldsymbol{k},\theta) = \pm\frac{1}{2k}\boldsymbol{e}_\theta. \tag{129}$$

Unlike 3D systems, where the chiral charge is calculated by integrating over a closed Fermi sphere surrounding each Weyl point, in its 2D counterpart, the Berry flux is obtained by integrating the Berry connection (Eq. (129)) over a closed loop (l) around each Weyl point according to the following expression

$$\gamma = \oint_l \boldsymbol{A}(\boldsymbol{k})\cdot d\boldsymbol{k}, \tag{130}$$

which corresponds to the Berry phase, derived in Eq. 55. Note that, since $dk = kd\theta$, by calculating the integrating the Berry connection (Eq. (129)) into the Berry phase (Eq. (129)) over the interval $[0,\ 2\pi]$, we obtain $\gamma = \pm\pi$. This result defines the two-dimension Weyl chirality as

$$\chi^{2D} = \frac{1}{\pi}\oint_l \boldsymbol{A}(\boldsymbol{k})\cdot d\boldsymbol{k} = \pm 1. \tag{131}$$

Another key property of Weyl physics in condensed matter is the Berry curvature, which is denoted by $\boldsymbol{\Omega} = \nabla \times \boldsymbol{A}$. In cylindrical coordinates, the curl of the Berry connection vanishes for all components except in $\boldsymbol{e}_{k_z}$, where

$$\nabla \times \boldsymbol{A} = \frac{1}{k}\frac{\partial}{\partial k}\left(\pm k \frac{1}{2k}\right)\boldsymbol{e}_{k_z}. \tag{132}$$

It can be verified that, when $k \neq 0$, the Berry curvature vanishes. However, when $k = 0$ an indeterminate form is obtained, which means that the Berry curvature exhibits a peak at the position of the Weyl crossings, this is a signature of the Dirac delta function. We conclude that the two-dimensional Berry curvature is

$$\boldsymbol{\Omega} = \pm\pi\delta^2(\boldsymbol{k})\boldsymbol{e}_{k_z}. \tag{133}$$

From Stokes' theorem, we can rewrite the Berry phase (Eq. (130)) in terms of the Berry curvature

$$\oint \boldsymbol{A} \cdot d\boldsymbol{k} = \int \nabla \times \boldsymbol{A} \cdot d\boldsymbol{s}. \tag{134}$$

The Berry curvature obtained is a Dirac delta function. In this way, we can calculate the right-hand side integral from the previous equation. With $ds = kd\theta dk$, the result of the integral is $\pm\pi$. This result leads to the derived Chern number expression

$$C = \frac{1}{\pi}\int_{BZ}^{2D} \boldsymbol{\Omega} \cdot d\boldsymbol{s} = \pm 1. \tag{135}$$

This equation provide an alternative method for calculating the Weyl chirality, expressed in terms of the Berry curvature.

Chapter 6

Quantum anomalous Hall effect in 1T-CrX_2 monolayers

Since the experimental achievement of 2D materials with the graphene in 2004 [8], the prediction and synthesis of new 2D materials have become one of the main topics in materials science. Practical applications, such as in spintronics and quantum computation fields, require the 2D character [102, 172]. Beyond the architecture, many of these applications also require intrinsic magnetic properties, such as in memory storage. In this work, we investigate the emergence of the quantum anomalous Hall effect in 1T monolayers with two different atomic configurations. In this chapter, we predict the 1T-$CrBi_2$ monolayer, thus extending the list of theoretically predicted magnetic materials in 2D structures, and we investigate their magnetic and topological properties [1].

6.1 Stability of 1T-MX structures

In the class of two-dimensional materials, different types of layer arrangements have been reported, such as 1T, 1T' and 2H structures. The 1T structure is composed of three planes of atoms, in which the atoms located in the central plane form six chemical bonds, three bonds to each atomic plane. In this chapter, we investigated the 1T-MX_2 monolayers (Fig. 27), here M represents the chromium atom and X was studied with two different group-V elements, Bi and Sb atoms. In this 1T phase, in both atomic configurations, the structure belongs to the P$\bar{3}$m1 (or No. 164) space group symmetry. We performed the ionic relaxation for both systems, resulting in a fully optimized lattice parameter $a = b = 3.43$ Å for the 1T-$CrBi_2$ structure, with a Cr-Bi bond length of 2.97 Å, and a buckling height (Δ) of 4.63 Å. For the 1T-$CrSb_2$ monolayer, our results show $a = b = 3.28$ Å, a Cr-Sb bond length of 2.67 Å, and $\Delta = 4.43$ Å. We also performed phonon calculations for the optimized free standing systems, which show that both atomic compositions are dynamically stable, without negative phonon frequencies, as shown in

[1] The results discussed in this chapter were published in Ref. [173]

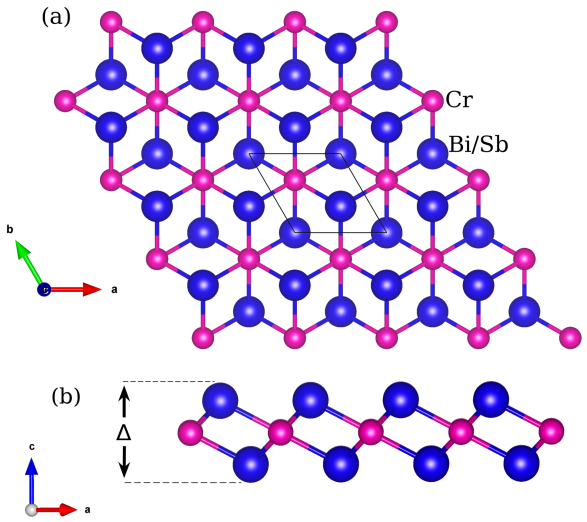

Figure 27 – Crystal structure of 1T-CrX_2 (X=Bi, Sb) monolayer at the top (a) and side views (b). The magenta spheres represent the Cr atoms and the blue counterpart Bi or Sb atoms. The black line indicates the unit cell.

Figs. 28(a) and 28(b). In addition to dynamical stability, we investigate, using *ab initio* molecular dynamics (AIMD) calculations, the thermal stability at 300 K over a time range of 10 ps, as shown in Figs. 28(c)-(d). As highlighted in the final snapshot of the AIMD results, insets in Figs. 28(c)-(d), both Bi and Sb compositions are thermally stable over a 10 ps range at 300 K.

Interestingly, both structures are dynamically stable, without imaginary phonon frequencies, under a wide range of biaxial tensile strain (TS). In both systems, we noted a reduction in buckling height as the lattice parameter increased (Figs. 28(e) and 28(f)). Our results show stability up to 20% and 25% for $CrBi_2$ and $CrSb_2$, respectively (Figs. 29(a) and 29(b)). These results, obtained through phonon calculations, are validated by means the ultimate strain-energy curve as a function of biaxial TS (Fig. 29(c)). This curve shows maximum energy points (critical points) near the values predicted by phonon dispersions. For both structures, the strain energy increases with the biaxial TS, reaching a critical point before decreasing. This decrease in strain energy indicate structural phase transitions or ruptures in atomic bonds [174]. However, these systems do not show structural phase transitions under the applied biaxial TS, leading to the breaking of Cr-X chemical bonds. Beyond the dynamical stability, we also investigated the thermodynamic stability of the free standing (FS) systems and at the ultimate tensile strain by calculating both cohesive and formation energies. The cohesive energy (E_{coh}) is given by [49, 53]

$$E_{coh} = \frac{E_{tot} - E_{Bi/Sb} - E_{Cr}}{N}. \tag{136}$$

In this notation N is the number of atoms in the unit cell, E_{tot} represents the total energy of the systems with or without external strain, $E_{Bi/Sb}$ and E_{Cr} are the total energies of an isolated Bi (or Sb) and a Cr atom, respectively. For the 1T-$CrBi_2$ system, our cohesive

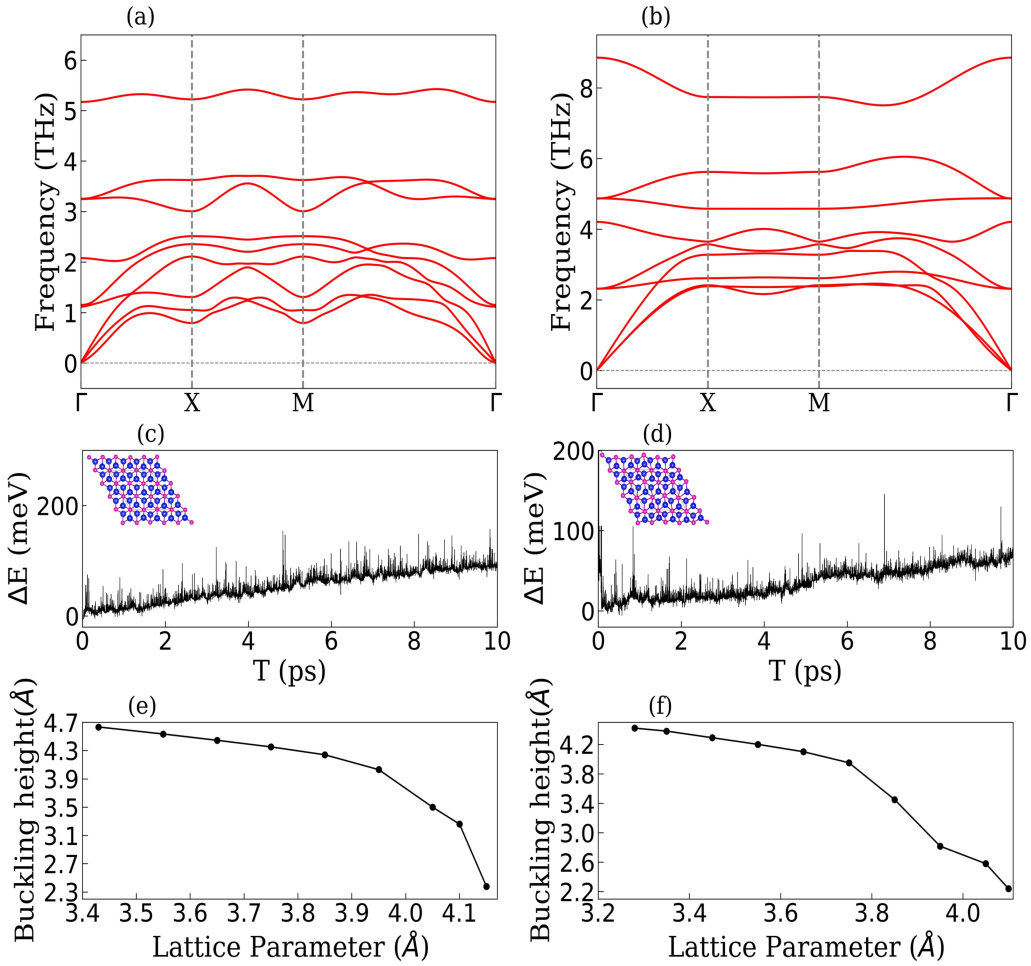

Figure 28 – Dynamical and thermal stabilities for 1T-CrX_2 monolayers. In (a) and (b) is shown the phonon spectra for 1T-$CrBi_2$ and 1T-$CrSb_2$ monolayers, respectively. For these respective systems, (c) and (d) show the *ab initio* molecular dynamics at 300 K, with the final snapshot highlighted in the inset. The buckling height as a function of the lattice parameter is shown in (e) and (f) for Bi and Sb compositions, respectively.

energies results were −3.10 eV/atom and −2.68 eV/atom for free standing and highest tensile strained systems, respectively. For the Sb counterpart, the calculated energies were −2.97 eV/atom in the strain-free configuration and −2.78 eV/atom under the highest TS condition. It is worth to note that, with negative values, both systems are energetically favorable, even under the highest tensile strain. To further confirm the stability, we calculated the formation energy

$$E_{Form} = E_{tot} - E_{Bulk(Bi/Sb)} - E_{Bulk(Cr)}. \tag{137}$$

Where $E_{Bulk(Bi/Sb)}$ represents the energy of the bulk system composed uniquely by Bi or Sb atoms in a 3D unit cell (U.C.), and $E_{Bulk(Cr)}$ corresponds to the same, but for Cr atoms. Similarly to the cohesive energy, negative formation energy values were obtained for 1T-$CrBi_2$, in free standing (−1.66 eV/U.C.) and under the highest tensile-strain regime

Table 1 – Cohesive and formation energies of CrX_2 systems in a free standing (FS) configuration, and at the ultimate tensile strain (TS) form. Here, the Cohesive energy is given in eV/atom, and the formation energy is expressed in eV per unit cell.

System	Cohesive energy	Formation energy
FS $CrBi_2$	-3.10	-1.66
TS $CrBi_2$	-2.68	-0.35
FS $CrSb_2$	-2.97	-0.82
TS $CrSb_2$	-2.78	-0.25

(−0.35 eV/U.C.), indicating thermodynamic stability even at critical TS value. In 1T-$CrSb_2$ configuration, the values are −0.82 eV/U.C. and −0.25 eV/U.C. for FS and highest TS systems, respectively. Our calculated cohesive and formation energies for the FS 1T-$CrSb_2$ system are in good agreement with Wang *et al.* [175]. These results for cohesive and formation energies are summarized in Table 1.

6.2 Magnetic properties

The unpaired electrons in *d*-orbitals from Cr atoms give rise to magnetic properties in both atomic configurations. In strain-free systems, the intrinsic magnetism per Cr atom is 4.1 μ_B and 3.53 μ_B for 1T-$CrBi_2$ and 1T-$CrSb_2$, respectively. This magnetism in Cr atoms leads to a magnetic polarization of Bi and Sb atoms, with a non-zero opposite magnetization of -0.09 μ_B and -0.05 μ_B for their neighboring Bi and Sb atoms, respectively. This nonzero magnetization, resulting from the interaction with magnetic atoms, is one of the main characteristics of superexchange coupling [176]. It is well known that conventional DFT approaches, such as LDA and GGA, do not provide accurate results for strongly correlated systems [55, 49]. To improve the analysis, in this work, we use the GGA+U method, with Dudarev's functional [63]. In this way, we take into account the effective

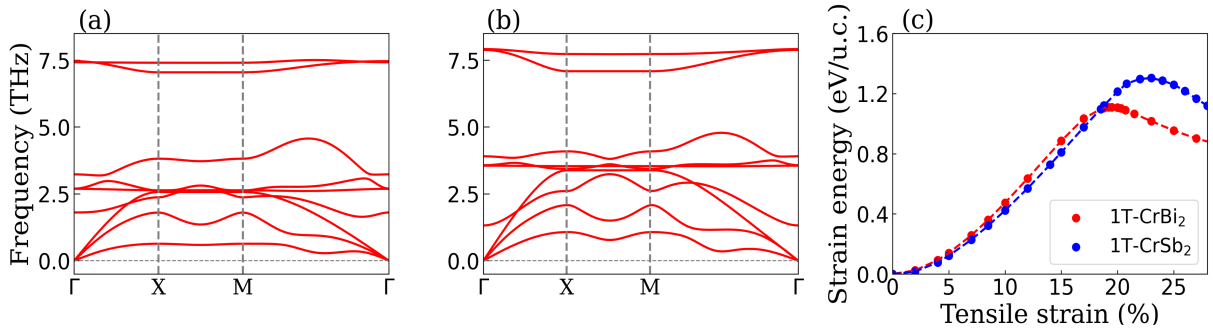

Figure 29 – Phonon dispersion for the ultimate tensile strained 1T-$CrBi_2$ monolayer (20%) in (a) and for the ultimate strain value for 1T-$CrSb_2$ (25%) in (b). Strain-energy curve as function of the biaxial tensile strain is shown in (c).

U term. The U_{eff} parameter for systems composed of Cr and X atoms, where (X = Bi, Sb), is reported in the literature to range between 2.0 eV and 3.5 eV [175, 177, 178, 179]. Unless otherwise specified, we used U_{eff} = 2.0 eV for the Sb configuration and U_{eff} = 3.0 for the Bi counterpart.

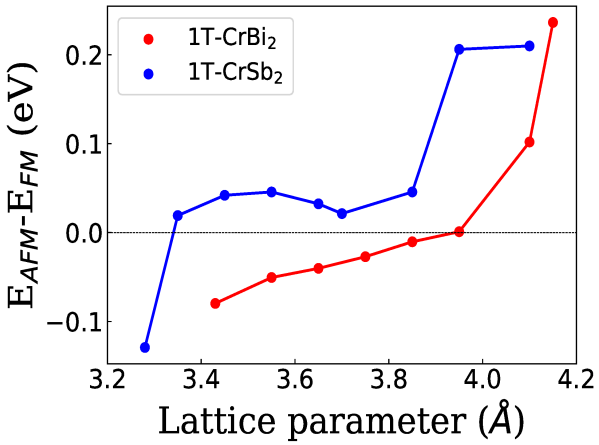

Figure 30 – Total energy difference between the Cr atoms aligned in AFM and FM configuration as function of the biaxial tensile strain. The positive (negative) values indicate the AFM (FM) phase as most stable in comparison with FM (AFM) alignment.

The ground magnetic phase for both systems in their free standing form is antiferromagnetic with an in-plane easy magnetization axis. However, external effects, such as strain and electric field, can significantly affect the ground magnetic phase and easy axis [135, 180, 181, 182]. By increasing the biaxial TS, a magnetic phase transition from AFM to FM is observed in both systems, as shown in Fig. 30. While in $CrSb_2$ the magnetic phase transition occurs only around 2%, for the $CrBi_2$ counterpart, a larger strain (close to 15%) is required to verify this phase transition. Although a decrease in Cr magnetic moment is observed at the highest tensile strain regime, reaching 3.85 μ_B and 3.36 μ_B for $CrBi_2$ and $CrSb_2$, respectively, both structures show the FM phase as GMP.

Table 2 – Calculated magnetic anisotropy energy values (in meV) for the 1T-$CrBi_2$ monolayers under different external biaxial tensile strain. The easy magnetization axis is located in-plane (out-of-plane) when the MAE values are negative (positive).

Strain	MAE
0%	-8.81
6.5%	-6.27
15%	-1.26
19%	9.16
20%	5.3

Notably, tensile strain affects not only the GMP but also the easy magnetization axis. Through the magnetic anisotropy energy (MAE), defined as the difference between the

Table 3 – Calculated magnetic anisotropy energy values (in meV) for the 1T-$CrSb_2$ monolayers under different external biaxial tensile strain. The easy magnetization axis is located in-plane (out-of-plane) when the MAE values are negative (positive).

Strain	MAE
0%	-0.58
8.2%	-0.40
17%	-0.20
23%	0.18
25%	1.46

total energy with the magnetic moment aligned IP and OP, we calculated the MAE values for selected external strains, as shown in Tables 2 and 3. The easy axis transit from IP to OP with an increase in TS for both $CrBi_2$ and $CrSb_2$. The negative (positive) values indicate an IP (OP) easy magnetization axis.

In the many-electron effects context, the GMP is affected not only by external strain, but also by the increase or decrease of correlation effects. It is well-known that in an external interaction-free material, the correlation term simulated in DFT is fixed, with a given U_{eff} value, which can be accurately predicted using linear response method [69]. However, extrinsic effects, such as strain modulation and electric field, may require different U_{eff} values in DFT simulations. For free standing 1T-$CrSb_2$, with $U_{eff} = 4.0$ eV, the GMP is FM instead of AFM. Table 4 shows the energy difference between the magnetic atoms in FM alignment, set as the reference due to its minimal value, and different variations of antiferromagnetism: Néel, stripy and zigzag, calculated with $U_{eff} = 4.0$ eV. Even under different biaxial TS values, the FM phase remains the GMP for this U_{eff} value.

Table 4 – Relative energy calculations, given in meV, for the 1T-$CrSb_2$ monolayer with the $U_{eff} = 4$ eV. The ground magnetic phase is ferromagnetic, which is set as zero, and the values reflects the total energy difference with relation to Néel, Stripy and Zigzag magnetic phases.

Strain	FM	Néel	Stripy	Zigzag
0%	0.0	28.32	28.20	28.23
8.2%	0.0	74.12	74.18	74.20
11.2%	0.0	33.77	33.69	33.72
20.0%	0.0	29.44	29.22	29.76
23.4%	0.0	232.07	232.23	232.20
25.0%	0.0	263.05	263.0	263.01

In the highest tensile strain regime, where both systems are ferromagnetic, the U_{eff} term plays a crucial role in the easy magnetization axis location. Figures 31(a) and 31(b) show an easy axis transition from OP to IP in $CrBi_2$ and $CrSb_2$, respectively. It is worth noting that the FM configuration remains OP in the most plausible U_{eff} regime, with a

critical transition point at 4.6 eV for Bi and 2.8 for Sb compositions. The FM OP order is crucial for the topological behavior of these systems, as will be discussed in the next section.

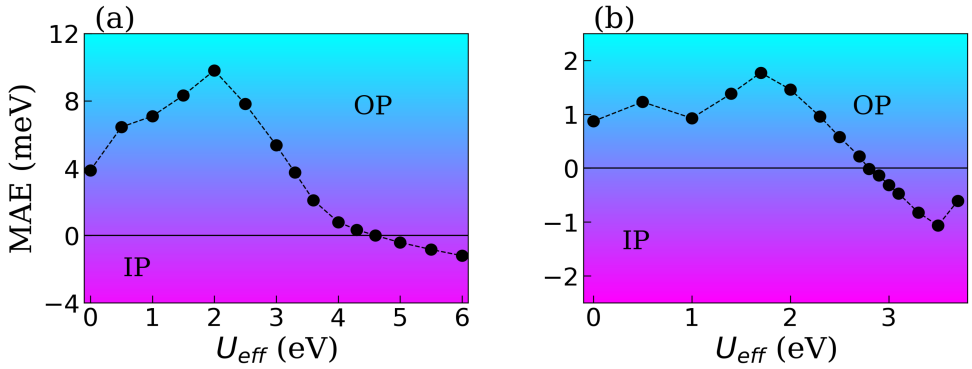

Figure 31 – Magnetic anisotropy energy (given in meV) as function of U_{eff} parameter for ultimate tensile strained 1T-$CrBi_2$ (a) and 1T-$CrSb_2$ (b). The positive and negative MAE values indicate the easy magnetization axis out-of-plane and in-plane, respectively.

6.2.1 Curie Temperature

In the context of magnetic materials, it is important to evaluate their critical temperatures. Exposing materials to temperatures above their critical values leads to the loss of their magnetic order. For FM materials, this critical temperature is named Curie temperature. For AFM materials, it is called the Néel temperature. For practical applications, such as memory storage and quantum computing [183, 172, 184], it is desired that these temperatures reach near or above room temperature [23]. However, in 2D materials, due to experimental limitations, the highest Curie temperature experimentally achieved is close to 45 K [24], which enhances the search for 2D magnetic materials with high critical temperatures. Motivated by this, we investigated the Curie temperature of the 1T CrX_2 monolayers at the ultimate tensile strain. In the DFT context, there are two most well-known methods to estimate the Curie temperature. The first one consists of using mean-field theory, however, this method significantly overestimates the Curie temperature, leading to an empirical analysis that concludes that the overestimates are about 50% [108, 185]. The second is the Monte Carlo method.

In this work, the Curie temperature (T_C) was estimated through Monte Carlo simulations based on the Heisenberg model, which Hamiltonian is given by

$$H = -\sum_{i,j} J_{i,j}\, S_i \cdot S_j - A\sum_i (S_i^z)^2. \tag{138}$$

Here, the $J_{i,j}$ term represents the coupling between the spins $S_{i,j}$. The magnetic anisotropy term A is usually neglected due to the low MAE magnitudes, on the order of μeV. However, due to significant MAE values found in these systems, as shown in Table 5, it is

important to consider it. Table 5 summarizes the 1T-CrX_2 magnetic properties under extreme biaxial tensile strain.

Table 5 – Magnetic parameters for 1T-CrX_2 monolayers at the ultimate tensile strain. The magnetization per Cr atom is given in μ_B, the magnetic anisotropy energy in meV, while the coupling parameter ΔE_{AFM-FM} per Cr atoms in the system is also given in meV. The Curie temperature is shown in Kelvin.

CrX_2	Mag/Cr	MAE	$\Delta E_{AFM-FM}/N$	T_C
$CrBi_2$	3.85	5.30	58	180
$CrSb_2$	3.36	1.46	53	170

Figure 32 shows the magnetic moment as a function of temperature, obtained through Monte Carlo simulations, for both 1T-$CrBi_2$ (red) and 1T-$CrSb_2$ (blue) monolayers. Both curves behave similarly until reaching the critical Curie temperature, which for 1T-$CrBi_2$ is estimated as 180 K and 1T-$CrSb_2$ as 170 K. These temperatures are higher than the experimentally reported in 2D magnetic materials, such as CrI_3, which has a Curie temperature of 45 K [24], and Fe_3GeTe_2 monolayer, which is 20 K [27, 23]. It is important to note that, as we will discuss below, both structures show the quantum anomalous Hall phase. In this context, the experimentally observed Curie temperatures for quantum anomalous Hall systems runs over from a few Kelvins, our estimated Curie temperatures suggest that these systems are promising for topological applications.

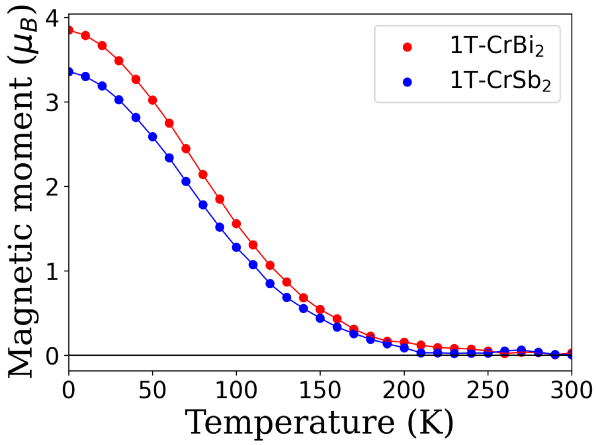

Figure 32 – Magnetic moment as function of the temperature for 1T-$CrBi_2$ monolayer under 20% of biaxial tensile strain in red symbols and in blue for 1T-$CrSb_2$ monolayers under 25%.

6.3 Quantum Anomalous Hall effect

In this section, we discuss the emergence of the quantum anomalous Hall effect in high tensile-strained 1T-CrX_2 monolayers. It is known that the SOC strength is proportional

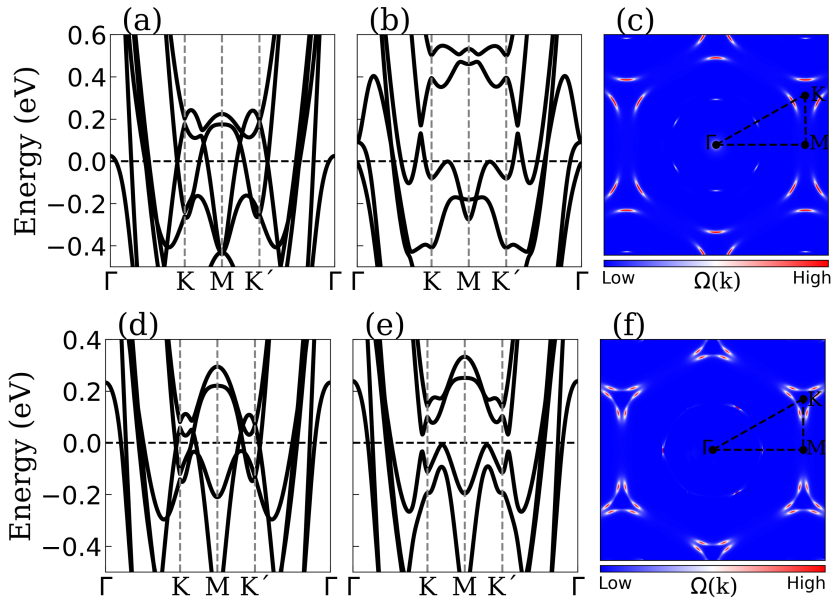

Figure 33 – Band structure without (a) and with (b) SOC effects in ultimate tensile-strained 1T-$CrBi_2$ monolayer, additionally (c) shows the Berry curvature distribution in momentum space. For the Sb counterpart, at the ultimate tensile strain, the band structures without and with SOC are shown in (d) and (e), respectively, and (f) shows the Berry curvature plot for this system.

to the atomic number (Z). In this context, both Bi (Z = 83) and Sb (Z = 51) atoms show a strong intrinsic SOC, which drives topological properties in many systems containing these atoms [186, 187]. The band structures without SOC for the highest tensile strained $CrBi_2$ and $CrSb_2$ systems are shown in Figs. 33(a) and 33(d), respectively. It can be noted that, near to the high-symmetry K-point, Dirac crossings arise close to the Fermi level (black dotted line). With the inclusion of SOC the Dirac points degeneracy is lifted, resulting in a clean band gap in K-M-K' path, as shown in Figs. 33(b) for Bi composition and 33(e) for Sb counterpart. In the K-Γ direction, the lower states cross the Fermi level. However, even at higher energies values, those bands split by SOC do not cross each other. Our results show a continuous gap between lower and higher bands, which is crucial for the topological invariant calculation, as will be discussed below. In the Bi atomic configuration, the band gap is located above the Fermi level, while in the Sb structure it remains at this level.

To investigate the topological properties at the highest strained systems, we build a tight-binding model extracted from DFT results. The Berry curvature, defined in Eq. (62), can be computed using the Kubo formula [75]. In terms of the velocity operators $v_{x,y}$, the Berry curvature over all occupied states is given by

$$\boldsymbol{\Omega}(\boldsymbol{k}) = -\sum_{n}\sum_{m\neq n} f_n \frac{2\,\mathrm{Im}\langle\psi_{n\boldsymbol{k}}|v_x|\psi_{m\boldsymbol{k}}\rangle\langle\psi_{m\boldsymbol{k}}|v_y|\psi_{n\boldsymbol{k}}\rangle}{(E_{m\boldsymbol{k}} - E_{n\boldsymbol{k}})^2}. \tag{139}$$

Here m and n denotes the band indices, $\psi_{m,n}$ and $E_{m,n}$ are the respective eigenfunctions

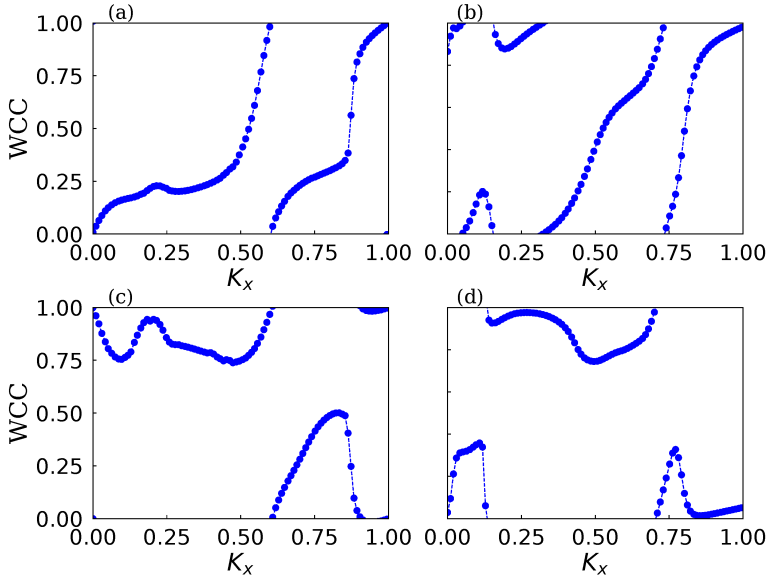

Figure 34 – Evolution of Wannier charge centers for the ultimate tensile strained 1T-CrX_2 monolayers. Plots for 1T-$CrBi_2$ with OP and IP magnetism are shown in (a) and (c), respectively. For the Sb counterpart, the corresponding plots are shown in (b) and (d), representing the OP and IP magnetism, respectively.

and eigenvalues of the corresponding bands, and f_n is the Fermi-Dirac distribution. Figures 33(c) and 33(f) show the Berry curvature for the 20% tensile-strained $CrBi_2$ and 25% $CrSb_2$, respectively. The high-intensity peaks indicate the topological nature in these systems, e.g., the points where the topological band gap is opened by SOC. For $CrSb_2$, they are located outside the high-symmetry Γ-K line, while for the Bi composition, they are located on the high-symmetry path.

As we mentioned in Chapter 3, the Chern number is calculated by integrating the Berry curvature over the entire Brillouin zone

$$C = \frac{1}{2\pi} \int_{BZ} \boldsymbol{\Omega}(\boldsymbol{k}) d^2k. \tag{140}$$

Our results show $C = 2$ for both structures, indicating a non-trivial behavior for these out-of-plane ferromagnetic monolayers. We also investigated the systems with an in-plane magnetic configuration, where the calculated Chern number was $C = 0$, indicating a trivial topology. These findings can also be verified by analyzing the evolution of Wannier charge centers, as shown in Figure 34. In the OP magnetic alignment (Fig. 34(a) for $CrBi_2$ and 34(b) for $CrSb_2$), the evolution of the WCCs shows two curves starting at zero and terminating at one, indicating $C = 2$, as previously calculated. However, the IP counterpart does not show a continuous curve from zero to one, illustrated in Figure 34(c) for the Bi composition and Figure 34(d) for Sb, resulting in a Chern number value $C = 0$.

As a consequence of the bulk-boundary correspondence, the nonzero Chern number leads to the formation of dissipationless topological edge states. Due to $C = 2$, two topological edge states are expected to connect the bands split by SOC in bulk, as shown

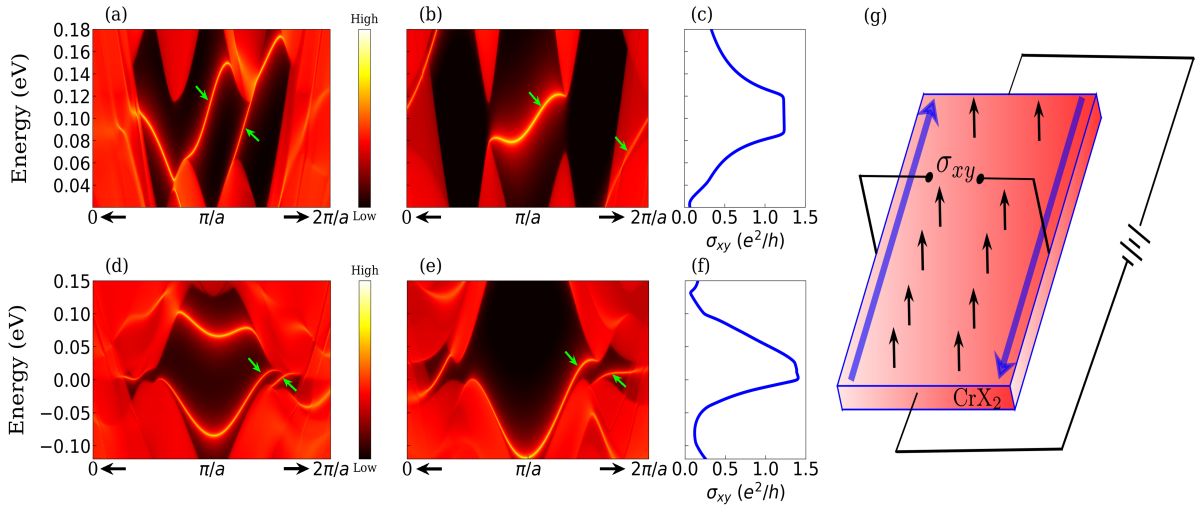

Figure 35 – Projected band structure along the edge path of 1T-$CrBi_2$ with two different biaxial tensile strain values, 19% (a) and 20% (b). In (d) and (e), the same is shown for 23.4% and 25% tensile strained 1T-$CrSb_2$. The green arrows indicate the topological edge states. The anomalous Hall conductivity for the highest tensile strained Bi and Sb compositions is shown in (c) and (d). A schematic figure of a quantum anomalous Hall device and a way to measure anomalous Hall conductivity is illustrated in (g). The blue and black arrows indicates the edge states and intrinsic OP magnetism, respectively.

in Figure 33. To investigate the effects of strain on the topological edge states, we performed nanoribbon calculations under two different strain percentages. For the 1T-$CrBi_2$ monolayer, biaxial tensile strains of 19% and 20% were applied. For the Sb composition, we considered biaxial tensile strains of 23.4% and 25%. Figures 35(a) and 35(b) show the energy-resolved dispersion for the 1T-$CrBi_2$ nanoribbon under the mentioned strain values. For the smaller strain value (Fig. 35(a)), we observe that two topological edge states connect the lower and upper bands, as indicated by green arrows. At the ultimate tensile-strained 1T-$CrBi_2$ system (Fig. 35(b)), the edge state that disperses through $\overline{k}_y = \pi/a$ point shows a behavior similar to that in the smaller strain configuration (Fig. 35(b)). However, the second state shifts in momentum direction, and its dispersion is partially hidden by the bulk states, its position is indicated by a green arrow. In 1T-$CrSb_2$ monolayer, for both values of strain, 23.4% (Fig. 35(d)) and 25% (Fig. 35(e)), the edge states, also indicated by green arrows, show similar configurations without significant changes. In the $CrSb_2$ monolayer, under 23.4% of strain, a trivial edge state arises near 0.1 eV. As the biaxial TS increases, this edge state shifts to higher energy values, beyond the range shown in Fig. 35(e).

In a quantum anomalous Hall system, one of the keys properties, particularly from the an experimental perspective [124, 36], is the anomalous Hall conductivity (AHC), which is denoted by σ_{xy}. This physical quantity is proportional to the Chern number and is

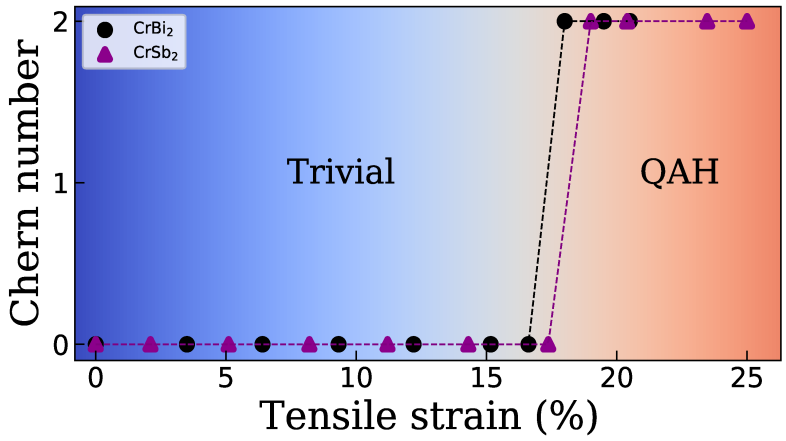

Figure 36 – Topological phase diagram for 1T-CrX_2 monolayers, with the Chern number as function of the percentage of biaxial tensile. The black symbols represent the Bi composition and purple symbols the Sb counterpart.

defined as $\sigma_{xy} = C(e^2/h)$. Figures 35(c) and 35(f) show the AHC for the 20% strained 1T-$CrBi_2$ and 25% 1T-$CrSb_2$ monolayers, respectively. In both systems, a plateau peak can be observed within the energy range from the band gap opening, with $\sigma_{xy} = 1.30\ e^2/h$ for the Bi-based system and $\sigma_{xy} = 1.45\ e^2/h$ for the Sb counterpart. A scheme illustrating how to measure the AHC is shown in Fig. 35(g). In both systems, the AHC does not reach the exact quantized value of $\sigma_{xy} = 2\ e^2/h$. The reason for this non quantized effect lies in the metallic behavior of the band structure at different momentum points, especially near to Γ point, as shown in Figs. 33(b) and 33(e). This non quantized AHC, resulting from bands that cross the topological gap at different momentum points, is also observed in other 2D quantum anomalous Hall systems [178, 188, 189, 124, 190, 191, 192].

The non trivial phase in 1T-CrX_2 monolayers arises due to biaxial tensile strain, spin-orbit coupling and with many-electron effects. As a result, a topological phase transition occurs at a given critical point. The combination of external strain effects and SOC leads to a topological phase diagram, as can be seen in Fig. 36. It is observed that the trivial behavior remains for both atomic compositions up to 15%. In the 1T-$CrBi_2$ system, the topological phase transition occurs at 17% of biaxial TS, while in the Sb-based system, the transition occurs around 18%.

We also observed topological behavior at larger values of biaxial tensile strains, where our calculations show negative phonon frequencies. In this way, with a substrate that stabilizes these imaginary phonon modes, in higher values of biaxial tensile strain, these systems can show the quantum anomalous Hall effect.

Chapter 7

Conclusion

In this work, we reported the emergence of nontrivial topological phases in different materials and systematically investigated their effects and additional properties resulting from such topological behavior. First, using first-principles calculations, we investigated the effects of a magnetic doping atom in a well-known quantum spin Hall insulator, bismuthene. The vanadium atom contributes introduces an out-of-plane magnetic moment in this system. Interestingly, we found that the topological invariant remains unchanged upon the introduction of the magnetic dopant, indicating robustness of the topologically nontrivial phase even in the presence of magnetism. This finding opens new possibilities for research in topological insulators combined with magnetism, which is highly desired due to practical applications.

The coupling between the two magnetic V impurities in bismuthene was investigated as a function of their separation distance. We analyzed the total energy variation for the impurities arranged in a line of defects, in the bulk and at one of the edges. The easy magnetization axis is oriented along the out-of-plane direction. Our results show that the bulk bismuthene supports ferromagnetic alignment between the V atoms at distances shorter than four lattice parameters. At larger distances, the magnetic coupling vanishes, indicating short-range magnetic coupling. However, when the impurities are located near one of the edges, their interaction with the topological states induces a significant change in magnetic behavior. Antiferromagnetism dominates in this new configuration, representing the ground magnetic phase for almost all inter-impurity distances. Beyond the ground magnetic phase behavior, we observed a long-range coupling with nonvanishing interactions between impurities up to 7 lattice parameters, near 30 Å. Notably, we verified two magnetic phase transitions with increasing the lattice parameter. These oscillations are attributed to the Ruderman-Kittel-Kasuya-Yosida coupling, here mediated by the topological states.

The electronic band structure reveals key distinctions between magnetic phases. While ferromagnetic alignment breaks time-reversal symmetry, inducing a band gap in the Dirac cone, the antiferromagnetic ground state (dominant across nearly all V-V distances)

maintains spin-polarized edge states with preserved Dirac crossings. In this regime, the spin configuration follows $\langle \boldsymbol{S} \rangle = \langle S_z \rangle \hat{z}$. Using an effective Hamiltonian, we elucidated the Ruderman-Kittel-Kasuya-Yosida mediated coupling mechanism. The effective model shows a good agreement with DFT results, especially for distances larger than 3 lattice parameters. At shorter distances, minor deviations are noted due to the fact that *ab initio* calculations take into account all interactions, including direct overlap orbitals. These findings establish a robust framework for investigating magnetism in topological insulators while preserving their essential properties.

One of the key themes of this thesis is a new topological class of materials, the two-dimensional Weyl semimetals. Prior to this work, in Weyl semimetals class, almost all subclasses had known potential candidate materials, except for the subclass of noncentrosymmetric Weyl semimetals with linear crossings. In this context, our study with the graphenylene-like porous structures, composed of SiGe and Ge, addresses this gap by predicting a family of two-dimensional noncentrosymmetric Weyl semimetals with a linear dispersion. The intrinsic buckling height in the z-direction drives an intrinsically broken inversion symmetry, which is crucial for the emergence of the topological phase. We found that spin-orbit coupling plays a pivotal role in the band splitting of a fourfold degenerate band crossing, which leads to the Weyl point formation. As required for the existence of two-dimensional Weyl semimetals, we verified that the C_3 symmetry protects the Weyl crossing in both atomic compositions, with a vanishing resultant chiral charge in Brillouin zone, in agreement with the fermion doubling theorem.

The properties of Weyl semimetal in a two-dimensional case show a different behavior from their three-dimensional counterpart. We studied the Weyl equation in the two-dimensional case and found key differences regarding the Berry curvature and Weyl chirality. In the two-dimensional case, the Berry curvature is given by a delta function, with its peak centered on the crossing position. The bulk-boundary correspondence in this system were verified through a nanoribbon calculation. In each system, we observe two edge states connecting the bulk Weyl points projected onto the edge with high Fermi velocity. Unlike in the quantum spin Hall case studied here, these Fermi arcs show a non-collinear spin texture, indicating that this spin channel forms an angle with the electronic motion plane. We observed that the Fermi arcs, although they lift their degeneracy, are robust against the non-vanishing magnetism originating from the dangling bonds. Similarly to the bismuthene system, this magnetism is suppressed by hydrogen edge passivation.

In the last results chapter, we have studied the emergence of quantum anomalous Hall phase in 1T-CrX_2 (X = Bi, Sb) monolayers due to the combination of different effects. We predicted a new two-dimensional magnetic material, the 1T-$CrBi_2$ monolayer, which is dynamically stable and thermodynamically stable at 300 K. We also investigated the 1T structure with Sb composition, the 1T-$CrSb_2$ monolayer. Both structures show large elasticity, with dynamic and thermodynamic stability up to 20% and 25% of biaxial ten-

sile strain for Bi and Sb compositions, respectively. These maximum strain points agrees with the strain energy curve as a function of biaxial tensile strain. Regarding the magnetic properties, our findings demonstrate that the magnetic configuration, arising from Cr *d*-orbitals, is sensitive to external effects, where the increase in biaxial tensile strain induces a magnetic phase transition from antiferromagnetic to ferromagnetic in both systems. Another sensibility of the magnetic configuration to external effects occurs in the ferromagnetic case. As the many-electron parameter increases, an easy magnetization axis transition from out-of-plane to in-plane is noted. The easy axis orientation plays a pivotal role in the topological phase. In both systems, we find above 160 K Curie temperatures using Monte Carlo simulations. These calculated temperatures are higher than the experimentally reported temperatures, representing a significant finding for experimental applications.

We observed the quantum anomalous Hall effect in these systems under the combination of biaxial tensile strain, many-electron effects, and spin-orbit coupling. This topological phase emerges at larger biaxial tensile strain values, where the ferromagnetism dominates as the ground magnetic phase. We found that the out-of-plane easy axis is crucial for the nontrivial topology, thus requiring an appropriate many-electron parameter. The strong spin-orbit coupling drives the topological phase, as evidenced by the band gap opening in Dirac cones, suggesting a topological phase transition. The topological nature was confirmed through Chern number calculations and non-vanishing Berry curvature.

We investigated the bulk-boundary correspondence in these systems by analyzing the nanoribbon band structure. Our calculations show two edge states propagating unidirectionally in both systems. We verified that the edge states in the Bi composition are sensitive to the external strain applied. In the 1T-$CrBi_2$ nanoribbon, increasing the applied strain drives the penetration of one topological state into the bulk. The anomalous Hall conductivities show a plateau in the limit of the band gap opening due to SOC. However, the higher values diverge from the quantized value of $2e^2/h$. The reason lies in the other bands that cross, at the same energy range and different momentum points, the topological band gap opened due to SOC, reducing the anomalous Hall conductivity to non-integer units. These flexible structures, exhibiting stable magnetism at high Curie temperatures and hosting quantum anomalous Hall effect, offer valuable findings for spintronic and quantum computing devices.

Bibliography

1 DONG, Z. et al. Raman characterization on two-dimensional materials-based thermoelectricity. **Molecules**, MDPI AG, v. 24, n. 1, p. 88, dez. 2018. ISSN 1420-3049. Disponível em: <http://dx.doi.org/10.3390/molecules24010088>.

2 DENG, Y. et al. Quantum anomalous hall effect in intrinsic magnetic topological insulator mnbi2te4. **Science**, American Association for the Advancement of Science (AAAS), v. 367, n. 6480, p. 895–900, fev. 2020. ISSN 1095-9203. Disponível em: <http://dx.doi.org/10.1126/science.aax8156>.

3 KUMAR, N. et al. Topological quantum materials from the viewpoint of chemistry. **Chemical Reviews**, American Chemical Society (ACS), v. 121, n. 5, p. 2780–2815, nov. 2020. ISSN 1520-6890. Disponível em: <http://dx.doi.org/10.1021/acs.chemrev.0c00732>.

4 BANSIL, A.; LIN, H.; DAS, T. Colloquium: Topological band theory. **Reviews of Modern Physics**, American Physical Society (APS), v. 88, n. 2, jun. 2016. ISSN 1539-0756. Disponível em: <http://dx.doi.org/10.1103/RevModPhys.88.021004>.

5 ANDO, Y. Topological insulator materials. **Journal of the Physical Society of Japan**, Physical Society of Japan, v. 82, n. 10, p. 102001, out. 2013. ISSN 1347-4073. Disponível em: <http://dx.doi.org/10.7566/JPSJ.82.102001>.

6 YAN, B.; FELSER, C. Topological materials: Weyl semimetals. **Annual Review of Condensed Matter Physics**, Annual Reviews, v. 8, n. Volume 8, 2017, p. 337–354, 2017. ISSN 1947-5462. Disponível em: <https://www.annualreviews.org/content/journals/10.1146/annurev-conmatphys-031016-025458>.

7 YANG, L. X. et al. Weyl semimetal phase in the non-centrosymmetric compound TaAs. **Nature Physics**, v. 11, n. 9, p. 728–732, 8 2015. Disponível em: <https://doi.org/10.1038/nphys3425>.

8 NOVOSELOV, K. S. et al. Electric field effect in atomically thin carbon films. **Science**, American Association for the Advancement of Science (AAAS), v. 306, n. 5696, p. 666–669, out. 2004. ISSN 1095-9203. Disponível em: <http://dx.doi.org/10.1126/science.1102896>.

9 GEIM, A. K.; NOVOSELOV, K. S. The rise of graphene. **Nature Materials**, Springer Science and Business Media LLC, v. 6, n. 3, p. 183–191, mar. 2007. ISSN 1476-4660. Disponível em: <http://dx.doi.org/10.1038/nmat1849>.

10 VOGT, P. et al. Silicene: Compelling experimental evidence for graphenelike two-dimensional silicon. **Phys. Rev. Lett.**, American Physical Society, v. 108, p. 155501, Apr 2012. Disponível em: <https://link.aps.org/doi/10.1103/PhysRevLett.108.155501>.

11 REIS, F. et al. Bismuthene on a sic substrate: A candidate for a high-temperature quantum spin hall material. **Science**, American Association for the Advancement of Science (AAAS), v. 357, n. 6348, p. 287–290, jul. 2017. ISSN 1095-9203. Disponível em: <http://dx.doi.org/10.1126/science.aai8142>.

12 SUN, S. et al. Epitaxial growth of ultraflat bismuthene with large topological band inversion enabled by substrate-orbital-filtering effect. **ACS Nano**, American Chemical Society (ACS), v. 16, n. 1, p. 1436–1443, dez. 2021. ISSN 1936-086X. Disponível em: <http://dx.doi.org/10.1021/acsnano.1c09592>.

13 ZHU, F.-f. et al. Epitaxial growth of two-dimensional stanene. **Nature Materials**, Springer Science and Business Media LLC, v. 14, n. 10, p. 1020–1025, ago. 2015. ISSN 1476-4660. Disponível em: <http://dx.doi.org/10.1038/nmat4384>.

14 LIU, Y. et al. Realization of strained stanene by interface engineering. **The Journal of Physical Chemistry Letters**, American Chemical Society (ACS), v. 10, n. 7, p. 1558–1565, mar. 2019. ISSN 1948-7185. Disponível em: <http://dx.doi.org/10.1021/acs.jpclett.9b00348>.

15 ZHANG, K. et al. Two dimensional hexagonal boron nitride (2d-hbn): synthesis, properties and applications. **Journal of Materials Chemistry C**, Royal Society of Chemistry (RSC), v. 5, n. 46, p. 11992–12022, 2017. ISSN 2050-7534. Disponível em: <http://dx.doi.org/10.1039/C7TC04300G>.

16 NAGUIB, M. et al. 25th anniversary article: Mxenes: A new family of two-dimensional materials. **Advanced Materials**, Wiley, v. 26, n. 7, p. 992–1005, dez. 2013. ISSN 1521-4095. Disponível em: <http://dx.doi.org/10.1002/adma.201304138>.

17 FREY, N. C. et al. Prediction of synthesis of 2d metal carbides and nitrides (mxenes) and their precursors with positive and unlabeled machine learning. **ACS Nano**, American Chemical Society (ACS), v. 13, n. 3, p. 3031–3041, mar. 2019. ISSN 1936-086X. Disponível em: <http://dx.doi.org/10.1021/acsnano.8b08014>.

18 KLEY, C. S. et al. Highly adaptable two-dimensional metal–organic coordination networks on metal surfaces. **Journal of the American Chemical Society**, American Chemical Society (ACS), v. 134, n. 14, p. 6072–6075, mar. 2012. ISSN 1520-5126. Disponível em: <http://dx.doi.org/10.1021/ja211749b>.

19 FENG, D. et al. Robust and conductive two-dimensional metal-organic frameworks with exceptionally high volumetric and areal capacitance. **Nature Energy**, Springer Science and Business Media LLC, v. 3, n. 1, p. 30–36, jan. 2018. ISSN 2058-7546. Disponível em: <http://dx.doi.org/10.1038/s41560-017-0044-5>.

20 LI, L. et al. Black phosphorus field-effect transistors. **Nature Nanotechnology**, Springer Science and Business Media LLC, v. 9, n. 5, p. 372–377, mar. 2014. ISSN 1748-3395. Disponível em: <http://dx.doi.org/10.1038/nnano.2014.35>.

21 LU, Q. et al. Realization of a two-dimensional weyl semimetal and topological fermi strings. **Nature Communications**, Springer Science and Business Media LLC, v. 15, n. 1, jul. 2024. ISSN 2041-1723. Disponível em: <http://dx.doi.org/10.1038/s41467-024-50329-6>.

22 MANZELI, S. et al. 2d transition metal dichalcogenides. **Nature Reviews Materials**, Springer Science and Business Media LLC, v. 2, n. 8, jun. 2017. ISSN 2058-8437. Disponível em: <http://dx.doi.org/10.1038/natrevmats.2017.33>.

23 MAK, K. F.; SHAN, J.; RALPH, D. C. Probing and controlling magnetic states in 2d layered magnetic materials. **Nature Reviews Physics**, Springer Science and Business Media LLC, v. 1, n. 11, p. 646–661, set. 2019. ISSN 2522-5820. Disponível em: <http://dx.doi.org/10.1038/s42254-019-0110-y>.

24 HUANG, B. et al. Layer-dependent ferromagnetism in a van der waals crystal down to the monolayer limit. **Nature**, v. 546, n. 7657, p. 270–273, 2017. Disponível em: <http://dx.doi.org/10.1038/nature22391>.

25 CHEN, W. et al. Direct observation of van der waals stacking–dependent interlayer magnetism. **Science**, American Association for the Advancement of Science (AAAS), v. 366, n. 6468, p. 983–987, nov. 2019. ISSN 1095-9203. Disponível em: <http://dx.doi.org/10.1126/science.aav1937>.

26 LU, S. et al. Controllable dimensionality conversion between 1d and 2d crcl3 magnetic nanostructures. **Nature Communications**, Springer Science and Business Media LLC, v. 14, n. 1, abr. 2023. ISSN 2041-1723. Disponível em: <http://dx.doi.org/10.1038/s41467-023-38175-4>.

27 DENG, Y. et al. Gate-tunable room-temperature ferromagnetism in two-dimensional fe3gete2. **Nature**, v. 563, n. 7729, p. 94–99, 2018. Disponível em: <http://dx.doi.org/10.1038/s41586-018-0626-9>.

28 GONG, C. et al. Discovery of intrinsic ferromagnetism in two-dimensional van der waals crystals. **Nature**, Springer Science and Business Media LLC, v. 546, n. 7657, p. 265–269, abr. 2017. ISSN 1476-4687. Disponível em: <http://dx.doi.org/10.1038/nature22060>.

29 HASAN, M. Z.; KANE, C. L. Colloquium: Topological insulators. **Reviews of Modern Physics**, American Physical Society (APS), v. 82, n. 4, p. 3045–3067, nov. 2010. ISSN 1539-0756. Disponível em: <http://dx.doi.org/10.1103/RevModPhys.82.3045>.

30 LIU, Z. et al. Quantum anomalous hall effect of dirac half-metal monolayer ticl3 with high chern number. **Europhysics Letters**, IOP Publishing, v. 136, n. 2, p. 27004, out. 2021. ISSN 1286-4854. Disponível em: <http://dx.doi.org/10.1209/0295-5075/ac23e9>.

31 KANE, C. L.; MELE, E. J. Quantum spin hall effect in graphene. **Physical Review Letters**, American Physical Society (APS), v. 95, n. 22, nov. 2005. ISSN 1079-7114. Disponível em: <http://dx.doi.org/10.1103/PhysRevLett.95.226801>.

32 KONIG, M. et al. Quantum spin hall insulator state in hgte quantum wells. **Science**, American Association for the Advancement of Science (AAAS), v. 318, n. 5851, p. 766–770, nov. 2007. ISSN 1095-9203. Disponível em: <http://dx.doi.org/10.1126/science.1148047>.

33 HASAN, M. Z. et al. Discovery of weyl fermion semimetals and topological fermi arc states. **Annual Review of Condensed Matter Physics**, Annual Reviews, v. 8, p. 289–309, 2017.

34 ARMITAGE, N. P.; MELE, E. J.; VISHWANATH, A. Weyl and dirac semimetals in three-dimensional solids. **Rev. Mod. Phys.**, American Physical Society, v. 90, p. 015001, Jan 2018. Disponível em: <https://link.aps.org/doi/10.1103/RevModPhys.90.015001>.

35 XU, S.-Y. et al. Discovery of a weyl fermion semimetal and topological fermi arcs. **Science**, v. 349, n. 6248, p. 613–617, 2015. Disponível em: <https://www.science.org/doi/abs/10.1126/science.aaa9297>.

36 CHANG, C.-Z.; LIU, C.-X.; MACDONALD, A. H. Colloquium: Quantum anomalous hall effect. **Rev. Mod. Phys.**, American Physical Society, v. 95, p. 011002, Jan 2023. Disponível em: <https://link.aps.org/doi/10.110>.

37 LIU, C.-X.; ZHANG, S.-C.; QI, X.-L. The quantum anomalous hall effect: Theory and experiment. **Annual Review of Condensed Matter Physics**, Annual Reviews, v. 7, n. 1, p. 301–321, mar. 2016. ISSN 1947-5462. Disponível em: <http://dx.doi.org/10.1146/annurev-conmatphys-031115-011417>.

38 CHANG, C.-Z. et al. Experimental observation of the quantum anomalous hall effect in a magnetic topological insulator. **Science**, American Association for the Advancement of Science (AAAS), v. 340, n. 6129, p. 167–170, abr. 2013. ISSN 1095-9203. Disponível em: <http://dx.doi.org/10.1126/science.1234414>.

39 FU, L. Topological crystalline insulators. **Phys. Rev. Lett.**, American Physical Society, v. 106, p. 106802, Mar 2011. Disponível em: <https://link.aps.org/doi/10.1103/PhysRevLett.106.106802>.

40 DZIAWA, P. et al. Topological crystalline insulator states in pb1-xsnxse. **Nature Materials**, Springer Science and Business Media LLC, v. 11, n. 12, p. 1023–1027, set. 2012. ISSN 1476-4660. Disponível em: <http://dx.doi.org/10.1038/nmat3449>.

41 WRASSE, E. O.; SCHMIDT, T. M. Prediction of two-dimensional topological crystalline insulator in pbse monolayer. **Nano Letters**, American Chemical Society (ACS), v. 14, n. 10, p. 5717–5720, set. 2014. ISSN 1530-6992. Disponível em: <http://dx.doi.org/10.1021/nl502481f>.

42 SCHINDLER, F. et al. Higher-order topological insulators. **Science Advances**, American Association for the Advancement of Science (AAAS), v. 4, n. 6, jun. 2018. ISSN 2375-2548. Disponível em: <http://dx.doi.org/10.1126/sciadv.aat0346>.

43 [ONLINE] International Year of Quantum Science and Technology. 2025. Disponível em: <https://quantum2025.org/>.

44 SUDRAJAT, H. Topological quantum materials in catalysis. **Journal of Materials Chemistry A**, Royal Society of Chemistry (RSC), v. 13, n. 9, p. 6325–6341, 2025. ISSN 2050-7496. Disponível em: <http://dx.doi.org/10.1039/D4TA08325C>.

45 KONG, X. et al. Experimental demonstration of topological catalysis for co2 electroreduction. **Journal of the American Chemical Society**, American Chemical Society (ACS), v. 146, n. 10, p. 6536–6543, fev. 2024. ISSN 1520-5126. Disponível em: <http://dx.doi.org/10.1021/jacs.3c11088>.

46 HIRSCHBERGER, M. et al. The chiral anomaly and thermopower of weyl fermions in the half-heusler gdptbi. **Nature Materials**, Springer Science and Business Media LLC, v. 15, n. 11, p. 1161–1165, jun. 2016. ISSN 1476-4660. Disponível em: <http://dx.doi.org/10.1038/nmat4684>.

47 TOKURA, Y.; YASUDA, K.; TSUKAZAKI, A. Magnetic topological insulators. **Nature Reviews Physics**, Springer Science and Business Media LLC, v. 1, n. 2, p. 126–143, jan. 2019. ISSN 2522-5820. Disponível em: <http://dx.doi.org/10.1038/s42254-018-0011-5>.

48 HILLS, R. D. Y.; KUSMARTSEVA, A.; KUSMARTSEV, F. V. Current-voltage characteristics of weyl semimetal semiconducting devices, veselago lenses, and hyperbolic dirac phase. **Phys. Rev. B**, American Physical Society, v. 95, p. 214103, Jun 2017. Disponível em: <https://link.aps.org/doi/10.1103/PhysRevB.95.214103>.

49 GIUSTINO, F. **Materials modelling using density functional theory: properties and predictions**. [S.l.]: Oxford University Press, 2014.

50 FAZZIO, A.; VIANNA, J.; CANUTO, S. **Teoria Quântica de Moléculas e Sólidos: Simulação Computacional**. [S.l.]: Editora Livraria da Física, 2004. ISBN 9788588325166.

51 SHOLL, D. S.; STECKEL, J. A. **Density Functional Theory: A Practical Introduction**. Wiley, 2009. ISBN 9780470447710. Disponível em: <http://dx.doi.org/10.1002/9780470447710>.

52 OLIVEIRA, I. **Introdução a Física do Estado Sólido**. [S.l.]: Editora Livraria da Física, 2005. ISBN 9788578614874.

53 ASHCROFT, N. W.; MERMIN, N. D. **Solid State Physics**. 1. ed. [S.l.]: Brooks Cole, 1976. ISBN 0-03-083993-9.

54 KITTEL, C. **Introduction to solid state physics**. 8th. ed. [S.l.]: John Wiley & Sons, 2004. ISBN 9780471415268.

55 MARTIN, R. M. **Electronic Structure: Basic Theory and Practical Methods**. Cambridge University Press, 2004. ISBN 9780511805769. Disponível em: <http://dx.doi.org/10.1017/CBO9780511805769>.

56 KOHN, W.; SHAM, L. J. Self-consistent equations including exchange and correlation effects. **Phys. Rev.**, American Physical Society, v. 140, p. A1133–A1138, Nov 1965. Disponível em: <https://link.aps.org/doi/10.1103/PhysRev.140.A1133>.

57 CEPERLEY, D. M.; ALDER, B. J. Ground state of the electron gas by a stochastic method. **Phys. Rev. Lett.**, American Physical Society, v. 45, p. 566–569, Aug 1980. Disponível em: <https://link.aps.org/doi/10.1103/PhysRevLett.45.566>.

58 KOHANOFF, J. **Electronic Structure Calculations for Solids and Molecules: Theory and Computational Methods**. Cambridge University Press, 2006. ISBN 9780511755613. Disponível em: <http://dx.doi.org/10.1017/CBO9780511755613>.

59 BECKE, A. D. Density-functional exchange-energy approximation with correct asymptotic behavior. **Phys. Rev. A**, American Physical Society, v. 38, p. 3098–3100, Sep 1988. Disponível em: <https://link.aps.org/doi/10.1103/PhysRevA.38.3098>.

60 LEE, C.; YANG, W.; PARR, R. G. Development of the colle-salvetti correlation-energy formula into a functional of the electron density. **Phys. Rev. B**, American Physical Society, v. 37, p. 785–789, Jan 1988. Disponível em: <https://link.aps.org/doi/10.1103/PhysRevB.37.785>.

61 PERDEW, J. P.; WANG, Y. Accurate and simple analytic representation of the electron-gas correlation energy. **Phys. Rev. B**, American Physical Society, v. 45, p. 13244–13249, Jun 1992. Disponível em: <https://link.aps.org/doi/10.1103/PhysRevB.45.13244>.

62 PERDEW, J. P.; BURKE, K.; ERNZERHOF, M. Generalized gradient approximation made simple. **Phys. Rev. Lett.**, American Physical Society, v. 77, p. 3865–3868, Oct 1996. Disponível em: <https://link.aps.org/doi/10.1103/PhysRevLett.77.3865>.

63 DUDAREV, S. L. et al. Electron-energy-loss spectra and the structural stability of nickel oxide: An lsda+u study. **Phys. Rev. B**, American Physical Society, v. 57, p. 1505–1509, Jan 1998. Disponível em: <https://link.aps.org/doi/10.1103/PhysRevB.57.1505>.

64 HIMMETOGLU, B. et al. Hubbard-corrected dft energy functionals: The lda+u description of correlated systems. **International Journal of Quantum Chemistry**, Wiley, v. 114, n. 1, p. 14–49, jul. 2013. ISSN 0020-7608. Disponível em: <http://dx.doi.org/10.1002/qua.24521>.

65 ANISIMOV, V. I.; ARYASETIAWAN, F.; LICHTENSTEIN, A. I. First-principles calculations of the electronic structure and spectra of strongly correlated systems: the lda+umethod. **Journal of Physics: Condensed Matter**, IOP Publishing, v. 9, n. 4, p. 767–808, jan. 1997. ISSN 1361-648X. Disponível em: <http://dx.doi.org/10.1088/0953-8984/9/4/002>.

66 TOLBA, S. A. et al. **Density Functional Calculations - Recent Progresses of Theory and Application**. InTech, 2018. ISBN 9781789231335. Disponível em: <http://dx.doi.org/10.5772/intechopen.72020>.

67 ROY, S. B. **Mott Insulators: Physics and applications**. IOP Publishing, 2019. ISBN 9780750315944. Disponível em: <http://dx.doi.org/10.1088/2053-2563/ab16c9>.

68 RAGHU, S. et al. Topological mott insulators. **Phys. Rev. Lett.**, American Physical Society, v. 100, p. 156401, Apr 2008. Disponível em: <https://link.aps.org/doi/10.1103/PhysRevLett.100.156401>.

69 COCOCCIONI, M.; GIRONCOLI, S. de. Linear response approach to the calculation of the effective interaction parameters in the LDA + U method. **Phys. Rev. B**, American Physical Society, v. 71, p. 035105, Jan 2005. Disponível em: <https://link.aps.org/doi/10.1103/PhysRevB.71.035105>.

70 RAJAGOPAL, A. K.; CALLAWAY, J. Inhomogeneous electron gas. **Phys. Rev. B**, American Physical Society, v. 7, p. 1912–1919, Mar 1973. Disponível em: <https://link.aps.org/doi/10.1103/PhysRevB.7.1912>.

71 BERRY, M. V. Quantal phase factors accompanying adiabatic changes. **Proceedings of the Royal Society of London. A. Mathematical and Physical Sciences**, v. 392, n. 1802, p. 45–57, 1984.

72 XIAO, D.; CHANG, M.-C.; NIU, Q. Berry phase effects on electronic properties. **Rev. Mod. Phys.**, American Physical Society, v. 82, p. 1959–2007, Jul 2010. Disponível em: <https://link.aps.org/doi/10.1103/RevModPhys.82.1959>.

73 TOMITA, A.; CHIAO, R. Y. Observation of berry's topological phase by use of an optical fiber. **Phys. Rev. Lett.**, American Physical Society, v. 57, p. 937–940, Aug 1986. Disponível em: <https://link.aps.org/doi/10.1103/PhysRevLett.57.937>.

74 TYCKO, R. Adiabatic rotational splittings and berry's phase in nuclear quadrupole resonance. **Phys. Rev. Lett.**, American Physical Society, v. 58, p. 2281–2284, Jun 1987. Disponível em: <https://link.aps.org/doi/10.1103/PhysRevLett.58.2281>.

75 THOULESS, D. J. et al. Quantized hall conductance in a two-dimensional periodic potential. **Phys. Rev. Lett.**, American Physical Society, v. 49, p. 405–408, Aug 1982. Disponível em: <https://link.aps.org/doi/10.1103/PhysRevLett.49.405>.

76 SHEN, S.-Q. **Topological Insulators: Dirac Equation in Condensed Matters**. Springer Berlin Heidelberg, 2012. ISSN 0171-1873. ISBN 9783642328589. Disponível em: <http://dx.doi.org/10.1007/978-3-642-32858-9>.

77 VANDERBILT, D. **Berry Phases in Electronic Structure Theory: Electric Polarization, Orbital Magnetization and Topological Insulators**. [S.l.]: Cambridge University Press, 2018.

78 ZHANG, H.; ZHANG, S. Topological insulators from the perspective of first-principles calculations. **physica status solidi (RRL) – Rapid Research Letters**, Wiley, v. 7, n. 1–2, p. 72–81, nov. 2012. ISSN 1862-6270. Disponível em: <http://dx.doi.org/10.1002/pssr.201206414>.

79 QI, X.-L.; ZHANG, S.-C. Topological insulators and superconductors. **Rev. Mod. Phys.**, American Physical Society, v. 83, p. 1057–1110, Oct 2011. Disponível em: <https://link.aps.org/doi/10.1103/RevModPhys.83.1057>.

80 LIU, C.-C.; JIANG, H.; YAO, Y. Low-energy effective hamiltonian involving spin-orbit coupling in silicene and two-dimensional germanium and tin. **Phys. Rev. B**, American Physical Society, v. 84, p. 195430, Nov 2011. Disponível em: <https://link.aps.org/doi/10.1103/PhysRevB.84.195430>.

81 ZHANG, H. et al. Topological insulators in bi2se3, bi2te3 and sb2te3 with a single dirac cone on the surface. **Nature Physics**, Springer Science and Business Media LLC, v. 5, n. 6, p. 438–442, maio 2009. ISSN 1745-2481. Disponível em: <http://dx.doi.org/10.1038/nphys1270>.

82 SAKURAI, J. J.; NAPOLITANO, J. **Modern Quantum Mechanics**. Cambridge University Press, 2020. ISBN 9781108473224. Disponível em: <http://dx.doi.org/10.1017/9781108587280>.

83 ARAúJO, A. L.; FERREIRA, G. J.; SCHMIDT, T. M. Suppressed topological phase transitions due to nonsymmorphism in snte stacking. **Scientific Reports**, Springer Science and Business Media LLC, v. 8, n. 1, jun. 2018. ISSN 2045-2322. Disponível em: <http://dx.doi.org/10.1038/s41598-018-27827-x>.

84 BERNEVIG, B. A.; HUGHES, T. L.; ZHANG, S.-C. Quantum spin hall effect and topological phase transition in hgte quantum wells. **Science**, American Association for the Advancement of Science (AAAS), v. 314, n. 5806, p. 1757–1761, dez. 2006. ISSN 1095-9203. Disponível em: <http://dx.doi.org/10.1126/science.1133734>.

85 HSIEH, D. et al. A topological dirac insulator in a quantum spin hall phase. **Nature**, Springer Science and Business Media LLC, v. 452, n. 7190, p. 970–974, abr. 2008. ISSN 1476-4687. Disponível em: <http://dx.doi.org/10.1038/nature06843>.

86 CHEN, Y. L. et al. Experimental realization of a three-dimensional topological insulator, bi2te3. **Science**, American Association for the Advancement of Science (AAAS), v. 325, n. 5937, p. 178–181, jul. 2009. ISSN 1095-9203. Disponível em: <http://dx.doi.org/10.1126/science.1173034>.

87 MOORE, J. E. The birth of topological insulators. **Nature**, Springer Science and Business Media LLC, v. 464, n. 7286, p. 194–198, mar. 2010. ISSN 1476-4687. Disponível em: <http://dx.doi.org/10.1038/nature08916>.

88 WEYL, H. Gravitation and the electron. **Proceedings of the National Academy of Sciences**, Proceedings of the National Academy of Sciences, v. 15, n. 4, p. 323–334, abr. 1929. ISSN 1091-6490. Disponível em: <http://dx.doi.org/10.1073/pnas.15.4.323>.

89 GREINER, W. **Relativistic Quantum Mechanics. Wave Equations**. Springer Berlin Heidelberg, 2000. ISBN 9783662042755. Disponível em: <http://dx.doi.org/10.1007/978-3-662-04275-5>.

90 YANG, S. A. Dirac and weyl materials: Fundamental aspects and some spintronics applications. **SPIN**, v. 06, n. 02, p. 1640003, 2016. Disponível em: <https://doi.org/10.1142/S2010324716400038>.

91 AHMAD, A.; K, G. V.; SHARMA, G. Geometry, anomaly, topology, and transport in weyl fermions. **Journal of Physics: Condensed Matter**, IOP Publishing, v. 37, n. 4, p. 043001, nov. 2024. ISSN 1361-648X. Disponível em: <http://dx.doi.org/10.1088/1361-648X/ad8ab9>.

92 NIELSEN, H.; NINOMIYA, M. The adler-bell-jackiw anomaly and weyl fermions in a crystal. **Physics Letters B**, Elsevier BV, v. 130, n. 6, p. 389–396, nov. 1983. ISSN 0370-2693. Disponível em: <http://dx.doi.org/10.1016/0370-2693(83)91529-0>.

93 XU, S.-Y. et al. Experimental discovery of a topological weyl semimetal state in tap. **Science Advances**, v. 1, n. 10, p. e1501092, 2015.

94 XU, S.-Y. et al. Discovery of a weyl fermion state with fermi arcs in niobium arsenide. **Nature Physics**, Springer Science and Business Media LLC, v. 11, n. 9, p. 748–754, aug 2015.

95 XU, S.-Y. et al. Experimental discovery of a topological weyl semimetal state in tap. **Science Advances**, v. 1, n. 10, p. e1501092, 2015. Disponível em: <https://www.science.org/doi/abs/10.1126/sciadv.1501092>.

96 LV, B. Q. et al. Observation of fermi-arc spin texture in taas. **Phys. Rev. Lett.**, American Physical Society, v. 115, p. 217601, Nov 2015. Disponível em: <https://link.aps.org/doi/10.1103/PhysRevLett.115.217601>.

97 LIU, Z. K. et al. Evolution of the fermi surface of weyl semimetals in the transition metal pnictide family. **Nature Materials**, Springer Science and Business Media LLC, v. 15, n. 1, p. 27–31, nov. 2015. ISSN 1476-4660. Disponível em: <http://dx.doi.org/10.1038/nmat4457>.

98 SUN, Y.; WU, S.-C.; YAN, B. Topological surface states and fermi arcs of the noncentrosymmetric weyl semimetals taas, tap, nbas, and nbp. **Phys. Rev. B**, American Physical Society, v. 92, p. 115428, Sep 2015. Disponível em: <https://link.aps.org/doi/10.1103/PhysRevB.92.115428>.

99 JIANG, J. et al. Signature of type-ii weyl semimetal phase in mote2. **Nature Communications**, Springer Science and Business Media LLC, v. 8, n. 1, jan. 2017. ISSN 2041-1723. Disponível em: <http://dx.doi.org/10.1038/ncomms13973>.

100 WANG, Z. et al. $mote_2$: A type-ii weyl topological metal. **Phys. Rev. Lett.**, American Physical Society, v. 117, p. 056805, Jul 2016. Disponível em: <https://link.aps.org/doi/10.1103/PhysRevLett.117.056805>.

101 TAMAI, A. et al. Fermi arcs and their topological character in the candidate type-ii weyl semimetal mote 2. **Physical Review X**, APS, v. 6, n. 3, p. 031021, 2016. Disponível em: <https://link.aps.org/doi/10.1103/PhysRevX.6.031021>.

102 WU, Y. et al. Observation of fermi arcs in the type-ii weyl semimetal candidate wte_2. **Phys. Rev. B**, American Physical Society, v. 94, p. 121113, Sep 2016. Disponível em: <https://link.aps.org/doi/10.1103/PhysRevB.94.121113>.

103 WANG, C. et al. Observation of fermi arc and its connection with bulk states in the candidate type-ii weyl semimetal wte_2. **Phys. Rev. B**, American Physical Society, v. 94, p. 241119, Dec 2016. Disponível em: <https://link.aps.org/doi/10.1103/PhysRevB.94.241119>.

104 LIU, D. F. et al. Magnetic weyl semimetal phase in a kagomé crystal. **Science**, American Association for the Advancement of Science (AAAS), v. 365, n. 6459, p. 1282–1285, set. 2019. ISSN 1095-9203. Disponível em: <http://dx.doi.org/10.1126/science.aav2873>.

105 MORALI, N. et al. Fermi-arc diversity on surface terminations of the magnetic weyl semimetal co3sn2s2. **Science**, American Association for the Advancement of Science (AAAS), v. 365, n. 6459, p. 1286–1291, set. 2019. ISSN 1095-9203. Disponível em: <http://dx.doi.org/10.1126/science.aav2334>.

106 SCHRUNK, B. et al. Emergence of fermi arcs due to magnetic splitting in an antiferromagnet. **Nature**, Springer Science and Business Media LLC, v. 603, n. 7902, p. 610–615, mar. 2022. ISSN 1476-4687. Disponível em: <http://dx.doi.org/10.1038/s41586-022-04412-x>.

107 SCHRöTER, N. B. M. et al. Weyl fermions, fermi arcs, and minority-spin carriers in ferromagnetic cos_2. **Science Advances**, American Association for the Advancement of Science (AAAS), v. 6, n. 51, dez. 2020. ISSN 2375-2548. Disponível em: <http://dx.doi.org/10.1126/sciadv.abd5000>.

108 SHI, Y. et al. Mnnbr monolayer: A high-temperature ferromagnetic half-metal with type-ii weyl fermions. **physica status solidi (RRL) – Rapid Research Letters**, Wiley, v. 15, n. 7, maio 2021. ISSN 1862-6270. Disponível em: <http://dx.doi.org/10.1002/pssr.202100115>.

109 MENG, W. et al. Two-dimensional weyl semimetal with coexisting fully spin-polarized type-i and type-ii weyl points. **Applied Surface Science**, Elsevier BV, v. 540, p. 148318, fev. 2021. ISSN 0169-4332. Disponível em: <http://dx.doi.org/10.1016/j.apsusc.2020.148318>.

110 LI, G.-G. et al. Two-dimensional weyl semi-half-metallic nics3 with a band structure controllable by the direction of magnetization. **Phys. Chem. Chem. Phys.**, The Royal Society of Chemistry, v. 23, p. 12068–12074, 2021. Disponível em: <http://dx.doi.org/10.1039/D1CP00812A>.

111 HE, T. et al. Ferromagnetic hybrid nodal loop and switchable type-i and type-ii weyl fermions in two dimensions. **Phys. Rev. B**, American Physical Society, v. 102, p. 075133, Aug 2020. Disponível em: <https://link.aps.org/doi/10.1103/PhysRevB.102.075133>.

112 JIA, T. et al. Weyl fermions in vi3 monolayer. **Frontiers in Chemistry**, v. 8, 2020. ISSN 2296-2646. Disponível em: <http://dx.doi.org/10.3389/fchem.2020.00722>.

113 WEI, X.-P. et al. Ferromagnetic weyl semimetals and quantum anomalous hall effect in 2d half-metallic mn2nt2. **Physica E: Low-dimensional Systems and Nanostructures**, v. 140, p. 115164, 2022. ISSN 1386-9477. Disponível em: <https://www.sciencedirect.com/science/article/pii/S1386947722000297>.

114 YOU, J.-Y. et al. Two-dimensional weyl half-semimetal and tunable quantum anomalous hall effect. **Phys. Rev. B**, American Physical Society, v. 100, p. 064408, Aug 2019. Disponível em: <https://link.aps.org/doi/10.1103/PhysRevB.100.064408>.

115 ZOU, X. et al. Antiferromagnetic topological crystalline insulator and mixed weyl semimetal in two-dimensional npas monolayer. **New Journal of Physics**, IOP Publishing, v. 23, n. 12, p. 123018, dec 2021. Disponível em: <https://dx.doi.org/10.1088/1367-2630/ac3cf5>.

116 ZHAO, X. et al. Two-dimensional quadratic double weyl semimetal. **Phys. Rev. Res.**, American Physical Society, v. 4, p. 043183, Dec 2022. Disponível em: <https://link.aps.org/doi/10.1103/PhysRevResearch.4.043183>.

117 LI, C. et al. Double-weyl fermions in two-dimensional ferromagnetic materials. **Journal of Alloys and Compounds**, Elsevier BV, v. 1010, p. 178059, jan. 2025. ISSN 0925-8388. Disponível em: <http://dx.doi.org/10.1016/j.jallcom.2024.178059>.

118 LOPES, E. V. C. et al. Noncentrosymmetric two-dimensional weyl semimetals in porous si/ge structures. **Journal of Physics: Condensed Matter**, IOP Publishing, v. 36, n. 18, p. 185701, fev. 2024. ISSN 1361-648X. Disponível em: <http://dx.doi.org/10.1088/1361-648X/ad1e09>.

119 CAI, Z. et al. Evidence for two-dimensional weyl fermions in air-stable monolayer ptte1.75. **Nano Letters**, American Chemical Society (ACS), v. 24, n. 33, p. 10237–10243, ago. 2024. ISSN 1530-6992. Disponível em: <http://dx.doi.org/10.1021/acs.nanolett.4c02580>.

120 HALL, E. H. On a new action of the magnet on electric currents. **American Journal of Mathematics**, JSTOR, v. 2, n. 3, p. 287, set. 1879. ISSN 0002-9327. Disponível em: <http://dx.doi.org/10.2307/2369245>.

121 KLITZING, K. v.; DORDA, G.; PEPPER, M. New method for high-accuracy determination of the fine-structure constant based on quantized hall resistance. **Phys. Rev. Lett.**, American Physical Society, v. 45, p. 494–497, Aug 1980. Disponível em: <https://link.aps.org/doi/10.1103/PhysRevLett.45.494>.

122 SCHOPFER, F.; POIRIER, W. Testing universality of the quantum hall effect by means of the wheatstone bridge. **Journal of Applied Physics**, AIP Publishing, v. 102, n. 5, set. 2007. ISSN 1089-7550. Disponível em: <http://dx.doi.org/10.1063/1.2776371>.

123 HALL, E. Xviii. on the "rotational coefficient" in nickel and cobalt. **The London, Edinburgh, and Dublin Philosophical Magazine and Journal of Science**, Informa UK Limited, v. 12, n. 74, p. 157–172, set. 1881. ISSN 1941-5990. Disponível em: <http://dx.doi.org/10.1080/14786448108627086>.

124 NAGAOSA, N. et al. Anomalous hall effect. **Rev. Mod. Phys.**, American Physical Society, v. 82, p. 1539–1592, May 2010. Disponível em: <https://link.aps.org/doi/10.1103/RevModPhys.82.1539>.

125 ZHANG, H. et al. High-temperature and multichannel quantum anomalous hall effect in pristine and alkali–metal-doped crbr3 monolayers. **Nanoscale**, The Royal Society of Chemistry, v. 12, p. 13964–13972, 2020. Disponível em: <http://dx.doi.org/10.1039/D0NR02829K>.

126 BAO, H. et al. Quantum anomalous hall effect with high chern numbers in functionalized square-octagon sb monolayers. **2D Materials**, IOP Publishing, v. 10, n. 3, p. 035004, apr 2023. Disponível em: <https://dx.doi.org/10.1088/2053-1583/accbd0>.

127 KARPLUS, R.; LUTTINGER, J. M. Hall effect in ferromagnetics. **Phys. Rev.**, American Physical Society, v. 95, p. 1154–1160, Sep 1954. Disponível em: <https://link.aps.org/doi/10.1103/PhysRev.95.1154>.

128 YIN, X. et al. Alkali metal-doped two-dimensional janus cr2br3i3 monolayers with the quantum anomalous hall effect. **J. Mater. Chem. C**, The Royal Society of Chemistry, v. 12, p. 5442–5450, 2024. Disponível em: <http://dx.doi.org/10.1039/D4TC00088A>.

129 WU, S.-C.; SHAN, G.; YAN, B. Prediction of near-room-temperature quantum anomalous hall effect on honeycomb materials. **Phys. Rev. Lett.**, American Physical Society, v. 113, p. 256401, Dec 2014. Disponível em: <https://link.aps.org/doi/10.1103/PhysRevLett.113.256401>.

130 LIMA, F. Crasto de; FERREIRA, G. J.; MIWA, R. H. Quantum anomalous hall effect in metal-bis(dithiolene), magnetic properties, doping and interfacing graphene. **Phys. Chem. Chem. Phys.**, The Royal Society of Chemistry, v. 20, p. 22652–22659, 2018.

131 WANG, Z. F.; LIU, Z.; LIU, F. Quantum anomalous hall effect in 2d organic topological insulators. **Phys. Rev. Lett.**, American Physical Society, v. 110, p. 196801, May 2013. Disponível em: <https://link.aps.org/doi/10.1103/PhysRevLett.110.196801>.

132 ZHANG, X. et al. Time-reversal symmetry breaking weyl semimetal and tunable quantum anomalous hall effect in a two-dimensional metal-organic framework. **Phys. Rev. B**, American Physical Society, v. 108, p. 054404, Aug 2023. Disponível em: <https://link.aps.org/doi/10.1103/PhysRevB.108.054404>.

133 LIU, Z. et al. Intrinsic quantum anomalous hall effect with in-plane magnetization: Searching rule and material prediction. **Physical Review Letters**, American Physical Society (APS), v. 121, n. 24, dez. 2018. ISSN 1079-7114. Disponível em: <http://dx.doi.org/10.1103/PhysRevLett.121.246401>.

134 JIA, K. et al. First-principles study reveals an electronic correlation effect on the topological and electronic properties of janus ruclf monolayers: Implications for spintronics and valleytronics applications. **ACS Applied Nano Materials**, v. 6, n. 15, p. 14003–14010, 2023.

135 GUO, S.-D.; MU, W.-Q.; LIU, B.-G. Valley-polarized quantum anomalous hall insulator in monolayer rubr2. **2D Materials**, IOP Publishing, v. 9, n. 3, p. 035011, maio 2022. ISSN 2053-1583. Disponível em: <http://dx.doi.org/10.1088/2053-1583/ac687f>.

136 CHANG, C.-Z. et al. High-precision realization of robust quantum anomalous hall state in a hard ferromagnetic topological insulator. **Nature Materials**, Springer Science and Business Media LLC, v. 14, n. 5, p. 473–477, mar. 2015. ISSN 1476-4660. Disponível em: <http://dx.doi.org/10.1038/nmat4204>.

137 LI, J. et al. Magnetically controllable topological quantum phase transitions in the antiferromagnetic topological insulator $mnbi_2te_4$. **Phys. Rev. B**, American Physical Society, v. 100, p. 121103, Sep 2019. Disponível em: <https://link.aps.org/doi/10.1103/PhysRevB.100.121103>.

138 LOPES, E. V. C.; VERNEK, E.; SCHMIDT, T. M. Rkky interactions mediated by topological states in transition metal doped bismuthene. **Journal of Applied Physics**, AIP Publishing, v. 133, n. 11, mar. 2023. ISSN 1089-7550. Disponível em: <http://dx.doi.org/10.1063/5.0140027>.

139 ZARE, M.; PARHIZGAR, F.; ASGARI, R. Topological phase and edge states dependence of the rkky interaction in zigzag silicene nanoribbon. **Physical Review B**, American Physical Society (APS), v. 94, n. 4, jul. 2016. ISSN 2469-9969. Disponível em: <http://dx.doi.org/10.1103/PhysRevB.94.045443>.

140 KIM, J.; JHI, S.-H. Magnetic phase transition in fe-doped topological insulator Bi_2Se_3. **Phys. Rev. B**, American Physical Society, v. 92, p. 104405, Sep 2015. Disponível em: <https://link.aps.org/doi/10.1103/PhysRevB.92.104405>.

141 MA, Y. et al. Room temperature ferromagnetism in teflon due to carbon dangling bonds. **Nature Communications**, Springer Science and Business Media LLC, v. 3, n. 1, mar. 2012. ISSN 2041-1723. Disponível em: <http://dx.doi.org/10.1038/ncomms1689>.

142 VALLA, T. et al. Photoemission spectroscopy of magnetic and nonmagnetic impurities on the surface of the bi_2se_3 topological insulator. **Phys. Rev. Lett.**, American Physical Society, v. 108, p. 117601, Mar 2012. Disponível em: <https://link.aps.org/doi/10.1103/PhysRevLett.108.117601>.

143 SCHOLZ, M. R. et al. Tolerance of topological surface states towards magnetic moments: Fe on bi_2se_3. **Phys. Rev. Lett.**, American Physical Society, v. 108, p. 256810, Jun 2012. Disponível em: <https://link.aps.org/doi/10.1103/PhysRevLett.108.256810>.

144 SICHAU, J. et al. Resonance microwave measurements of an intrinsic spin-orbit coupling gap in graphene: A possible indication of a topological state. **Phys. Rev. Lett.**, American Physical Society, v. 122, p. 046403, Feb 2019. Disponível em: <https://link.aps.org/doi/10.1103/PhysRevLett.122.046403>.

145 WADA, M. et al. Localized edge states in two-dimensional topological insulators: Ultrathin bi films. **Phys. Rev. B**, American Physical Society, v. 83, p. 121310, Mar 2011. Disponível em: <https://link.aps.org/doi/10.1103/PhysRevB.83.121310>.

146 WANG, Z. F.; CHEN, L.; LIU, F. Tuning topological edge states of bi(111) bilayer film by edge adsorption. **Nano Letters**, American Chemical Society (ACS), v. 14, n. 5, p. 2879–2883, may 2014. ISSN 1530-6992. Disponível em: <http://dx.doi.org/10.1021/nl5009212>.

147 FU, L.; KANE, C. L. Topological insulators with inversion symmetry. **Phys. Rev. B**, American Physical Society, v. 76, p. 045302, Jul 2007. Disponível em: <https://link.aps.org/doi/10.1103/PhysRevB.76.045302>.

148 SOLUYANOV, A. A.; VANDERBILT, D. Computing topological invariants without inversion symmetry. **Physical Review B**, American Physical Society (APS), v. 83, n. 23, p. 235401, jun 2011.

149 GRESCH, D. et al. Z2pack: Numerical implementation of hybrid wannier centers for identifying topological materials. **Physical Review B**, American Physical Society (APS), v. 95, n. 7, p. 075146, feb 2017.

150 NAUMOV, I. I.; DEV, P. Coexistence of quantum spin hall and magnetic states in zigzag bismuth nanoribbons. **Applied Physics Letters**, AIP Publishing, v. 123, n. 9, ago. 2023. ISSN 1077-3118. Disponível em: <http://dx.doi.org/10.1063/5.0160159>.

151 NAUMOV, I. I.; DEV, P. One-dimensional magnetism and rashba-like effects in zigzag bismuth nanoribbons. **Phys. Rev. Mater.**, American Physical Society, v. 7, p. 026204, Feb 2023. Disponível em: <https://link.aps.org/doi/10.1103/PhysRevMaterials.7.026204>.

152 QI, M.; DAI, S.; WU, P. Prediction of electronic and magnetic properties in 3d-transition-metal x-doped bismuthene (x = v, cr, mn and fe). **Applied Surface Science**, Elsevier BV, v. 486, p. 58–64, ago. 2019. ISSN 0169-4332. Disponível em: <http://dx.doi.org/10.1016/j.apsusc.2019.05.002>.

153 KIM, J. et al. Understanding the giant enhancement of exchange interaction in bi_2se_3−EuS heterostructures. **Physical Review Letters**, American Physical Society (APS), v. 119, n. 2, jul. 2017. ISSN 1079-7114. Disponível em: <http://dx.doi.org/10.1103/PhysRevLett.119.027201>.

154 LI, Z. L. et al. Strong single-ion anisotropy and anisotropic interactions of magnetic adatoms induced by topological surface states. **Physical Review B**, American Physical Society (APS), v. 85, n. 5, fev. 2012. ISSN 1550-235X. Disponível em: <http://dx.doi.org/10.1103/PhysRevB.85.054426>.

155 KIM, J.; WU, R. Manipulating the one-dimensional topological edge state of bi bilayer nanoribbons via magnetic orientation and electric field. **Phys. Rev. B**, American Physical Society, v. 97, p. 115151, Mar 2018. Disponível em: <https://link.aps.org/doi/10.1103/PhysRevB.97.115151>.

156 BYCHKOV, Y. A.; RASHBA, E. I. Oscillatory effects and the magnetic susceptibility of carriers in inversion layers. **Journal of Physics C: Solid State Physics**, v. 17, n. 33, p. 6039, nov 1984. Disponível em: <https://dx.doi.org/10.1088/0022-3719/17/33/015>.

157 NOLTING, W.; RAMAKANTH, A. **Quantum Theory of Magnetism**. Springer Berlin Heidelberg, 2009. ISBN 9783540854166. Disponível em: <http://dx.doi.org/10.1007/978-3-540-85416-6>.

158 PAVARINI, E.; KOCH, E.; COLEMAN, P. (Ed.). **Many-Body Physics: From Kondo to Hubbard**, v. 5 de **Schriften des Forschungszentrums Jülich. Reihe modeling and simulation**, (Schriften des Forschungszentrums Jülich. Reihe modeling and simulation, v. 5). Autumn School on Correlated Electrons, Jülich (Germany), 21 Sep 2015 - 25 Sep 2015, Jülich: Forschungszentrum Jülich GmbH Zentralbibliothek, Verlag, 2015. getr. Zählung p. ISBN 978-3-95806-074-6. Disponível em: <https://juser.fz-juelich.de/record/205123>.

159 SILVA, J. F.; VERNEK, E. Modified exchange interaction between magnetic impurities in spin–orbit coupled quantum wires. **Journal of Physics: Condensed Matter**, IOP Publishing, v. 31, n. 13, p. 135802, feb 2019. Disponível em: <https://doi.org/10.1088/1361-648x/ab0076>.

160 KONDO, J. Resistance minimum in dilute magnetic alloys. **Progress of Theoretical Physics**, v. 32, n. 1, p. 37–49, 07 1964. ISSN 0033-068X. Disponível em: <https://doi.org/10.1143/PTP.32.37>.

161 BRUNETTO, G. et al. Nonzero gap two-dimensional carbon allotrope from porous graphene. **The Journal of Physical Chemistry C**, American Chemical Society (ACS), v. 116, n. 23, p. 12810–12813, jun. 2012. ISSN 1932-7455. Disponível em: <http://dx.doi.org/10.1021/jp211300n>.

162 SONG, Q. et al. Graphenylene, a unique two-dimensional carbon network with nondelocalized cyclohexatriene units. **J. Mater. Chem. C**, Royal Society of Chemistry (RSC), v. 1, n. 1, p. 38–41, 2013. ISSN 2050-7534. Disponível em: <http://dx.doi.org/10.1039/C2TC00006G>.

163 DU, Q.-S. et al. A new type of two-dimensional carbon crystal prepared from 1, 3, 5-trihydroxybenzene. **Scientific Reports**, Springer Science and Business Media LLC, v. 7, n. 1, jan. 2017. ISSN 2045-2322. Disponível em: <http://dx.doi.org/10.1038/srep40796>.

164 KREMER, L. F.; BAIERLE, R. J. Stability, electronic and optical properties of group iv graphenylene-like materials. an ab initio investigation. **Diamond and Related Materials**, Elsevier BV, v. 141, p. 110689, jan. 2024. ISSN 0925-9635. Disponível em: <http://dx.doi.org/10.1016/j.diamond.2023.110689>.

165 GUO, Y. et al. Two-dimensional tunable dirac/weyl semimetal in non-abelian gauge field. **Scientific Reports**, Springer Science and Business Media LLC, v. 9, n. 1, dec 2019.

166 FANG, C. et al. Multi-weyl topological semimetals stabilized by point group symmetry. **Physical Review Letters**, American Physical Society (APS), v. 108, n. 26, jun. 2012. ISSN 1079-7114. Disponível em: <http://dx.doi.org/10.1103/PhysRevLett.108.266802>.

167 CHANG, G. et al. Topological quantum properties of chiral crystals. **Nature Materials**, Springer Science and Business Media LLC, v. 17, n. 11, p. 978–985, out. 2018. ISSN 1476-4660. Disponível em: <http://dx.doi.org/10.1038/s41563-018-0169-3>.

168 LIU, J.; FANG, C.; FU, L. Tunableweyl fermions and fermi arcs in magnetized topological crystalline insulators. **Chinese Physics B**, IOP Publishing, v. 28, n. 4, p. 047301, abr. 2019. ISSN 2058-3834. Disponível em: <http://dx.doi.org/10.1088/1674-1056/28/4/047301>.

169 XU, S.-Y. et al. Spin polarization and texture of the fermi arcs in the weyl fermion semimetal taas. **Phys. Rev. Lett.**, American Physical Society, v. 116, p. 096801, Mar 2016. Disponível em: <https://link.aps.org/doi/10.1103/PhysRevLett.116.096801>.

170 LI, Y. et al. Dirac fermions in strongly bound graphene systems. **Phys. Rev. Lett.**, American Physical Society, v. 109, p. 206802, Nov 2012. Disponível em: <https://link.aps.org/doi/10.1103/PhysRevLett.109.206802>.

171 HWANG, C. et al. Fermi velocity engineering in graphene by substrate modification. **Scientific Reports**, Springer Science and Business Media LLC, v. 2, n. 1, ago. 2012. ISSN 2045-2322. Disponível em: <http://dx.doi.org/10.1038/srep00590>.

172 ENGEL, H.-A.; RECHER, P.; LOSS, D. Electron spins in quantum dots for spintronics and quantum computation. **Solid State Communications**, Elsevier BV, v. 119, n. 4–5, p. 229–236, jul. 2001. ISSN 0038-1098. Disponível em: <http://dx.doi.org/10.1016/S0038-1098(01)00110-7>.

173 LOPES, E. V. C.; SCHMIDT, T. M. Tuning quantum anomalous hall effect in ferromagnetic 1t-crx2 (x = bi, sb) monolayers. **Applied Physics Letters**, AIP Publishing, v. 125, n. 24, dez. 2024. ISSN 1077-3118. Disponível em: <http://dx.doi.org/10.1063/5.0244117>.

174 SHENG, K.; WANG, Z.-Y. Ab initio discovery of group iv–v monolayers with superlative mechanical, electronic, and transport properties. **Crystal Growth & Design**, v. 24, n. 15, p. 6400–6412, 2024. Disponível em: <https://doi.org/10.1021/acs.cgd.4c00643>.

175 WANG, Y. et al. Intrinsic ferromagnetism in two-dimensional 1t-mx2 monolayers with tunable magnetocrystalline anisotropy. **Phys. Chem. Chem. Phys.**, The Royal Society of Chemistry, v. 25, p. 30636–30643, 2023.

176 ANDERSON, P. W. Antiferromagnetism. theory of superexchange interaction. **Phys. Rev.**, American Physical Society, v. 79, p. 350–356, Jul 1950. Disponível em: <https://link.aps.org/doi/10.1103/PhysRev.79.350>.

177 MOGULKOC, A.; MODARRESI, M.; RUDENKO, A. N. Two-dimensional chromium pnictides Crx(x=P, As, Sb): Half-metallic ferromagnets with high curie temperature. **Phys. Rev. B**, American Physical Society, v. 102, p. 024441, Jul 2020. Disponível em: <https://link.aps.org/doi/10.1103/PhysRevB.102.024441>.

178 MOGULKOC, A.; MODARRESI, M.; RUDENKO, A. Two-dimensional chromium bismuthate: A room-temperature ising ferromagnet with tunable magneto-optical response. **Phys. Rev. Appl.**, American Physical Society, v. 15, p. 064053, Jun 2021.

179 KUHN, G. et al. Electronic structure and magnetic properties of $crsb_2$ and $fesb_2$ investigated via ab initio calculations. **Phys. Rev. B**, American Physical Society, v. 87, p. 085113, Feb 2013. Disponível em: <https://link.aps.org/doi/10.1103/PhysRevB.87.085113>.

180 LIU, Y. et al. Structural, electronic, and magnetic properties of $crte_2$. **Phys. Rev. Mater.**, American Physical Society, v. 6, p. 084004, Aug 2022. Disponível em: <https://link.aps.org/doi/10.1103/PhysRevMaterials.6.084004>.

181 ZHU, H. et al. Insight into strain and electronic correlation dependent magnetism in monolayer $1t-Crte_2$. **Phys. Rev. B**, American Physical Society, v. 108, p. 144404, Oct 2023. Disponível em: <https://link.aps.org/doi/10.1103/PhysRevB.108.144404>.

182 SOUZA, P. H. et al. Magnetic anisotropy energies and metal-insulator transitions in monolayers of $\alpha-rucl_3$ and $oscl_3$ on graphene. **Phys. Rev. B**, American Physical Society, v. 106, p. 155118, Oct 2022. Disponível em: <https://link.aps.org/doi/10.1103/PhysRevB.106.155118>.

183 BADER, S.; PARKIN, S. Spintronics. **Annual Review of Condensed Matter Physics**, Annual Reviews, v. 1, n. 1, p. 71–88, ago. 2010. ISSN 1947-5462. Disponível em: <http://dx.doi.org/10.1146/annurev-conmatphys-070909-104123>.

184 LI, X.; WU, X. Two-dimensional monolayer designs for spintronics applications. **WIREs Computational Molecular Science**, v. 6, n. 4, p. 441–455, 2016. Disponível em: <https://wires.onlinelibrary.wiley.com/doi/abs/10.1002/wcms.1259>.

185 LIU, Z.; LIU, J.; ZHAO, J. Yn2 monolayer: Novel p-state dirac half metal for high-speed spintronics. **Nano Research**, Tsinghua University Press, v. 10, n. 6, p. 1972–1979, jan. 2017. ISSN 1998-0000. Disponível em: <http://dx.doi.org/10.1007/s12274-016-1384-3>.

186 ARES, P. et al. Recent progress on antimonene: A new bidimensional material. **Advanced Materials**, v. 30, n. 2, p. 1703771, 2018. Disponível em: <https://onlinelibrary.wiley.com/doi/abs/10.1002/adma.201703771>.

187 WANG, X. et al. Topological phases in double layers of bismuthene and antimonene. **Nanotechnology**, IOP Publishing, v. 28, n. 39, p. 395706, sep 2017. Disponível em: <https://dx.doi.org/10.1088/1361-6528/aa825f>.

188 HUANG, A. et al. Topological phase and quantum anomalous hall effect in ferromagnetic transition-metal dichalcogenides monolayer 1t vse2. **Nanomaterials**, MDPI AG, v. 11, n. 8, p. 1998, ago. 2021. ISSN 2079-4991.

189 ZHU, M. et al. Theoretical model of spintronic device based on tunable anomalous Hall conductivity of monolayer CrI3. **Applied Physics Letters**, v. 116, n. 2, p. 022404, 01 2020. ISSN 0003-6951. Disponível em: <https://doi.org/10.1063/1.5132356>.

190 ZHOU, J. et al. Intrinsic quantum spin hall and anomalous hall effects in h-sb/bi epitaxial growth on a ferromagnetic mno2 thin film. **Nanoscale**, The Royal Society of Chemistry, v. 8, p. 11202–11209, 2016.

191 ZAITSEV, N. L. et al. Interplay between exchange-split dirac and rashba-type surface states at the $mnbi_2te_4$/BiTeI interface. **Phys. Rev. B**, American Physical Society, v. 107, p. 045402, Jan 2023. Disponível em: <https://link.aps.org/doi/10.1103/PhysRevB.107.045402>.

192 LI, D. et al. Switchable in-plane anomalous hall effect by magnetization orientation in monolayer $mn_3si_2te_6$. **Phys. Rev. B**, American Physical Society, v. 109, p. 155153, Apr 2024. Disponível em: <https://link.aps.org/doi/10.1103/PhysRevB.109.155153>.

193 KRESSE, G.; HAFNER, J. *abinitio* molecular dynamics for liquid metals. **Physical Review B**, American Physical Society (APS), v. 47, n. 1, p. 558–561, jan 1993.

194 KRESSE, G.; FURTHMÜLLER, J. Efficient iterative schemes for ab initio total-energy calculations using a plane-wave basis set. **Phys. Rev. B**, American Physical Society, v. 54, p. 11169–11186, Oct 1996.

195 MOSTOFI, A. A. et al. An updated version of wannier90: A tool for obtaining maximally-localised wannier functions. **Computer Physics Communications**, v. 185, n. 8, p. 2309–2310, 2014. ISSN 0010-4655. Disponível em: <https://www.sciencedirect.com/science/article/pii/S001046551400157X>.

196 WU, Q. et al. Wanniertools : An open-source software package for novel topological materials. **Computer Physics Communications**, v. 224, p. 405 – 416, 2018. ISSN 0010-4655. Disponível em: <http://www.sciencedirect.com/science/article/pii/S0010465517303442>.

197 WANG, V. et al. Vaspkit: A user-friendly interface facilitating high-throughput computing and analysis using vasp code. **Computer Physics Communications**, v. 267, p. 108033, 2021. ISSN 0010-4655. Disponível em: <https://www.sciencedirect.com/science/article/pii/S0010465521001454>.

198 TOGO, A. First-principles phonon calculations with phonopy and phono3py. **J. Phys. Soc. Jpn.**, v. 92, n. 1, p. 012001, 2023.

199 TOGO, A. et al. Implementation strategies in phonopy and phono3py. **J. Phys. Condens. Matter**, v. 35, n. 35, p. 353001, 2023.

200 EVANS, R. F. L. et al. Atomistic spin model simulations of magnetic nanomaterials. **Journal of Physics: Condensed Matter**, IOP Publishing, v. 26, n. 10, p. 103202, feb 2014. Disponível em: <https://dx.doi.org/10.1088/0953-8984/26/10/103202>.

201 ARAúJO, A. L.; MACIEL, R. P. **VASProcar v1.1.18.10 - Python tools for DFT calculations**. Zenodo, 2023. Disponível em: <https://doi.org/10.5281/zenodo.8370829>.

Appendix

APPENDIX A

Computational details

In this appendix we will discuss the computational details that leaded to the results of this thesis.

Overall the calculations were performed using density functional theory (DFT), with the projector-augmented waves (PAW) method. We employed the plane-wave expansion, implemented in Vienna *ab initio* simulation package (VASP) [193, 194]. The exchange and correlation term was described using the generalized gradient approximation (GGA), with the Perdew-Burke-Ernzerhof (PBE) functional [62]. For a better description of magnetic properties, we considered the DFT+U correction, as detailed in the respective section. Tight-binding models were constructed within the Wannier functions formalism, with parameters extracted from DFT calculations using Wannier90 [195]. The topological invariants were calculated using the Wannier charge centers [148] implemented in Z2Pack [149]. The particularities of each study are discussed next.

A.1 Chapter 4

The calculations were performed with a kinetic energy cutoff of 420 eV. The convergence criterion for residual forces was set to 0.001 eV/Å. All calculations included fully relativistic effects in the pseudopotentials. The electronic correlation of the vanadium 3*d*-orbitals was described with the DFT+U method using the Dudarev formalism [63]. We optmized the effective U parameter by means of linear response method [69]. For the single vanadium impurity study, a 5×5×1 supercell with 50 atoms was used, the Brillouin zone was mapped by a 7×7×1 Monkhost-pack k-mesh. We adopted a vacuum of 15Åin the c-direction to avoid interactions with its periodic image. To investigate the coupling effects between the impurities for the highest inter-V distances (7 lattice parameters) the supercell in both bulk and edge contains 308 atoms.

To solve the integrals of RKKY interaction, numerical calculations methods were used. We use a code, originally written by Silva and Vernek [159], in `Julia` language adapted for this study.

A.2 Chapter 5

For this study, we adopted a plane wave kinetic energy cutoff of 400 eV. We have used fully relativistic effects in the pseudopotentials. The Brillouin zone was sampled using a Monkhost-Pack grid of 11×11×1 for the unit cell. The topological properties were calculated with the WannierTools package [196], which was used to determine the Weyl chirality, Chern number and projected edge states (without edge passivation). To avoid the dangling bonds in the edge states, we build a nanoribbon replied 11 times in a direction. We performed the relaxation of Si-H and Ge-H edge bonds in a convergence criterion of 10^{-7} eV. The lenghts of saturated nanoribbons are 12.4 nm for Ge and 12.2 nm for SiGe.

A.3 Chapter 6

We performed calculations with converged plane-wave kinetic energy cutoff of 350 eV. All the calculations included relativistic effects. The relaxation calculations were carried with a total energy convergence of 10^{-6} eV and a residual force criterion of 0.001 eV/Å. We used a Brillouin zone k-mesh of 15×15×1 in the Monkhost-Pack formalism. To prevent periodic image interactions, we adopted a 15Åof vacuum between the layers. We performed *ab initio* molecular dynamics (AIMD) simulations in the canonical ensemble (NVT) at 300 K using a 3×3×1 supercell over a 10 ps timeframe to investigate the thermodynamic stability. We studied the elastic properties by means of the strain-energy curve as a function of biaxial tensile strain, obtained with the VASPKIT facility [197]. The dynamical stability were investigated by phonon dispersion analysis, using the PHONOPY code [198, 199]. To accurately describe the electronic correlation in 3*d*-orbitals from Cr, we applied the DFT+U correction via Dudarev method [63]. We determined the Curie temperature using Monte Carlo simulations based on the Heisenberg model, with the parameters extracted from DFT results using the VAMPIRE package [200]. The topological properties, such as Chern number and Berry curvature, were investigated with WannierTools [196]. The VASP data were obtained with VASProcar [201].

APPENDIX B

Academic production

B.1 Thesis originated articles

1. **Emmanuel V. C. Lopes**, Tome M. Schmidt; *Tuning quantum anomalous Hall effect in ferromagnetic 1T-CrX2 (X = Bi, Sb) monolayers*. Applied Physics Letters; 125 (24): 243103. https://doi.org/10.1063/5.0244117.

2. **Emmanuel V. C. Lopes**, Rogério J. Baierle, Roberto H. Miwa, Tome M. Schmidt; *Noncentrosymmetric two-dimensional Weyl semimetals in porous Si/Ge structures*. Journal of Physics: Condensed Matter; 36 (18): 185701. https://dx.doi.org/10.1088/1361-648X/ad1e09.

3. **Emmanuel V. C. Lopes**, Edson Vernek, Tome M. Schmidt; *RKKY interactions mediated by topological states in transition metal doped bismuthene*. Journal of Applied Physics; 133 (11): 115105. https://doi.org/10.1063/5.0140027.

B.2 Articles in collaboration

1. Marcos O. G. Junior, Augusto L. Araujo, **Emmanuel V. C. Lopes**, Tome M. Schmidt. *Weyl semimetal engineering by symmetry control in $NiTe_2$*. arXiv:2506.13908 [cond-mat.mtrl-sci]. https://doi.org/10.48550/arXiv.2506.13908.

2. Bryan D. Assunção, **Emmanuel V. C. Lopes**, Tome M. Schmidt, Gerson J. Ferreira. *A tangible $k{\cdot}p$ approach to quasisymmetries, pseudosymmetries and other pathways to small anticrossings*. **Under preparation**.

B.3 Conferences

1. **Autumn Meeting 2022 Brazilian Physical Society**, São Paulo, SP, Brazil (10-14 April, 2022), Contributed Talk: "Magnetic Impurities in a Quantum Spin Hall

Insulator".

2. **8º Encontro do INCT Nanocarbono e 2º Encontro da REDE 2D**, Uberlândia, MG, Brazil (17-19 November, 2022), Presented Poster: "Impurezas Magnéticas em um Isolante Topológico 2D".

3. **Autumn Meeting 2023 Brazilian Physical Society**, Ouro Preto, MG, Brazil (21-25 May, 2023), Contributed Talk: "Two-dimensional Weyl semimetals in porous structures".

4. **3º Encontro da REDE 2D**, Belo Horizonte, MG, Brazil (13-14 November, 2023), Contributed Talk: "Noncentrosymmetric two-dimensional Weyl semimetals in porous Si/Ge structures".

5. **21st Brazilian Workshop on Semiconductor Physics (BWSP)**, Campinas, SP, Brazil (02-06 September, 2024), Young Researcher Contributed Talk: "Noncentrosymmetric two-dimensional Weyl semimetals in porous Si/Ge structures".

6. **9º Encontro do INCT Nanocarbono e 4º Encontro da REDE 2D**, Belo Horizonte, MG, Brazil (11-13 September, 2024), Presented Poster: "Strain-induced quantum anomalous Hall effect in 1T-CrX_2 monolayers (X = Bi, Sb)".

7. **Autumn Meeting 2025 Brazilian Physical Society**, Belém, PA, Brazil (18-22 May, 2025), Contributed Talk: "Tuning quantum anomalous Hall effect in 1T-CrX_2 (X = Bi, Sb) monolayers.".

B.4 Awards

2024 Institute of Physics (IOP) Trusted Reviewer Status, IOP Publishing.